

Experimental Investigation on the Aerodynamic Performance of a Compressor Cascade in Droplet Laden Flow

Von der Fakultät für Maschinenbau
der Helmut-Schmidt-Universität / Universität der Bundeswehr Hamburg
zur Erlangung des akademischen Grades eines Doktor-Ingenieurs
genehmigte

DISSERTATION

vorgelegt von

Birger Ober

aus Weilburg

Hamburg 2013

Tag der mündlichen Prüfung: 25. Juni 2013
Erstgutachter: Prof. Dr.-Ing. Franz Joos
Zweitgutachter: Prof. Dr.-Ing. habil. Bernhard Weigand

Experimental Investigation on the Aerodynamic Performance of a Compressor Cascade in Droplet Laden Flow

By the Department of Mechanical Engineering
der Helmut-Schmidt-Universität / Universität der Bundeswehr Hamburg
for obtaining the academic degree of a Doktor-Ingenieur approved

Doctoral Thesis

submitted by

Birger Ober

from Weilburg

Hamburg 2013

Preface

This thesis is the result of my investigative studies as Research and Teaching Assistant at the Helmut Schmidt University's Laboratory for Turbomachinery, and at Vattenfall Nuclear Energy GmbH, both in Hamburg, Germany.

As mentor for this thesis, I want to thank Prof. Dr.-Ing. Franz Joos for his advice and expertise, and also for providing access to the laboratory's infrastructure, thereby facilitating my experimental investigations. My sincere appreciation is also extended to Prof. Dr.-Ing. habil. Bernhard Weigand for his co-mentoring expertise. My gratitude goes also to Dr. Uwe Kleen for providing a flexible and supportive work environment and for sharing his valuable experiences.

I also thank my colleagues at the Laboratory for Turbomachinery for providing a motivating and inspiring work environment. To Hans Joachim Dehne a special thank you for contributing to this project with his practical advice and machining skills in every aspect connected to the test rig.

My appreciation also to Dr.-Ing. Tjark Eisfeld, Niklas Neupert and Ulrike Wagner who have reviewed the manuscript, providing guidance to make it more comprehensible.

I would like to thank my parents for their years of support. Finally, to Ulrike: Thank you for your help, your guidance, and your patience.

Berlin, August 2013

Birger Ober

Kurzfassung

Eine Methode zur kurzfristigen Leistungssteigerung von Gasturbinen ist das Eindüsen flüssigen Wassers in den Ansaugbereich des Verdichters. Hierbei handelt es sich um eine etablierte Technik, die in der Lage ist, Minderleistung, wie sie beispielsweise durch hohe Umgebungstemperaturen hervorgerufen wird, durch den kühlenden Effekt des verdunstenden Wassers auszugleichen.

Allerdings sind die Auswirkungen auf das aerodynamische Verhalten der Verdichterbeschaufelung nicht erschöpfend erforscht. Das Wissen um die Einflüsse, die durch die Anwesenheit flüssiger Wassertropfen in der Verdichterströmung hervorgerufen werden, ist unverzichtbar in dem Bestreben, das Potenzial dieser Technologie bestmöglich zu nutzen.

Ein verbessertes Verständnis der zugrundeliegenden Effekte trägt dazu bei, Gasturbinen eine Leistungscharakteristik zu verleihen, die sie in die Lage versetzen, den gesteigerten Flexibilitätsanforderungen, welche aus der steigenden Erzeugungskapazität erneuerbarer Energiequellen und den politischen Rahmenbedingungen erwachsen, gerecht zu werden.

Um die Wissensbasis in diesem Bereich zu erweitern, werden in dieser Arbeit die Ergebnisse experimenteller Untersuchungen an einer Verdichterkaskade präsentiert. Die Beschaufelung der Kaskade ist abgeleitet von der Rotorbeschaufelung eines Axialverdichters. Die Versuche behandeln das Verhalten der Beschaufelung bei variierenden Eintrittsmachzahlen, Wasserbeladungen der Strömung und Anstellwinkeln der Beschaufelung.

Der Versuchsaufbau besteht im Wesentlichen aus einem geschlossenen Windkanal, in dem die Kaskade montiert ist, und einem Phasen Doppler Anemometer, einem laserbasierten Messsystem, das in der Lage ist, die Geschwindigkeit und Größe eines in der Verdichterströmung befindlichen Wassertropfens, zu bestimmen.

Diese Arbeit umfasst die Beschreibung der Versuchsanlage, die Darstellung der den Versuchen zugrundeliegenden, physikalischen Konzepte sowie die Auswertung und Interpretation der Messergebnisse.

Die Auswertung der Ergebnisse basiert auf den Geschwindigkeitsmessungen der Strömung in Ein- und Austrittsebene der Kaskade sowie im Schaufelkanal. Die Auswertung zielt darauf ab, die Einflüsse, die durch die Präsenz der Wassertropfen in der Strömung hervorgerufen werden zu identifizieren. Hierzu wird ein Vergleich zu einer Referenzströmung gezogen, die nicht mit Wassertropfen beladen ist. Die Ergebnisse beinhalten qualitative Bewertungen zum Verhalten des Wassers auf der Beschaufelung, die Analyse und

Bewertung der Geschwindigkeitsprofile im Kaskadenaustritt sowie die Untersuchung des Folgeverhaltens verschiedener Tropfenklassen anhand der Messungen im Schaufelkanal. Weiterführende Auswertungen bestimmen den Verlustbeiwert, Abströmwinkel, DeHaller-Zahl und Stromschichtdickenverhältnis (AVDR) jeder Messreihe.

Die Ergebnisse zeigen, dass die in der Strömung vorhandenen Wassertropfen die Aerodynamik der Verdichterströmung teilweise erheblich beeinflussen. Hier sind zwei Haupteffekte zu nennen. Zum einen ein Strömungsablösungen dämpfender Effekt, der den Betriebsbereich der Beschaufelung bei sehr niedrigen Anstellwinkeln erweitert und zu verminderten Verlusten führt. Zum anderen ein verlustverstärkender Effekt, der bei mittleren und hohen Anstellwinkeln auftritt und primär auf den auf der Beschaufelung befindlichen Wasserfilm zurückzuführen ist.

Abstract

One approach for the power augmentation of gas turbines is to inject liquid water into the compressor intake. This established technology, commonly referred to as inlet fogging or overspray fogging, is able to overcome power output deficits that occur in environments with high ambient temperatures. This is achieved by the cooling effect that evaporating water exerts on the intake air.

However, the effects of the application of this technology on the aerodynamic behavior of compressor blades is not yet fully understood. The knowledge of the influences that are provoked by the presence of liquid water droplets in the compressor flow is vital for the endeavor to fully utilize the potential of this technology.

An improved understanding of the underlying basic principles contributes to adapting the performance characteristics of gas turbines to cater for increasing demands for flexibility, which arise from a growing renewable generation capacity in the grid and economic and political boundary conditions.

In order to broaden the knowledge base in this field, the results of experimental investigations, conducted on a linear compressor cascade are presented in this work. The blades that were mounted in the cascade are derived from the rotating blades of an axial compressor. The experiments focused on the aerodynamic behavior of the cascade under varying boundary conditions. The variables were: inlet Mach number, water load of the flow and incidence angle.

The test rig comprises essentially a wind tunnel which contains the compressor cascade and a Laser-Doppler-Anemometer, a laser based measurement technique that is capable of recording the velocity and size of a water droplet traveling through the wind tunnel.

This work includes the description of the test rig, the discussion of the underlying physical principles as well as the compilation and interpretation of the experimental results.

The compilation of the results is based on the velocity measurements at the cascade's inlet and discharge plane as well as the inter blade flow channel. The interpretation of the results aims at identifying the influences provoked by the presence of water droplets in the compressor flow. In order to achieve this, the water laden flow is compared to a dry reference flow. The results include a qualitative analysis of the water movement on the blade surface, the analysis of the flow in the cascades discharge plane and the ability of different droplet classes to follow the flow in the inter blade

flow channel. Further investigations show the loss coefficient, discharge flow angle, DeHaller number and the axial velocity density ratio (AVDR) of each experiment.

The results show that the droplets present in the flow influence the aerodynamics of the blades considerably on some operating points. Two main effects can be identified. Firstly, a dampening effect on flow separations, that broadens the operating regime for very low incidence angles and reduces losses. Secondly a loss increasing effect that can be primarily accounted to the water film on the blade surface in the mid range of incidence angles.

Contents

I	Nomenclature	iii
1	Introduction	1
1.1	State of the Art	2
1.2	Scope of this Work	6
2	Experimental Setup	9
2.1	Infrastructure	9
2.2	Test Rig	9
2.2.1	Angle of Incidence	11
2.2.2	Boundary Layer Injection	12
2.2.3	Water Injection	14
2.2.4	Cascade Properties	16
3	Basic Principles	23
3.1	Principles of Two-Phase-Flow	23
3.1.1	Continuous Phase	23
3.1.2	Gas Dynamics	26
3.1.3	Dispersed Phase	28
3.2	Droplet Behavior	29
3.2.1	Droplet Movement	29
3.2.2	Droplet Deformation and Droplet Breakup	32
3.2.3	Droplet Wall Interaction	36
3.2.4	Droplet Entrainment	41
3.2.5	Water Film Formation	41
3.3	Measurement Techniques	43
3.3.1	Laser Doppler/Phase Doppler Anemometry	43
3.3.2	LDA/PDA Data Acquisition	49
3.3.3	Optical Measurement of Water Load	51
3.3.4	Shadowgraphy	53
4	Experiments Conducted	55
4.1	Phenomenological Experiments	55
4.1.1	Investigation of the Water Film Formation	56
4.1.2	Droplet Disintegration	59
4.2	Investigation of Cascade Discharge Properties	63
4.2.1	Discharge Flow Velocity	63
4.2.2	Deflection Angle	79

4.3	Investigation of Performance Parameters	92
4.4	Investigation of the Inter Blade Flow	102
5	Conclusion	109
5.1	Summary	109
5.2	Future Prospects	111
	Bibliography	113
	List of Figures	121
	List of Tables	124

I Nomenclature

Latin Symbols

a	m/s	Speed of Sound
A	m ²	Area
c	m/s	Absolute Velocity
c	m	Chord Length
c	kJ/kg K	Specific Heat Capacity
C	1/m ³	Concentration
C	-	Drag Coefficient
d	μm	Diameter
D	-	Diffusion Function
f	N/m ³	Volume Specific Force
f	Hz	Frequency
f	-	Drag Factor
F	N	Force
h	m	Blade Height
h	kJ/kg	Specific Enthalpy
h	m	Film Thickness
H	kJ/kg	Specific Total Enthalpy
H	-	Film Thickness
I	W/m ²	Intensity
m	kg	Mass
\dot{m}	kg/s	Mass Flow Rate
p	Pa	Pressure
q	W/m ²	Heat Flux Density
Q	-	Coefficient
r	m	Radius
s	m	Distance
s	m	Pitch
t	s	Time
t'	s	Time
T	K	Temperature

u	m/s	Circumferential Velocity
u	m/s	x - Velocity
v	m/s	y - Velocity
V	m^3	Volume
\dot{V}	m^3/s	Volume Flow Rate
w	m/s	Relative Velocity
w	m/s	z - Velocity
x	m	Coordinate
X	kg/kg	Water Load
y	m	Coordinate
z	m	Coordinate

Greek Symbols

α	$^\circ$	Impact Angle
β	$^\circ$	Flow Angle
δ	m	Boundary Layer Thickness
δ_1	m	Displacement Thickness
δ_2	m	Impulse Loss Thickness
δ_3	m	Energy Loss Thickness
Δ	-	Difference
γ	-	Surface Roughness
η	-	Efficiency
η	Pa s	Dynamic Viscosity
Θ	$^\circ$	Laser Beam Intersection Angle
Θ	$^\circ$	Flow Angle
κ	-	Isentropic Exponent
λ	W/mK	Thermal Conductivity
λ	m	Wave Length

Π	-	Pressure ratio
ρ	kg/m ³	Density
σ	-	Solidity
σ	°	Shock Angle
σ	N/m	Surface Tension
τ	N/m ²	Shear Stress
τ	s	Time
ϕ	-	Stage Flow Coefficient
ϕ	°	Scatter Angle
χ	-	Mole Fraction
ψ	-	Stage Work Coefficient
ω	1/s	Angular Velocity

Indices

a	Air
c	Circumferential
c	Continuous
cas	Cascade
crit	Critical
desal	Desalinated
dis	Disintegration
d	Droplet
D	Drag
ext	Extinction
h	Homogeneous
imp	Impact
is	Injection System
k	Kinematic
m	Meridional
max	Maximal
p	Constant Pressure
rel	Relative

s	Isentropic
s	Shear
sc	Settling Chamber
tot	Total
w	Water
v	Velocity
0	Initial
1,2	Positions
∞	Infinity

Abbreviations

CFD	Computational Fluid Dynamics
LDA	Laser Doppler Anemometer
MLFT	Minimum Liquid Film Thickness
MMD	Mass Median Diameter
MWR	Minimum Wetting Rate
PDA	Phase Doppler Anemometer
SMD	Sauter Mean Diameter

Dimensionless Numbers

AVDR	Axial Velocity Density Ratio
H	Film Thickness
Ha	DeHaller Number
K	Splashing Factor
Ma	Mach Number
Oh	Ohnsorge Number
Tu	Turbulence
Re	Reynolds Number
St	Stokes Number
We	Weber Number
ω	Loss Coefficient

1 Introduction

The electric energy supply system is subject to constant change. Key influences are market conditions and regulatory boundary conditions. Both have substantial influence on the profitability of certain power production facilities. Recent developments in the global power production environment have increased the attractiveness of power plant types that incorporate gas turbines as main component.

Lower costs for natural gas in the United States of America due to novel exploration techniques (fracking) increase the profitability of the operation of gas fired power plants.

The transformation of the European power supply system towards a system that is based on renewable sources like wind and solar energy, introduces challenges to the electricity grid. Renewable sources show a higher volatility in energy availability than fossil fired power plants. The exact prediction of the energy availability from renewable sources still remains an unsolved challenge. This increases the demand for an infrastructure that is able to quickly adapt to the current power demand. Gas turbines, especially the aeroderivate types, have this ability which make them a valuable asset in the regulatory power market.

This background emphasises the impact of the optimisation of gas turbines in terms of efficiency, power output and flexibility. One approach to reach these targets, besides the conventional aerodynamic optimistaion, is inlet fogging. Inlet fogging allows to cool the intake air by evaporative cooling thus increasing the air mass flow rate and consequently the power output of the gas turbine. Overspray fogging increases the amount of water injected into the intake air beyond the border of saturation and allows a continuous evaporation process that influences the compression process, which is then also referred to as wet compression process. This reduces the compression work needed and increases the gas turbine cycle efficiency. The effects of water injection into the air intake of gas turbines have been mentioned as early as the 1940's, when Kleinschmidt [1] investigated the effects of water injection on the gas turbine process.

Even though investigations have been undertaken to utilise the wet compression process in flight applications, it is clear today that most of the potential from the wet compression approach will be realised in stationary gas turbines for power production. Practical considerations of wet compression lift the compressor into the focus of investigation as it is the component to be most affected by water injection.

The detailed influence of water injection on the gas turbine aerodynamics has not yet been fully understood. A systematic test approach on the aerodynamic performance of different profile families has been introduced in the laboratories of the NACA, the predecessor organisation of today's NASA in the 1950's. The use of linear compressor cascades for the investigation of the aerodynamic performance of any type of profile is established ever since.

1.1 State of the Art

Since the 1940's, when the first investigations in this field were undertaken, the interest of numerous researchers was drawn to this subject and the ongoing research has broadened since then. Today's investigations are undertaken for three main reasons.

The reduction of emissions of jet engines is a key element to limit the negative effects of increasing air and naval traffic especially in the vicinity of airports or harbors. In this context the possibilities of reducing the emission of NO_x have been intensively studied under varying boundary conditions. These studies focus on the application of water injection in aircraft engines or naval applications (e.g. [2], [3]).

A deepened knowledge of the effects of liquid water droplets in a gas turbine is also desirable for safety reasons. Investigations were conducted to assess the aerodynamic effects of ingested rain in aircraft engines (e.g. [4]) as heavy rain ingestion poses a threat to stable operation in descending flight as reported in [5].

Another focus in this context is put on the possibilities to augment the power output of gas turbines. Dietz and Flemming [6] have experimentally investigated the effects of water injection on a turbojet engine and reported a thrust surplus of up to 15% but at significantly increased fuel consumption. Most publications today concentrate on stationary gas turbines in simple and combined cycle power plants as the need for power augmentation, especially in warm regions of the earth, is a prominent challenge.

A comprehensive overview of the underlying climatic and psychrometric properties is given in [7]. In this, Bhargava et al. discuss the attractiveness of evaporative fogging due to its effectiveness and low initial costs and give information on nozzle characteristics and practical considerations. Theoretical and experimental aspects of wet compression are discussed in [8]. The authors lift up the considerations to be made prior to installing a water injection system, like compressor inlet temperature profile distortion, tran-

sients and the reduction of the compressor's surge margin. More practical considerations for the operation of such systems are given in [9] and [10]. It has been found that the use of demineralized water is advisable and that the size of the droplets has an influence on erosion phenomena.

Bhargava and Meher-Homji conducted an analysis of the power augmentation potential for different gas turbine types in [11]. The key findings of their work are that a correlation exists between the key design parameters of the gas turbine and the effect of water injection. They also state that aeroderivative machines benefit more from water injection than heavy duty gas turbines.

A comparison of the different power augmentation technologies has been conducted by Bianchi et al. [12]. They report that all technologies yield a percentage wise higher power boost than the corresponding change in heat rate in gas turbine applications. An analysis of the power augmentation potential that incorporates climatic boundary conditions is given by Chaker et al. [13].

The above mentioned investigations take a result driven standpoint and are motivated from a wholistic view. A common basis for all the effects mentioned above is the detailed thermodynamic and aerodynamic investigation. The gas turbine process has been investigated by numerous research groups. The thermodynamic performance of the wet compression cycle has been investigated by Zheng et al. [14]. They present a model to calculate the wet compression process. Their conclusion is, that compression work can be saved utilising water injection. Their findings can be summarized as follows:

- The presence of water droplets in the intake duct reduces the compressor inlet temperature.
- In a configuration, where droplet evaporation takes place inside the compressor, necessary compression work is reduced and the compressor discharge temperature is reduced at constant pressure ratio.
- Water injection leads to an increase of effective output of the thermodynamic gas turbine process and a slight increase in efficiency.
- The effect of water injection depends on the properties of the injected water. Small droplet diameters are desirable as these result in a high evaporation rate.

Zheng et al. also compared different gas turbine cycles including regenerative and inter cooled cycles [15]. The highest power output and efficiency

could be seen for the regenerative cycle with water injection.

Roumeliotis [16] investigated the effects of water injection using an adaptive performance modeling technique that allows to investigate different component characteristics. The results from this research with respect to water injection can be summarized as follows:

- The engine's power output benefits from water injection even in low ambient temperatures and ISO conditions.
- Lower droplet diameter and higher ambient temperature increase the possible gain in power output.
- Water injection leads to a significant loss in surge margin and poses the risk of erosion of the blades.

Water injection imposes changes on the compression process. The latent heat of water causes an internal cooling during the compression due to the evaporation. Different research groups have developed models to calculate the wet compression process. They focus on the effects for the compressor operation. Among these are Horlock [17], White and Meacock [18], Khan and Wang [19] and Matz [20]. The key findings are:

- The evaporation of water droplets in the compressor lead to the off design operation of single stages. The front stages are less loaded, moving the operation point closer to choke conditions. The operation point of the rear stages is moved toward overload and therefore a stall condition.
- The irreversible entropy production is dependent on the droplet size distribution.
- Droplet size also determines the evaporation rate and therefore the compressor outlet temperature and necessary compression work.
- Compressor mass flow rate increases as the operating point of the first stages is moved towards a lower pressure ratio and a higher volume flow rate.
- The necessary compression work is reduced due to the continuous evaporation of the droplets.

A recent investigation has been carried out by White and Meacock. They applied a calculation model that takes a number of effects into account,

such as the polydispersion of droplet sizes, droplet temperature relaxation effects, slip velocity effects and the impingement of droplets onto the blades and film evaporation to a generic 12-stage compressor. Their results show that accounting for slip velocity effects leads to higher evaporation rates due to higher heat and mass transfer rates. They restate the degradation of aerodynamic performance of single compressor stages due to their off design operation [21].

Potential benefits in terms of the compression process' efficiency have been identified by Eisfeld in [22].

Other recent thermodynamic investigations state that droplet evaporation strongly depends on the diameter of the injected droplets and that it is a main driver for cooling efficiency within the flow [15],[17],[8]. The result is reduced compressor work and a higher efficiency.

Even though a substantial number of wet compression upgrades and retrofits have been installed, the aerodynamic effects a droplet laden flow imposes on the axial compressor are not fully understood. An investigation on the aerodynamic behaviour of a compressor airfoil has been conducted by Eisfeld and Joos [23]. The findings presented state that the effects of water injection into a linear compressor cascade in terms of the loss coefficient are beneficial in case of high blade loading and detrimental in case of low blade loading.

Investigations that focus more on the operation map have been conducted by Brun et al. [24]. They found in a thermodynamic analysis that wet compression can result in a displacement of the operating point towards the surge line.

The further development of computational fluid dynamics(CFD) applications and the increasing computing resources in recent years allows the numerical investigation of increasingly complex models.

Sun et al. [25] investigated the 3D flow field of a compressor stage under wet compression conditions using a commercial CFD code. They found a stabilising effect for flow separations on the rotor blades suction surface.

Luo et al. [26] made an attempt to simulate the effects of water injection in the near stall and choke condition. Their results show a dampening effect with regard to flow separations that was most prevalent on the rotor blade's pressure side near choke condition.

In [27] Sun et al. used a 3D model of an entire gas turbine to calculate the effects of water injection. They report that water injection leads to an increased mass flow and power output as well as a higher compressor efficiency. They could also identify an improvement for the flow separation

behaviour on the first stage of the compressor.

1.2 Scope of this Work

The efforts of researchers in the field of wet compression in an axial compressor have covered the thermodynamic effects thoroughly and the wet compression process is well understood. The consequences for the operation of gas turbines equipped with a water injection system have been investigated and the possibility to augment the power output has been confirmed. However, the detailed aerodynamic effects on the compressor's blades imposed by the presence of liquid droplets in the compressor flow have not been fully understood.

This knowledge is desirable to be able to match the blade geometry to fully utilise the potential of wet compression. This knowledge is also beneficial in an attempt to mitigate the negative effects of wet compression like the overload of the late stages and the reduced surge margin as reported in [17]. Eisfeld [28, 22] has laid a solid, experimental foundation to increase the knowledge in this field at the open loop wind tunnel that is located at the Helmut Schmidt University of Hamburg. The wind tunnel is designed to test compressor blade geometries in wet compression conditions. However his research was restricted by the capabilities of the test rig that did not allow the investigation of a wide range of operating points.

In order to further broaden the knowledge in this area, the test rig was improved to allow the investigation of a wider range of operating points. With the improvements, the test rig is capable to simulate the entire range of stable incidence flow angles and inlet Mach numbers of $Ma_{\max, \text{in}} = 1.2$. The scope of this work is to investigate the aerodynamic performance of axial compressor blade geometries in wet compression conditions. In order to achieve this, the geometry of an mid and outer cross section of an axial compressor rotor blade was used to create a compressor cascade that simulates a two dimensional flow. The resulting geometry was tested in a variety of operating conditions. The variables were:

- Inlet Mach number: $Ma = 0.71..0.89$
- Water load: $X = 0\%...2.1\%$
- Incidence angles reflecting the entire range of incidence flow angles, that result in a stable compressor flow

The results deliver detailed information that can be used in the design of blade geometries, that aim at the full utilisation of the potential of water injection and inlet fogging. The results can also be used as a validation case for numerical simulations.

2 Experimental Setup

First systematic wind tunnel tests on compressor cascades were conducted in the 50's by the NACA [29]. Ever since, wind tunnel tests have been an important source of information on the aerodynamic performance of compressor blades as the optical accessibility provides the possibility to utilise superior laser driven measurement equipment.

2.1 Infrastructure

All experiments were conducted at the Helmut Schmidt University in Hamburg, Germany. The Laboratory of Turbomachinery on campus possesses an open loop wind tunnel.

The wind tunnel is operated through the continuous supply of compressed air which is generated by two radial compressors with adjustable guide vanes. The test rig can be operated with one active compressor, parallel coupling of both compressors for high mass flow rates or serial coupling for high pressure ratios. The maximal possible parameters are the flow rate of $\dot{V}_{\max} = 85000 \frac{\text{m}^3}{\text{h}}$ for parallel coupling and a pressure ratio $\Pi_{\max} = 3.7$ for serial coupling.

The compressed air is cooled down to an adjustable value just downstream of the compressors and then fed into the settling chamber just upstream of the wind tunnel. A bypass exists which leads directly to the off gas section. The discharge ratio is adjusted by a butterfly valve. Another butterfly valve is located in the off gas section. This configuration allows the operation of the wind tunnel at the desired mass flow rate and pressure values independently of the compressor's performance map. Another advantage of this setup is the possibility of continuous operation at stationary conditions.

The off-gas section consists of a diffuser, a water-separator-vessel and a chimney. The flow is decelerated downstream of the test section by a diffuser and led into the water separator which is equipped with sieve plates to filter out the water droplets. The flow is discharged through the chimney into the atmosphere further downstream.

2.2 Test Rig

An overview of the test rig is given in Figure 2.1. It comprises three major components. The settling chamber is a cylindrical pressure vessel with a diameter of 1.6m and built in sieve plates for flow equalisation. Thermo-

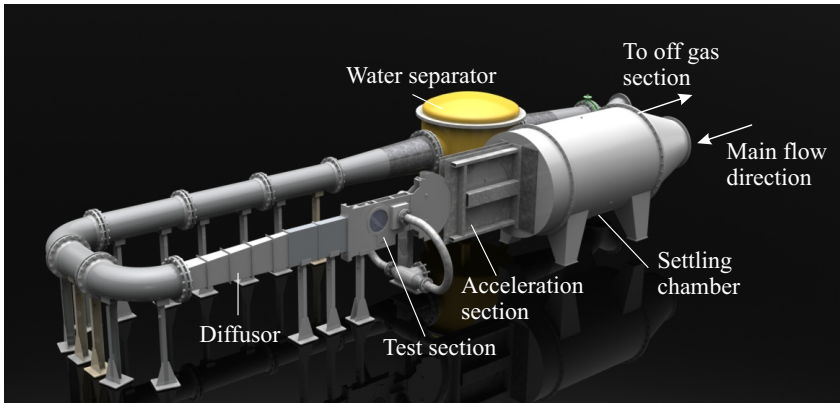


Figure 2.1: Test rig overview

couples and pressure probes are installed in the settling chamber to monitor the total temperature and total pressure.

The acceleration section has a rectangular cross section of 100mm x 300mm and is located at the outflow opening of the settling chamber. The mass flow rate depends on the pressure inside the settling chamber and the properties inside the test section.

The test section is equipped with a minimum of eight compressor blades in a linear cascade configuration mounted between two circular windows made of acrylic glass to account for optical accessibility.

An expansion step in the geometry prevents an influence of the wind tunnel walls on the discharge flow angle. The position of the lowest blade is chosen in a way that minimises the influence of the untreated boundary layer at the bottom wall of the wind tunnel to a negligible level. This configuration has been used by Ulrichs [30] and was again validated by Eisfeld [31]. Pressure probes are mounted at the inlet and discharge plane of the cascade to monitor the periodicity of the flow as depicted in Figure 2.2. Thermocouples are mounted at the outlet, additionally. The ideal investigation of a flow through a rotating machine in a linear cascade requires the development of the investigated cross section into an infinite plane. As this is impossible, the deviation from the ideal scenario has to be accounted for in the evaluation of the test data. Recommendations are given in [32].

The restricted number of blades used in the linear cascade can lead to an

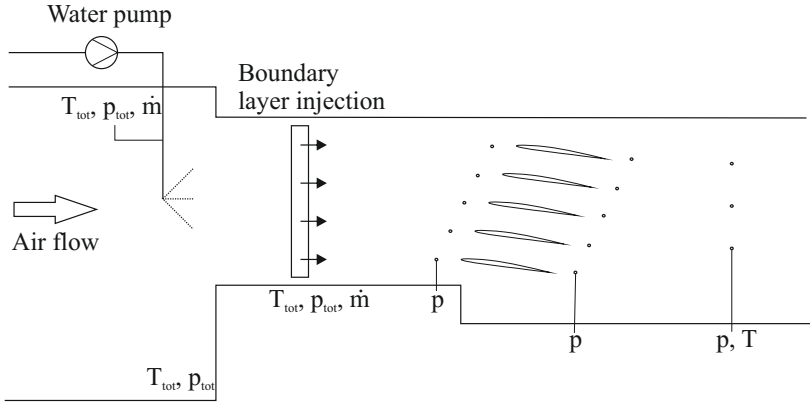


Figure 2.2: Measurements taken in vicinity of test section

inhomogeneous incident flow, because the upper and lower blades may receive a misaligned incident flow. As the flow in the rotating machine can be assumed to be identical for every blade passage, the aim is to have identical flow conditions for every blade in the cascade. Due to this, the periodicity of the incident flow has to be controlled. In this case this is achieved by the measurement of the static pressure along the cascade.

The flow is likely to develop corner vortices on the suction side of the blades at the side walls of the wind tunnel. This leads to a contraction of the free flow area. This effect has to be evaluated and accounted for.

Moreover it is recommended by Hirsch in [32] that a minimum chord length of 60 mm is used, as a greater scale increases the accuracy of measurement. In the course of the experiments presented in this work, a chord length of 50 mm is used, because the utilised measurement equipment allows for good accuracy albeit. Additionally, a minimum of five blades is suggested in order to improve the periodicity of the flow.

2.2.1 Angle of Incidence

The test rig is equipped with a mechanism that allows the variation of the angle of incidence. The possible range of incidence angles is 20 degrees while the design angle of incidence of the respective blade is chosen to be the center position of the variation mechanism. The absolute position is displayed by

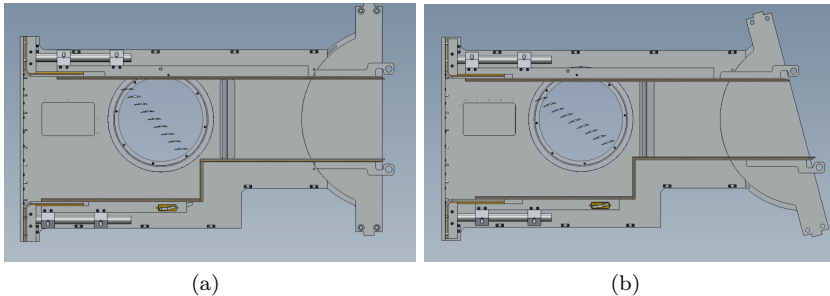


Figure 2.3: Incidence angle variation mechanism in neutral position (a) and neutral position plus 5° (b)

a scale on the rotating part of the outer wall of the wind tunnel. The accuracy of the adjusted angle is cross checked by the alignment of the laser light source of the Phase Doppler Anemometer and a reference point on the blade. The kinematics of the mechanism can be seen in Figure 2.3a and 2.3b.

A rotational movement of the right part of the outer wall is achieved by a manual drive (not depicted). The rotation is translated by a bolt joint into an axial movement of the upper and lower walls. The insularity of the wind tunnel is maintained by the compensators. They consist of linear ball bearings and a linear guide. The main upper and lower walls have cut-outs that allow a part of the compensator to slide in. In that way the assembly is able to adjust the length automatically depending on the axial position of the main walls. Two additional bolt joints translate the axial movement of the upper and lower wall into a rotation of the acrylic glass windows. The center of rotation is the leading edge of the analyzed blade.

2.2.2 Boundary Layer Injection

In accordance with the recommendations in [32] the test facility is equipped with a wall boundary layer treatment system to minimise the effect of free flow contraction as reported in [28]. Various systems have been tested in the past. The most common system uses a boundary layer suction system that reduces the boundary layer thickness by an opening in the side walls upstream of the cascade where an underpressure is applied. The underpressure directs the flow close to the side walls into the openings. The result

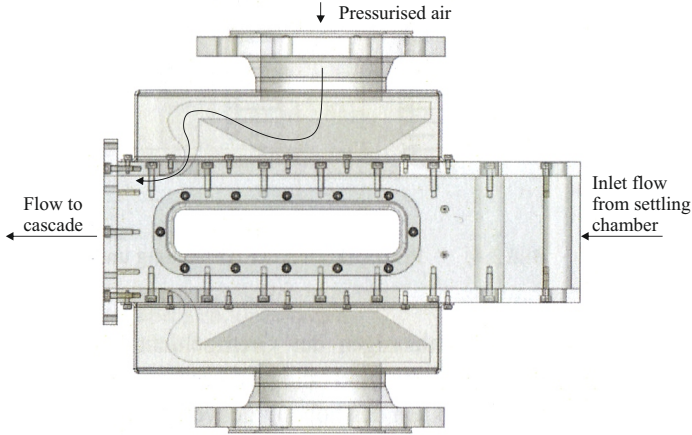


Figure 2.4: Boundary layer injection system: nozzle configuration

is a reduced boundary layer thickness and therefore a reduced influence on the 2D flow.

Another configuration that aims at the same goal works with a similar configuration but with an overpressure that is applied at the side wall openings. The side walls of the wind tunnel used in this investigation have a slit nozzle each that are formed to inject air into the wall boundary layer and refill the velocity profile. The nozzles are supplied with pressurised air via a plenum chamber as depicted in the nozzle configuration in Figure 2.4.

The nozzles inject the air tangentially thereby utilising the coanda effect that fosters the attachment of the flow to the nozzle wall resulting in a well aligned flow in the direction of the primary flow. The configuration consists of an additional line of pressurized air that bypasses the settling chamber, a butterfly valve and the nozzles. The configuration can be seen in Fig. 2.6b. Depending on the compressor blade's profile and the angle of incidence, the flow rate through the cascade \dot{V}_{casc} , which is dependent on the pressure in the settling chamber p_{sc} , has to be adjusted. In order to achieve an even span wise velocity profile for all operation points (flow rates), the individual adjustment of the pressure in the injection system p_{is} and in the settling chamber is necessary. This is realised by the bypass configuration. The maximum possible pressure in the injection system and the settling chamber is the compressor's discharge pressure (neglecting the pressure loss in

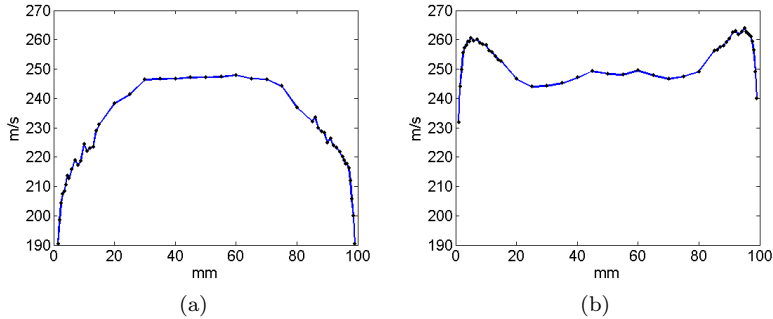


Figure 2.5: Measured inlet velocity profile without (a) and with (b) injection as reported in [28]

the piping).

During operation, p_{is} is usually the compressor discharge pressure and p_{sc} in the range of 20% to 40% of that value which results in a mass flow rate of about 15% of the total mass flow rate. The effectiveness of this system can be assessed via the velocity profiles at the cascades inlet plenum as shown in Figure 2.5a and Figure 2.5b. The spanwise velocity profiles illustrate the boundary layer by a low velocity regime close to the side walls in case of a non operating boundary layer injection system (Figure 2.5a) and with operating boundary layer injection system (2.5b). The velocity profile clearly shows a significantly reduced area of low kinetic energy fluid which tends to produce flow separations. The boundary layer is reenergised. [33]

2.2.3 Water Injection

The water that is used during the experiments is supplied by the laboratory's decalcification equipment which also supplies water to the laboratory's steam generator. The decalcified water is fed into a reverse osmosis rig that desalinates the water.

The reverse osmosis rig is capable of delivering $\dot{V}_{w, \text{desal}, \text{max}} = 1\text{m}^3/\text{h}$ at a conductivity of 3...4 μS . The desalinated water is then passed through a set of filters that reduces the water conductivity to $< 2 \mu\text{S}$. The outlet of the filter is connected to the storage tank that has a storage volume of 2m^3 . A conventional low pressure pump feeds the demineralised water to

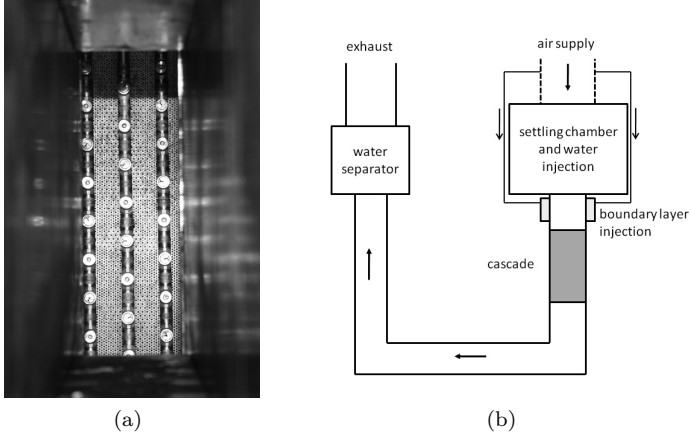


Figure 2.6: View into the settling chamber (a). Schematic of test rig configuration (b).

the high pressure pump that increases the water pressure to operating conditions of the nozzle manifold of $p_w = 200$ bar. The manifold is a set of pipes equipped with nozzles that form a uniformly distributed grid. In the course of the experiments, the manifold was equipped with either 10 or 15 nozzles.

The nozzles were PJ10 pin jet type nozzles manufactured by BETE. The spray characteristics produced by a PJ10 nozzle according to the manufacturer are given in Table 2.1. The nozzle manifold is positioned centrally in the settling chamber facing the entrance of the cascade. A view into the settling chamber from a downstream position (close to the test section) showing the nozzle manifold can be found in Fig. 2.6a.

The result is a uniform water loading at the cascade entrance with a low initial velocity of $< 2 \frac{\text{m}}{\text{s}}$. Since the water injection is located $s > 2$ m upstream of the test section, a homogeneous water distribution is assumed for the blades in the middle of the cascade. A typical droplet size distribution at the cascade's inlet plane can be found in Fig. 2.8.



Figure 2.7: Pin jet nozzle bete PJ10

Table 2.1: Spray properties produced by PJ10 nozzle at 200bar

Property	Value
d_{10}	$5.8 \mu\text{m}$
d_{32}	$20 \mu\text{m}$
$d_{v,0,1}$	$12 \mu\text{m}$
$d_{v,0,5}$	$27 \mu\text{m}$
$d_{v,0,9}$	$43 \mu\text{m}$

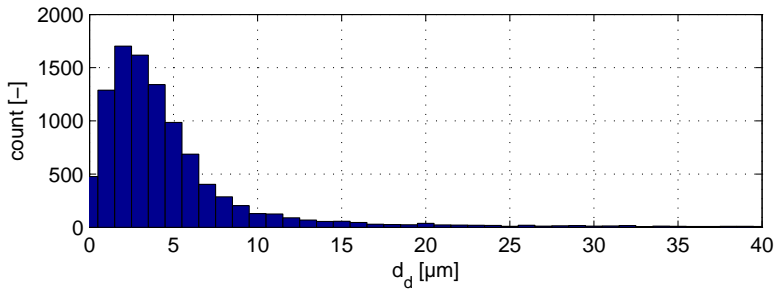


Figure 2.8: Measured droplet size distribution at cascade inlet; total number of droplets per node: 10000

2.2.4 Cascade Properties

Several authors have presented the theory of axial compressors in great depth. Among these are Traupel in [34] and [35], Oertel in [36] and Aungier in [37]. For this reason only a short overview over the basic principles of an axial compressor will be given.

A single stage of an axial compressor is described by velocity plans as depicted in Figure 2.9. In this, c describes the fluid velocity in a fixed coordinate frame, w is the fluid velocity in the coordinate frame that moves according to the blade and ωr is the circumferential velocity as seen from a polar surface view, while r is the distance from the center of rotation to the respective surface. Plane 1 denotes the rotor entry plane and plane 2 is located between rotor and stator. The rotor rotates at a constant speed

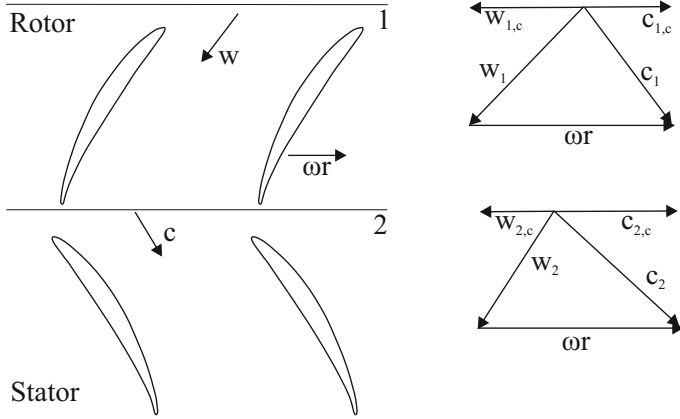


Figure 2.9: Axial compressor velocity plan

ωr . The total enthalpy rise for the flow through a rotor blade is given by Euler's turbine equation with $u = \omega r$.

$$\Delta H = u(c_{2,c} - c_{1,c}) = L_u \quad (2.1)$$

L_u is the stage work. The static enthalpy h is related to the total enthalpy H by:

$$H = h + \frac{1}{2}c^2 \quad (2.2)$$

The enthalpy change for the stator and the rotor are defined as:

$$\text{rotor} \quad \Delta h'' = h_2 - h_1 = \frac{1}{2}(w_1^2 - w_2^2), \quad (2.3)$$

$$\text{stator} \quad \Delta h' = h_3 - h_2 = \frac{1}{2}(c_1^2 - c_2^2). \quad (2.4)$$

The enthalpy difference over the entire stage is the sum of both terms $\Delta h = \Delta h' + \Delta h''$. With the respective isentropic change of state over the entire stage Δh_s , the stage efficiency (neglecting the exit losses) becomes:

$$\eta_u = \frac{\Delta h_s + \frac{c_2^2 - c_1^2}{2}}{L_u} \quad (2.5)$$

In order to compare different compressor designs, the definitions of dimensionless numbers is helpful. The most common are the stage work coefficient, stage flow coefficient and the stage reaction.

$$\psi = \frac{\Delta h_s}{u^2}, \quad \phi = \frac{c_m}{u}, \quad r_k = \frac{\Delta h_s''}{\Delta h_s' + \Delta h_s''} \quad (2.6)$$

In the case of a two dimensional flow, as in the investigations in this work, the flow can be described by a set of properties that are independent of the span wise flow direction. The governing properties are:

- Inlet velocity $w_1(y) = \text{const.}$
- Inlet flow angle β_1
- Discharge velocity $w_2(y)$
- Discharge flow angle β_2
- Wake momentum thickness δ_2 .

The coordinate system is chosen to be aligned with the incident flow as depicted in Figure 2.10 along with the above mentioned flow properties. The values for $w_1(y)$ and $w_2(y)$ are recorded by a 2D Laser Doppler Anemometer. This laser-based, non-intrusive measurement technique will be discussed in chapter 2.2. The wake momentum thickness δ_2 is determined in analogy to the boundary layer with the threshold $w_2(y) < 0.99\bar{w}_2$ as discussed in chapter 3.1.1.

In the course of the experiments, two blade profiles are investigated. The blade design of the blades is based on the work of Grein and Schmidt [38], who have utilised the inverse design tool ISGAV-R to design the blade profiles. This design has been utilised in the first row of rotating blades of an experimental axial compressor with the design parameters as summarised in Table 2.2. The maximum design Ma number in the high speed regime on the suction side of the first row of rotating blades $Ma_{\max} = 1.07$, the accompanying magnitude of Reynolds number $Re = 10 \cdot 10^5$ as well as the high rotational speed show the relevance of this design for industrial application.

The cascade is equipped with eight blades in the case of the middle cross section and nine blades in the case of the outer cross section.

This work aims at the evaluation of a series of aerodynamic and performance parameters of the linear cascade in connection with water injection.

Table 2.2: Compressor design parameters

Property	Value
Pressure ratio	2.03
Pressure ratio 1st stage	1.3
Mass flow rate	13.4 $\frac{\text{kg}}{\text{s}}$
Rotational speed	17000 $\frac{1}{\text{min}}$
Circumferential speed	345 $\frac{\text{m}}{\text{s}}$
Outer diameter	387 mm

Table 2.3: Geometrical data of the tested blade profiles

Property	Middle cross section	Outer cross section
number of blades	9	8
design deflection	13.9°	6°
design inlet Ma number	0.77	0.89
design DeHaller number	0.76	0.74
chord length c	50mm	50mm
blade aspect ratio h/s	2	2
solidity c/s	0.76	0.76

These dimensionless parameters are necessary for the comparison between different test cases or as a reference for numerical investigations. In the case of a geometry that resembles the aerodynamics of an axial compressor, the relevant dimensionless numbers are:

- DeHaller number $Ha = w_2/w_1$,
- Loss coefficient ω ,
- Deflection angle $\Delta\beta = \beta_1 - \beta_2$,
- Axial Velocity Density Ratio $AVDR$.

For the evaluation of the performance parameters the flow has to be analysed along the entire blade pitch. In good approximation the inlet flow properties

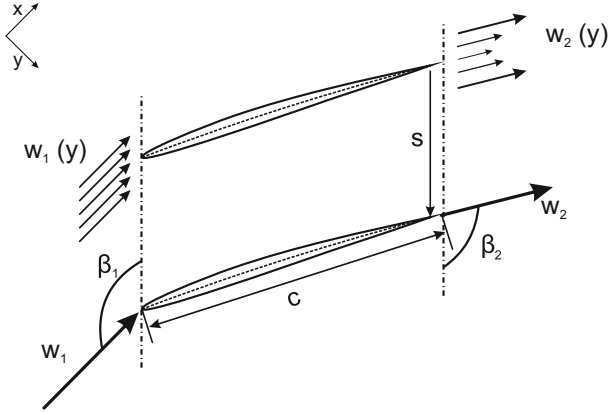


Figure 2.10: Traverse nomenclature

are independent from the relative position to the blade. The values are therefore simply averaged over the distance from blade to blade.

$$\bar{w}_1 = \frac{1}{s} \int_y^{y+s} w_1(y) dy \quad (2.7)$$

$$\bar{\beta}_1 = \frac{1}{s} \int_y^{y+s} \beta_1(y) dy \quad (2.8)$$

In this, s is the cascade pitch.

In contrast to the inlet flow is the discharge flow influenced by the wake of the blade which causes an inhomogeneity in the flow that has to be accounted for. Scholz [39] introduced an averaging method for this. The mean discharge velocity is determined by:

$$\begin{aligned} \bar{w}_2^2 &= \sqrt{\bar{w}_{2,m}^2 + \bar{w}_{2,c}^2} \quad (2.9) \\ &= \left(\frac{1}{s} \int_y^{y+s} w_2(y) \sin(\beta_2(y)) dy \right)^2 \\ &+ \left(\frac{\int_y^{y+s} w_2^2(y) \sin(\beta_2(y)) \cos(\beta_2(y)) dy}{\int_y^{y+s} w_2(y) \sin(\beta_2(y)) dy} \right)^2. \end{aligned}$$

The mean discharge flow angle is obtained by:

$$\cot \bar{\beta}_2 = \frac{\frac{1}{s} \int_y^{y+s} w_2^2(y) \sin(\beta_2(y)) \cos(\beta_2(y)) dy}{\left(\frac{1}{s} \int_y^{y+s} w_2(y) \sin(\beta_2(y)) dy \right)^2}. \quad (2.10)$$

With this, the DeHaller number and the deflection angle can be obtained directly.

The loss coefficient ω is traditionally defined as the total pressure loss coefficient and was introduced by Lieblein [40] and can be found in more recent literature as well (e.g. in [41]). In the experiments conducted here, the total pressure could not be reliably measured due to the water droplet laden flow. The liquid droplets in the flow prevent a reliable measurement with suitable probes as they would block the probe openings.

A correlation of the loss coefficient and the wake momentum thickness was presented by Aungier [37]. The correlation is given by:

$$\omega = \frac{2\delta_2\sigma}{\cos \bar{\beta}_2 c} \left(\frac{\bar{w}_2}{\bar{w}_1} \right)^2. \quad (2.11)$$

The comparability with total pressure based loss coefficients is not given as discussed by Ulrichs [30]. A relative evaluation, that uses a reference measurement, in the setup used here, is nevertheless possible.

The axial velocity density ratio $AVDR$ describes the stream tube contraction from the cascade's inlet to the discharge plane. It is given by:

$$AVDR = \frac{A_1}{A_2} = \frac{\rho_2 \sin \bar{\beta}_2}{\rho_1 \sin \bar{\beta}_1}. \quad (2.12)$$

The contraction may have different sources. The design of the flow channel between the blades and the side walls determines the constructional boundary conditions for this value. The higher the contraction of the flow channel towards the blade row discharge plane, the higher the $AVDR$. This aspect of the $AVDR$, which is not influenced by changing flow properties is combined with aspects that are influenced by the flow properties in the evaluation of the $AVDR$.

An important aspect of the $AVDR$ that is influenced by the flow properties is the growing wall boundary layer from inlet to discharge plane. An increased boundary layer thickness at the discharge plane reduces the area of free flow, thus increasing the $AVDR$.

Another aspect of influence stems from the development of vortices due to misaligned incidence flows or flow separations. These phenomena tend to block parts of the flow channel, similar to the effect caused by the boundary layer, resulting in an increased value for the *AVDR*.

Schreiber [42] reports that an increase of the *AVDR* results in an increase of the deflection angle for transonic and supersonic flows. The *AVDR* also has an influence on the blade loading and the loss coefficient as reported by Köller [43]. According to him, a decreasing *AVDR* leads to a higher loss coefficient due to the higher blade loading for high incidence angles which decreases the range of incidence angles that result in a stable compressor flow.

The influence of the *AVDR* has to be accounted for in the evaluation of the flow parameters. A more elaborate discussion of the governing mechanisms can be found in [44].

The evaluation of the *AVDR* demands the knowledge of the fluid density as well as the inlet and discharge flow angles. The flow angles can be obtained by the use of Equations 2.8 and 2.10. The determination of the flow density is a challenge in a two phase flow due to the uncertainty of temperature measurements in this type of flow.

Eisfeld [22] proposed a substitution for the fluid density utilising the knowledge of the total temperature, velocity and loss coefficient. The ratio of the temperatures is obtained by:

$$\frac{T_2}{T_1} = \left(\frac{T_{\text{tot}} - \frac{\bar{w}_2^2}{2c_p}}{T_{\text{tot}} - \frac{\bar{w}_1^2}{2c_p}} \right) \quad (2.13)$$

The ratio of the total pressure at the inlet and discharge plane is given by:

$$\frac{p_{\text{tot}, 2}}{p_{\text{tot}, 1}} = \left[1 - \left(1 - \frac{\bar{w}_1^2}{2c_p T_{\text{tot}}} \right)^{\frac{\kappa}{\kappa-1}} \right] \omega + 1 \quad (2.14)$$

Equations 2.13 and 2.14 can be used for substitution in the calculation of the *AVDR*.

$$AVDR = \left(\frac{\sin \bar{\beta}_2 \bar{w}_2}{\sin \bar{\beta}_1 \bar{w}_1} \right) \left(\frac{T_2}{T_1} \right)^{\frac{1}{\kappa-1}} \left(\frac{p_{\text{tot}, 2}}{p_{\text{tot}, 1}} \right) \quad (2.15)$$

3 Basic Principles

The experiments conducted for this work were designed to investigate the effects of a two phase flow in a compressor cascade. In the following, the principles of this type of flow are discussed.

3.1 Principles of Two-Phase-Flow

A two phase flow is only one example of multiphase flows. Crowe et al. argue in [45] that the overarching term for this kind of flows is the multicomponent multiphase flow. A component is a chemical species such as oxygen or nitrogen. A dry airflow is consequently to be treated as a multicomponent flow. In practice this is realized by using the physical properties that represent the mixture of the single components. The term phase refers to the condition of aggregation of the component. These conditions of aggregation can be gaseous, liquid or solid. The water droplet laden flow investigated in this work consists of a multicomponent gaseous phase and a liquid dispersed single component phase. It is therefore referred to as a gas-droplet flow.

3.1.1 Continuous Phase

Under the assumption of an adiabatic test rig and constant fluid properties, the behavior of the continuous phase can be described by the Navier-Stokes equations in vectorial form. The Navier-Stokes equations are presented in numerous publications in great depth, e.g. [46]. The equation of continuity is given by:

$$\frac{D\rho}{Dt} + \rho \left[\frac{\partial u}{\partial x} + \frac{\partial v}{\partial y} + \frac{\partial w}{\partial z} \right] = 0. \quad (3.1)$$

The equations for momentum in all three directions are:

$$\text{x-direction} \quad \rho \frac{Du}{Dt} = f_x - \frac{\partial p}{\partial x} + \left(\frac{\partial \tau_{xx}}{\partial x} + \frac{\partial \tau_{yx}}{\partial y} + \frac{\partial \tau_{zx}}{\partial z} \right), \quad (3.2)$$

$$\text{y-direction} \quad \rho \frac{Dv}{Dt} = f_y - \frac{\partial p}{\partial y} + \left(\frac{\partial \tau_{xy}}{\partial x} + \frac{\partial \tau_{yy}}{\partial y} + \frac{\partial \tau_{zy}}{\partial z} \right), \quad (3.3)$$

$$\text{z-direction} \quad \rho \frac{Dw}{Dt} = f_z - \frac{\partial p}{\partial z} + \left(\frac{\partial \tau_{xz}}{\partial x} + \frac{\partial \tau_{yz}}{\partial y} + \frac{\partial \tau_{zz}}{\partial z} \right). \quad (3.4)$$

and the energy equation is given by:

$$\rho \frac{DH}{Dt} = - \left(\frac{\partial q_x}{\partial x} + \frac{\partial q_y}{\partial y} + \frac{\partial q_z}{\partial z} \right) + \frac{U^2}{c_p \Delta T} \left[(uf_x + vf_y + wf_z) + \frac{\partial}{\partial t} + D \right]. \quad (3.5)$$

In this D is the dissipation, given by:

$$D = \frac{\partial}{\partial x} [u\tau_{xx} + v\tau_{yx} + w\tau_{zx}] + \frac{\partial}{\partial y} [u\tau_{xy} + v\tau_{yy} + w\tau_{zy}] + \frac{\partial}{\partial z} [u\tau_{xz} + v\tau_{yz} + w\tau_{zz}]. \quad (3.6)$$

Gravity is neglected in this set of equations as the kinetic energy exceeds the potential energy by far due to the high velocities in the investigated flow.

The velocity of the turbulent flow can be defined as the sum of the regular main velocity and the fluctuating, random part. This is formulated for the x-direction as:

$$u = \bar{u}(x, y, z, t) + u'(x, y, z, t) \quad (3.7)$$

and in an analogue manner for the y-direction and the z-direction. The turbulence of a flow can then be determined by:

$$Tu = \frac{\sqrt{\frac{1}{3}(\bar{u}'^2 + \bar{v}'^2 + \bar{w}'^2)}}{u_\infty} \quad (3.8)$$

In the case of a (quasi-) two-dimensional flow Equation 3.8 can be rewritten as:

$$Tu = \frac{\sqrt{\frac{1}{2}(\bar{u}'^2 + \bar{v}'^2)}}{u_\infty}. \quad (3.9)$$

The no-slip-condition at the blade surface demands that the velocity of the flow perpendicular to the blade surface is $v_{y=0} = 0$. The velocity difference towards the free flow is overcome by a boundary layer. The development of this is determined by intermolecular friction. In the case of an airfoil shaped body, in contrast to a flat plate, the pressure is a function of the

position $p = f(x)$. The equations that describe the boundary layer are a special case of the Navier-Stokes-equations and are often referred to as Prandtl's boundary layer equations for compressible fluids. These equations have been formulated in numerous publications (e.g. [47]).

$$\frac{\partial(\rho u)}{\partial x} + \frac{\partial(\rho v)}{\partial y} = 0 \quad (3.10)$$

$$\rho \left(u \frac{\partial u}{\partial x} + v \frac{\partial u}{\partial y} \right) = -\frac{\partial p}{\partial x} + \frac{\partial}{\partial y} \left(\eta \frac{\partial u}{\partial y} \right) \quad (3.11)$$

$$\rho c_p \left(u \frac{\partial T}{\partial x} + v \frac{\partial T}{\partial y} \right) = u \frac{\partial \rho}{\partial x} + \frac{\partial}{\partial y} \left(\lambda \frac{\partial T}{\partial y} \right) + \eta \left(\frac{\partial u}{\partial y} \right)^2 \quad (3.12)$$

The pressure inside the boundary layer is independent from the distance normal to the surface. The pressure gradient is exerted upon the boundary layer by the free flow. It is given by:

$$\frac{\partial p}{\partial x} = -\rho_\infty u_\infty \frac{\partial u_\infty}{\partial x} = \rho_\infty c_p \frac{\partial T_\infty}{\partial x}. \quad (3.13)$$

For the evaluation of the aerodynamic behavior of an airfoil or blade geometry, the knowledge of the boundary layer properties is mandatory. These properties are given:

$$\text{displacement thickness:} \quad \delta_1 = \int_0^\delta \left(1 - \frac{\rho}{\rho_\infty} \frac{u}{u_\infty} \right) dy \quad (3.14)$$

$$\text{momentum loss thickness:} \quad \delta_2 = \int_0^\delta \frac{\rho}{\rho_\infty} \frac{u}{u_\infty} \left(1 - \frac{u}{u_\infty} \right) dy, \quad (3.15)$$

$$\text{energy loss thickness:} \quad \delta_3 = \int_0^\delta \frac{\rho}{\rho_\infty} \frac{u}{u_\infty} \left[1 - \left(\frac{u}{u_\infty} \right)^2 \right] dy. \quad (3.16)$$

The displacement thickness describes the distance of displacement of the free flow from the surface of the body due to the boundary layer. The momentum loss thickness includes the mass flow in the evaluation and delivers therefore information, as the name implies, the loss of momentum in the flow due to the boundary layer. The kinetic energy loss is defined by additionally including the information about the velocity distribution, which converts the momentum equation into the equation for kinetic energy.

3.1.2 Gas Dynamics

The test configuration used in this work leads to local velocities that exceed the speed of sound. The development of shock waves and their effect on the flow field has to be discussed, consequently. A shock wave can be normal to the main flow direction. At an angle different from 90° in which case it is referred to as oblique, or a bow shock which develops at the leading edge of the blade at sufficiently high incident velocities.

Pressure disturbances travel at a characteristic speed through the flow field which is defined by (e.g. [37]):

$$a^2 = \left(\frac{\partial p}{\partial \rho} \right)_s. \quad (3.17)$$

For perfect gases this can be rewritten as $a = \sqrt{\kappa RT}$. In this κ is the ratio of specific heats $\kappa = c_p/c_v$. From this it is easily visible that the speed of sound increases with an increase in temperature.

If a series of pressure waves travels through a fluid, the first one will increase the pressure and consequently the temperature of the fluid which results in a higher speed of the subsequent waves. The following waves will consequently catch up to the first wave. As this holds true for every subsequent wave the marginal pressure increase of one single wave builds up to a shock front with a substantial pressure increase over a few free lengths of path of the molecules.

The change of state over a shock wave is irreversible. In the case of a strong normal shock wave, the velocity is reduced from $Ma > 1$ to $Ma < 1$. The governing equations to describe the change of state as a function of the incident Ma number have been given by many authors (e.g. [48]).

$$\frac{\hat{p}}{p} = 1 + \frac{2\kappa}{\kappa + 1} (Ma^2 - 1) \quad (3.18)$$

$$\frac{\hat{T}}{T} = \left[1 + \frac{2\kappa}{\kappa + 1} (Ma^2 - 1) \right] \left[1 - \frac{2}{\kappa + 1} \left(1 - \frac{1}{Ma^2} \right) \right] \quad (3.19)$$

$$\frac{\hat{c}}{c} = 1 - \frac{2}{\kappa + 1} \left(1 - \frac{1}{Ma^2} \right) \quad (3.20)$$

These equations represent the special case of a perpendicular orientation of the shock to the main flow direction. In many applications a shock will be induced by the geometry of a body in the flow which is likely to provoke an oblique shock. The relevant property of the incident flow is then the

incident Ma number normal to the shock. When the angle between incident flow and the shock is denoted by σ , the incident Ma number normal to the shock is $Ma^\perp = Ma \sin \sigma$. The change in incident Ma number normal to the shock causes a change in flow direction as the velocity component parallel to the shock remains unchanged. The change in flow direction is denoted by Θ and can be correlated to the shock angle σ .

$$\cot \Theta = \tan \sigma \left(\frac{\frac{\kappa+1}{2} Ma^2}{Ma^2 \sin^2 \sigma - 1} - 1 \right) \quad (3.21)$$

In the case of an inter-blade flow in a transonic compressor cascade a shock wave develops due to the blade geometry that induce transonic velocities. The configuration in Figure 3.1 shows that the shock is in direct contact to the boundary layer. As the shock is an abrupt deceleration of the flow and consequently a pressure increase this means an increase in stress for the boundary layer as discussed in the previous chapter. The boundary

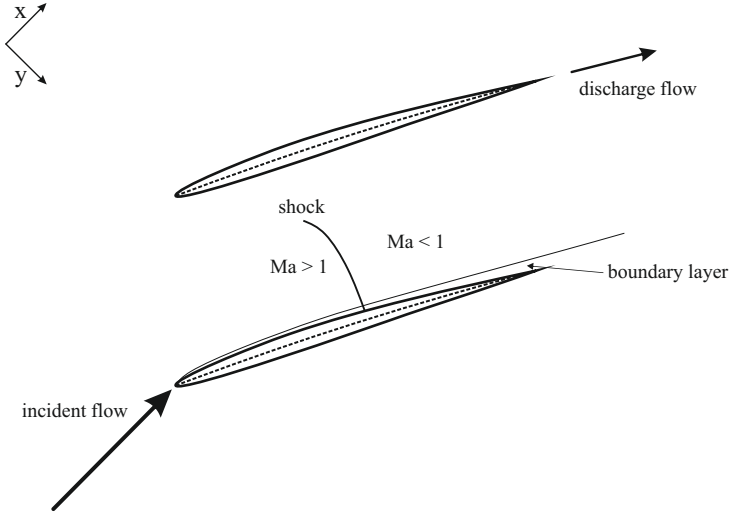


Figure 3.1: Transonic flow conditions: interblade shock configuration

layer shock interaction that springs from this configuration can have different consequences according to [47]. The presence of the shock can induce

the transition to a turbulent boundary layer and can also induce a flow separation. The key finding presented is, that a shock can fundamentally change the boundary layer properties. A detailed discussion of the influence the shock exerts on the boundary layer and the effects on the turbulence structures can be found in [49].

3.1.3 Dispersed Phase

The influence of the dispersed phase on the speed of sound can be assessed in two different ways. One way is to calculate the effective thermodynamic properties of the mixture of the fluids. This has been proposed by Brennen [50].

$$a_h = a_a \sqrt{\frac{1 + \chi \frac{c_d}{c_{p,c}}}{1 + \chi \frac{c_d}{c_{p,c}} (1 + \chi)}} \quad (3.22)$$

Under the assumption that the relative velocity between the continuous phase and the dispersed phase is negligible and the droplets are distributed homogeneously, the speed of sound can be defined analogously to a single phase flow. Oertel develops in [36]:

$$a_h = \sqrt{\left(\frac{\partial p}{\partial \rho}\right)_s} \\ = \left[\rho_h^2 \left(\frac{1}{\rho_d^2 a_d^2} + \chi \left(\frac{1}{\rho_a^2 a_a^2} - \frac{1}{\rho_d^2 a_d^2} \right) - \left(\frac{\partial \chi}{\partial p} \right)_s \left(\frac{1}{\rho_a} - \frac{1}{\rho_d} \right) \right) \right]^{-0.5}. \quad (3.23)$$

The development of this equation demands the absence of material transport from one phase to the other and the change of state is isentropic.

In the case of water droplets in a dry air flow further assumptions can be made. The speed of sound in water and the density is much higher than in the homogeneous phase. With this Equation 3.23 can be rewritten:

$$a_h = a_a \frac{1 + \frac{\rho_a}{\rho_d} X}{\sqrt{1 + X}}. \quad (3.24)$$

The assumptions made above are quite substantial and they only hold entirely true for very fine sprays in flows that are not or very mildly accelerated.

The evaluation of both equations yields similar results. A significant change in the speed of sound is not induced by water loads in the range of 0%...2.1%. The resulting change in the speed of sound has been calculated to be < 1%.

3.2 Droplet Behavior

The droplet behaviour comprises three aspects. The droplet movement is determined by the forces acting upon it causing an acceleration. The acting forces also cause the second aspect of droplet behavior, deformation and eventually breakup of the droplet. The underlying mechanisms for droplet breakup will be discussed. A droplet that impacts on a solid object will interact with the surface. The modes of interaction and the consequences of an impact are the third aspect and will be described as well.

3.2.1 Droplet Movement

The dry air flow in a compressor cascade is subject to velocity gradients. The flow is accelerated upon entering the cascade reaching the maximum velocity in the high speed regime close to the suction side of the blade and is then decelerated towards the discharge plane.

Droplets that represent the dispersed phase in a two phase flow will be subject to relative velocities as their inertia leads to a lower acceleration. The movement of a given droplet will be determined ultimately by the sum of the forces that act upon it. This is formulated by the momentum equation.

$$m \frac{du}{dt} = \sum_i F_i \quad (3.25)$$

In a uniform pressure field with a constant relative velocity between the droplet and the carrier gas, the drag force that acts upon the droplet is given by:

$$F_D = \frac{1}{2} \rho_c C_D \frac{\pi}{4} d^2 u_{\text{rel}} |u_{\text{rel}}|. \quad (3.26)$$

Herein C_D is the drag coefficient that is dependent on the shape and orientation to the flow as well as the flow parameters such as Mach number and Reynolds number. The relative velocity between the continuous phase and the dispersed phase is denoted by u_{rel} . The equation of motion for a

droplets given in [45]:

$$m \frac{dv}{dt} = 3\pi\eta_c D u_{\text{rel}} f + mg. \quad (3.27)$$

The acceleration due to gravity is denoted by g . The drag factor f is a function of the Reynolds number and the drag coefficient.

$$f = \frac{C_D Re_{\text{rel}}}{24} \quad (3.28)$$

The relative velocity demands the definition of a relative Reynolds number for the dispersed phase. It is given by:

$$Re_{\text{rel}} = \frac{\rho_c d |u_{\text{rel}}|}{\eta_c}. \quad (3.29)$$

The response time for a droplet to changes in velocity is given in [45].

$$\tau_v = \frac{\rho_d d^2}{18\eta_c} \quad (3.30)$$

In this η_c is the viscosity of the continuous phase. With this Equation 3.27 can be reformulated:

$$\frac{dv}{dt} = \frac{f}{\tau_v} u_{\text{rel}} + g. \quad (3.31)$$

The following correlations for the drag factor f have been formulated under the assumption of a spherical droplet.

$$f = \begin{cases} 1 + \frac{Re_{\text{rel}}^{\frac{2}{3}}}{6} & \text{for } Re_{\text{rel}} < 1000 \\ 0.0183 Re_{\text{rel}} & \text{for } 1000 \leq Re_{\text{rel}} < 3 \times 10^5 \end{cases} \quad (3.32)$$

This set of equations allows a description of the droplet movement in a homogeneous flow field. In the case of an inhomogeneous flow field additional forces have to be accounted for. The combination of these forces is known in literature as the Basset-Boussinesq-Oseen equation (BBO equation). A discussion of the terms of the BBO equation is given in the following.

The *Faxen force* accounts for the inhomogeneity of the flow. The correlation for the three dimensional case is given by:

$$F_{\text{Faxen}} = \eta_c \pi \frac{d^3}{8} \nabla^2 u. \quad (3.33)$$

In this, u is the flow velocity. This force reduces to zero for a homogeneous flow field as the velocity gradients disappear. Additional forces act upon the droplet due to pressure gradients. Under the assumption of a constant pressure over the particle volume V_d the force can be expressed by:

$$F_p = V_d \nabla p. \quad (3.34)$$

This force acts in the direction of the pressure gradient. If this force contributes significantly to the motion of the droplet can be estimated according to [45]. The pressure gradient in the continuous phase has the same magnitude as the flow acceleration. This is expressed by:

$$\frac{dp}{dx} \sim \rho_c \frac{du_c}{dt}. \quad (3.35)$$

The ratio of the pressure force to the force that is needed to accelerate a droplet is then:

$$\frac{V_d \frac{dp}{dx}}{m \frac{du_d}{dt}} \sim \frac{\rho_c \frac{du_c}{dt}}{\rho_d \frac{du_d}{dt}}. \quad (3.36)$$

Under the assumption that the acceleration of the continuous and the dispersed phase are of the same order, and the ratio of the densities of the dispersed phase and the continuous phase is in the order of 10^3 , the pressure force becomes negligible.

If relative acceleration of a droplet to the continuous phase takes place, other forces have to be accounted for as well.

The virtual mass force describes the force that is required to accelerate the fluid that is surrounding the droplet. The name of this force stems from the analogy to adding a virtual mass to the droplet which would result in the same correlation.

$$F_{vm} = \frac{\rho_c V_d}{2} \frac{du_{rel}}{dt} \quad (3.37)$$

The Basset force accounts for the delay in development of the boundary layer with changing relative velocity. It is sometimes referred to as the "history" term, because it depends on the acceleration history of the droplet. It is given by:

$$F_{Basset} = \frac{3}{2} d^2 \sqrt{\pi \rho_c \eta_c} \int_t^0 \frac{\frac{du_{rel}}{dt}}{\sqrt{t-t'}} dt'. \quad (3.38)$$

The importance of the Basset force and the virtual mass force can be determined by the evaluation of a combination of properties of the two phases and the flow. Crowe et al. report in a summary of the results obtained by Hjempfelt and Mockros (1966) in [45] that both forces become insignificant for $\rho_c/\rho_d \sim 10^{-3}$ if $(\eta_c/\rho_c\omega d^2)^{0.5} > 6$. In this ω is the frequency of the oscillating flow. Following the discussion in [31] these forces become only significant if a droplet travels through a shock wave which can only be the case for a negligible span of time.

Yet other forces have to be accounted for that are not represented in the BBO equation. The *Saffmann force* is induced by a velocity gradient over the droplet. The velocity gradient leads to a rotation of the droplet which results in a pressure distribution over the droplet. This ultimately leads to a lift force due to a pressure difference between two sides of the droplet. It was formulated by Saffmann and is given by:

$$F_{\text{Saffmann}} = 1.61\eta_c d |u_{\text{rel}}| \sqrt{Re_s}. \quad (3.39)$$

The shear Reynolds number is based on the velocity difference between two opposite sides of the droplet.

$$Re_s = \frac{d^2 du}{v_c dy} \quad (3.40)$$

Rotational movement of a droplet can also be due to collision with other droplets or rebound from solid surfaces. This results in the *Magnus force*. The correlation was derived by Rubinow and Keller and has been extended to account for flow rotation effects in [45]:

$$F_{\text{Magnus}} = \frac{\pi}{8} d^3 \rho_c \left[\left(\frac{1}{2} \nabla \times u - \omega_d \right) \times u_{\text{rel}} \right]. \quad (3.41)$$

3.2.2 Droplet Deformation and Droplet Breakup

The compressor flow is characterized by large velocity gradients in all three dimensions. In the case of the two dimensional flow in the linear cascade the gradients are limited to the main (axial) flow direction and the meridional direction. Large gradients exist at the stagnation point at the leading edge of the blade, in the high velocity regime on the suction side and in the deceleration zone in the inter-blade flow. This leads to a relative velocity between the dispersed and continuous phase as the water droplet, due to its inertia, has a limited ability to follow these gradients. The droplet size is the

main factor of influence in this context. As there is, in real sprays, always a droplet distribution present in the incident flow rather than a single droplet size, an average value for the droplet size will be used in the following to illustrate the behavior of all present droplets.

A number of different values are commonly used in this sort of setting, depending on the application. A comprehensive overview of this and other droplet atomisation topics is given by Wozniak in [51].

- d_{10} is the arithmetic mean value: $d_{10} = \frac{\sum d_d}{n_d}$
- d_{32} or SMD is the Sauter Mean Diameter: $d_{32} = \frac{\sum d_v}{\sum d_s}$
- d_{v10} indicates that 10% of the total liquid volume is distributed in droplets smaller than this value.
- d_{v50} indicates that 50% of the total liquid volume is distributed in droplets smaller than this value. This value is also called MMD or mass median diameter.
- d_{v90} indicates that 90% of the total liquid volume is distributed in droplets smaller than this value.

The arithmetic mean value is calculated as the ratio of the sum of all droplets in the specific control volume and the number of droplets. The SMD is the ratio of the sum of all droplet's volume and all droplet's surface.

The above mentioned relative velocity results in aerodynamic stress for the single droplet and can be described by the Weber number We :

$$We_{\text{dis}} = \frac{u_{\text{rel}} d_d \rho_{\text{da}}}{\sigma_d}. \quad (3.42)$$

In this u_{rel} is the relative velocity between the droplet and the surrounding flow, d_d is the droplets diameter, ρ_{da} is the density of the dry air and σ_d the surface tension of the liquid water droplet in air. The Weber number represents the ratio of the aerodynamic stress on the droplet and the surface tension.

Another dimensionless number is the Ohnsorge number which contains the relevant fluid characteristics of the droplet and can also be expressed in terms of the Weber number and Reynolds number.

$$Oh = \frac{\eta_d}{\sqrt{\rho_d d_d \sigma}} = \frac{\sqrt{We}}{Re} \quad (3.43)$$

Herein is η the droplet's dynamic viscosity.

The Ohnesorge number and the Weber number have been used by Pilch and Erdmann to formulate the deformation and breakup time for the droplet. They used a dimensionless time in the form of:

$$\tau = \frac{tu_{\text{rel}}}{d_0} \sqrt{\frac{\rho_d}{\rho_{\text{da}}}}. \quad (3.44)$$

The deformation time can be found by using:

$$\tau_d = 1.9(We_{\text{dis}} - 12)^{-0.25}(1 + (2.2Oh)^{1.6}). \quad (3.45)$$

The applicability for the droplet breakup time is determined by the Weber number:

$$\tau_{\text{dis}} = 6(We_{\text{dis}} - 12)^{-0.25} \quad \text{for } 12 < We_{\text{dis}} \leq 18 \quad (3.46)$$

$$\tau_{\text{dis}} = 2.45(We_{\text{dis}} - 12)^{-0.25} \quad \text{for } 18 < We_{\text{dis}} \leq 45 \quad (3.47)$$

$$\tau_{\text{dis}} = 14.1(We_{\text{dis}} - 12)^{-0.25} \quad \text{for } 45 < We_{\text{dis}} \leq 351 \quad (3.48)$$

$$\tau_{\text{dis}} = 0.77(We_{\text{dis}} - 12)^{-0.25} \quad \text{for } 351 < We_{\text{dis}} \leq 2670 \quad (3.49)$$

Aerodynamic stress, characterized by the Weber number, leads to a deformation of the droplet. For small Weber numbers this is a reversible process. A critical value $We_{\text{diss, crit}} = 12$ has been stated by Schmelz in [52]. For values around the critical Weber number, the droplet approaches its maximum diameter d_{max} . Above $We_{\text{dis, crit}} = 12$ droplet break up is initiated.

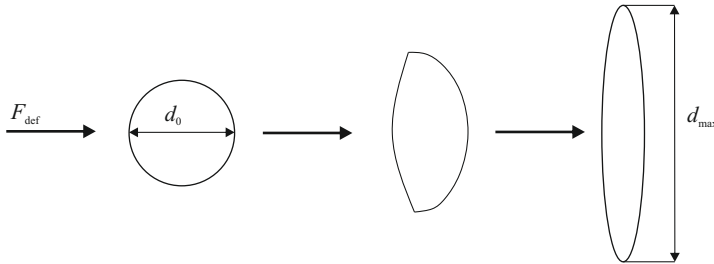


Figure 3.2: Droplet deformation process

Schmelz also investigated the progress of droplet break up. Different break up modi exist and the occurrence is determined by the Weber number. A summary is given in Figure 3.3

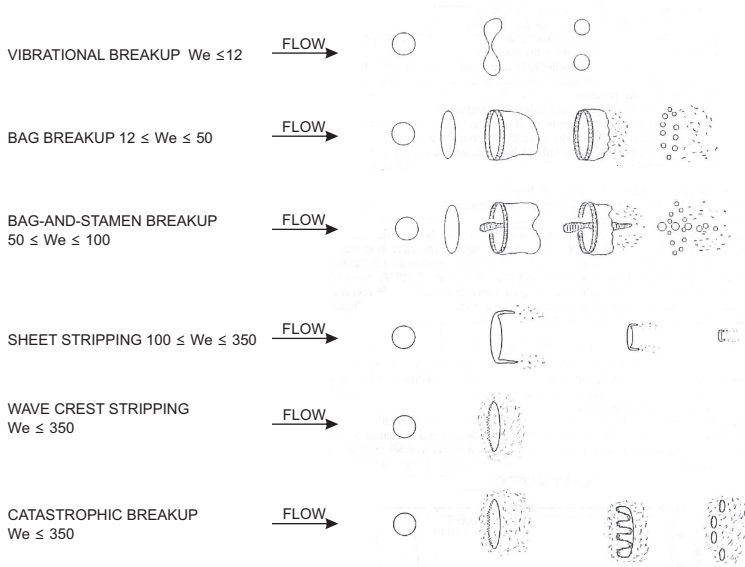


Figure 3.3: Breakup mechanisms as determined by We number

- For $We \approx 12$ an oscillating deformation of the droplet takes place. The oscillations that develop at the natural frequency of the droplet can overcome the surface tension and the droplet disintegrates into a small number of relatively large secondary droplets. This phenomenon is referred to as vibrational break up.
- For Weber numbers $12 < We_{\text{dis}} \leq 50$ bag breakup occurs. This phenomenon is analogous to the bursting of a soap bubble that is produced from a circular ring. The droplet is deformed and most of the water is concentrated in a torus. In the center a thin film in the form of a bag develops which quickly disintegrates due to aerodynamic forces. The remaining torus then splits into a low number of relatively large secondary droplets.
- Weber numbers of $50 < We_{\text{dis}} \leq 100$ lead to a faster deformation of the droplet. This shortens the time period in which the water can travel to the outer zone to form a torus. The result is a mixed mode

disintegration where a central stamen of water exists in addition to the torus and bag. This stamen is formed along the droplet axis parallel to the approaching flow. After the breakup of the bag, the stamen and torus disintegrate into a low number of relatively large secondary droplets.

- Sheet stripping is initiated for $100 < We_{\text{dis}} \leq 350$. Water, in the form of small droplets, is constantly transported from the droplet's edge, reducing its size. This is fostered by aerodynamic forces that deform the droplet's edge.
- Wave crest stripping is initiated for $We_{\text{dis}} < 350$ by small-wavelength and large amplitude waves that are formed at the windward facing side of the droplet. The wave crests propagate along the surface and are constantly eroded by the action of the flow field. Catastrophic breakup is triggered by long-wavelength and large-amplitude waves that penetrate the droplet. The droplet disintegrates into several fragments. These fragments undergo wave crest stripping as the Weber number for the fragments is still sufficiently high.

3.2.3 Droplet Wall Interaction

The interaction of a droplet with a solid wall plays a key role in many technical applications like ink jet printing, fuel injection in internal combustion engines or spray cooling.

First systematic investigations have been conducted as early as 1908 by Worthington [53]. Over 100 years of research in this field has broadened the knowledge and today the complexity of the accompanying phenomena is illustrated by the identified number of influencing parameters. The outcome of each droplet wall interaction is determined by the velocity, impact angle, temperature, fluid properties, ambient pressure and temperature as well as the surface properties. A more elaborate overview of the influencing parameters is given in Yarin [54].

In the context of a linear compressor cascade, droplet wall interaction primarily takes place on the blade surface. The curvature of the blade leads to a broad range of impact angles and consequently to a broad range of impact normal velocities. A set of dimensionless numbers is necessary to describe the impact scenario as presented in various publications (e.g. [54]).

$$We_{\text{imp}} = \frac{\rho_d d_d u_d^2}{\sigma}, \quad Re_{\text{imp}} = \frac{\rho_d d_d u_d}{\eta_d}, \quad Oh = \frac{\eta_d}{\sqrt{\rho_d \sigma d}} = \frac{We_{\text{di}}^{1/2}}{Re_{\text{di}}} \quad (3.50)$$

The droplet density is denoted by ρ , the droplet viscosity by η and σ is the surface tension. The droplet diameter is represented by d and the velocity by u . The Weber number describes the ratio of the inertial force to surface force. The Reynolds number represents the ratio of the inertial forces to the shear forces.

Rioboo et al. [55] investigated the droplet impact on a dry surface. The influencing parameters were systematically varied. In the first phase of droplet impact, referred to as the kinematic phase, the amount of water that is driven into a lamella and away from the impact zone shows a scaling behavior that only depends on impact velocity and droplet size. According to Yarin [54], six different outcomes of a droplet impact on a dry surface are to be distinguished.

- In the case of *deposition*, the droplet stays on the surface and spreads to a maximum, driven by inertial forces. Surface tension causes the final diameter of the resulting lamella to be smaller than the maximum diameter. This is determined by the Weber and Ohnesorge number.
- Rougher surfaces and higher impact velocities cause a *prompt splash* of the droplet. As in the case of *deposition*, a lamella spreads on the surface. In addition to that, small secondary droplets emerge from the spreading lamella of the droplet.
- Lower surface tensions lead to *corona splash*. The lamella detaches from the surface and takes the shape of a crown. Small droplets detach from the pointed edges of the crown.
- *Receding breakup* is characteristic for non-wettable surfaces. As in the *deposition* scenario, is the lamella shrinking after reaching the maximum size. During the shrinking process it breaks up into fingers driven by capillary instabilities. Each of these fingers is capable of further break up.
- If the remaining kinetic and surface energy of the lamella is sufficiently high after the lamella reached the maximum size, the lamella shrinks and pushes a part of the liquid upward from the surface in the shape of a column. The rest of the liquid stays on the surface and spreads out. This scenario is referred to as *partial rebound*.
- *Rebound* of a droplet is possible when the remaining energy is sufficient to lift the entire droplet from the surface. The droplet stays intact.

The distinguishing parameters for one of the scenarios to occur are a combination of surface and liquid properties, impact and ambient parameters. *Receding breakup*, *partial rebound* and *rebound* are relevant for low impact Weber numbers and low wettability surfaces and therefore not of primary interest for the work presented here.

Mundo [56] investigated the limits for deposition and splashing and formulated the K-factor for the impact on dry surfaces:

$$K_{\text{imp}} = We_{\text{imp}}^{0.5} Re_{\text{imp}}^{0.25} = \left(\frac{\rho_d^3 d_d^3 u_d^5}{\sigma_d^2 \eta_d} \right). \quad (3.51)$$

The threshold for deposition is given by $K_{\text{imp}} < 57.7$. Above this value prompt splashing is taking place. A threshold for corona splashing has not been given. In the context of a linear compressor cascade the most important findings presented by Mundo [56] are:

- The critical K factor for splashing on a dry surface is independent of the angle of impact for angles $> 60^\circ$
- Very high angles of impact ($80^\circ \dots 90^\circ$) and high impact velocities lead to chaotic break up of the droplet.
- The presence of a thin water film increases the critical K factor for splashing. Thicker water films lead to higher values for K_{crit} .
- Very low surface roughness ($\gamma = R_T \ll 10^{-3}$) results in higher critical K factors, effectively suppressing splashing.
- The droplet impact velocity determines the velocity of the secondary droplets.

The influence of the ambient pressure has been investigated by Xu et al. [57]. The results from their experiments show that corona splashing can be fully suppressed by lowering the ambient pressure. Below the threshold pressure, the droplet is fully deposited. The threshold pressure increases significantly for velocities $> 2 \frac{\text{m}}{\text{s}}$. The root cause for this phenomenon remains unclear up to the present. The existence of this regime however suggests that other characteristic regimes exist. The authors mention the case when the speed of droplet impact approaches the speed of sound in the gas as such a probable regime. The experiments were conducted in conjunction with a glass surface.

Compressibility effects play a role when impact velocities exceed a certain

threshold. Rein [58] and Lesser & Field [59] investigated droplets with $d_d \approx 200 \mu\text{m}$ impact at an impact velocity of $100 \frac{\text{m}}{\text{s}}$. The resulting Weber and Reynolds numbers are in the order of 10^4 to 10^5 . Under these conditions, shock waves are expected to propagate through the droplet. The shock wave is initiated upon impact and travels through the droplet. It overtakes the moving line of contact and this leads to spallation at the droplet bottom. The strength of the shock wave plays a key role for the erosive effects. It can be described by the Waterhammer equation $p_{\text{wh}} = \rho_d a_d u_d$. In this a_d and u_d are the speed of sound in the droplet and the droplet velocity upon impact.

Heymann [60] calculated, that in oblique impact scenarios, the pressure can be as high as $3p_{\text{wh}}$. In addition to the compressibility of the droplet, the compressibility of the surface was included in more recent models, e.g. by Surov & Ageyev [61].

The influence of the surface properties for the droplet behavior upon impact on a solid surface has been investigated by several research groups. Stow and Hadfield [62] studied the droplet impact on metal surfaces of varying roughness. The result is a well defined critical velocity for splashing in cases, where the roughness of the surface is small in comparison to the thickness of any developing water film.

The outcome of the droplet impact on a solid surface is also influenced by the number of droplets in a given control volume. Different research groups have investigated the influence of the interaction of adjacent droplets on the droplet impact outcome, e.g. Cossali et al. [63] found out that the interaction of spreading lamellas can lead to the uprising of fluid jets. Richter et al. [64] report that the interaction of two spreading lamellas lead to significantly larger secondary droplets.

The number of droplets that enters the cascade determines the number of impingement events per time per unit volume and therefore, in the case of a homogeneous spray with a single droplet diameter, the water mass per unit time that is deposited on the blade's surface. Above a certain threshold of impingement events per unit time the spreading diameter upon impact of the droplets exceeds the distance between the impact locations. The impinging droplets connect and a water film develops. More detailed descriptions of this behavior can be found in various publications (e.g. [65], [66], [67]).

The presence of several droplets that impact on the surface can therefore be treated as the impact on a partly wetted surface. As discussed in [54], the complexity of the impact scenario also depends on the surface proper-

ties. Especially the presence of a water film on the surface influences the complexity of the splashing event. Splashing on thick water films will be neglected in the following, because it is regarded as non relevant in the scope of this study.

Yarin and Weiss [68] found a threshold velocity for splashing of droplets that impact as a droplet train on a solid surface with the frequency f . It is given by:

$$u_{d,crit} = 18f_{imp}\eta_d \left(\frac{\sigma}{\rho_d} \right)^{1/4}. \quad (3.52)$$

For velocities above this threshold, which is independent of the droplet diameter, splashing and crown formation takes place. Below the threshold deposition takes place. According to [54], the independence of the threshold velocity from the droplet diameter indicates that the crown originates from the liquid lamella on the surface.

The impact of a single droplet on a pre-wetted surface was studied by Cossali [69] and Rioboo [70]. They also found crown formation and therefore splashing for sufficiently high impact velocities. The result of the experimental investigations of Cossali et al. is a threshold value for K for the droplet impact on a pre-existing film:

$$\begin{aligned} K &> K_{crit} = 2100 + 5880H^{1.44}, \\ 0.1 &< H < 1, \quad Oh > 7 \cdot 10^{-3}. \end{aligned} \quad (3.53)$$

In this the dimensionless water film thickness is $H = h_0/d_d$. The height of the liquid film and the surface roughness play a key role in this discussion. The threshold value for K decreases for higher surface roughness as the propagation of the lamellae is hindered for sufficiently low ratios of liquid film heights to roughness amplitude.

The complexity of the underlying phenomena mirrors to the numerical simulation of the relevant mechanisms which are not yet able to fully predict experimental results.

Urban [71] investigated oblique droplet impact on a wetted surface experimentally and numerically. Goma [72] reports on the possibilities to numerically describe and predict the droplet impact on a wetted flat plate under conditions which are relevant to the work presented here. He concludes that relevant phenomena like the film thickness on the surface and the ejected secondary droplets can be predicted but improvements of the model are necessary.

3.2.4 Droplet Entrainment

The deposition of water on the blade surface as a result of droplet impact leads to a water film formation. Under certain circumstances, parts of this water mass flow reenter the flow at the suction side of the blade. This phenomenon is known as droplet carryover or entrainment.

There are different reasons for droplet carryover to take place [73].

- Droplets are knocked out from the water film at the crests of large scale waves as a consequence of the dynamic effect of the surrounding continuous phase on the water film. This is referred to as dynamic carryover.
- Droplets are knocked out of the film by other droplets impacting on the film. This is called droplet carryover.

It has also been noticed that the passage of a shock wave causes the entrainment of droplets from a thin liquid film into the free flow under the action of friction [74]. Archer investigated the process of shock droplet interaction [75]. He reports the existence of different stages of the entrainment process. The development of a vortex pair ultimately draws fluid into the flow field and instabilities cause the fluid to atomize.

Milton reports in [76] that the fluid viscosity and surface tension plays a key role in the entrainment process. He tested different fluids and found that wave building due to shear stresses took place for water and oil but not alcohol or gasoline. He also estimated the velocity of the entrained droplets to be 60%-70% of the free flow.

In the case of the experiments conducted for this work however the relative velocity between fluid and shock wave is different from the situations described above. The water that forms the liquid film impinges on the blade and is then transported towards the trailing edge. The termination point of the high speed regime is, in the case of a transsonic flow, the local position of the shock. Therefore the relative velocity between liquid film and shock is lower.

3.2.5 Water Film Formation

The impingement of water droplets on the blade surface leads to the splashing of a certain fraction of the droplets. The further progression of the impingement event is determined by the K-factor. Eisfeld [31] discussed this in a comparable setting in the analysis of a droplet impinging on the

leading edge of a compressor airfoil. He was able to visualize the splashing of a droplet upon the impact on the leading edge in operating conditions that are relevant for axial compressor operation.

The shape of the blade around the leading edge offers an impinging droplet a variety of impact angles. A surface normal to the vector describing the incidence flow can be found at the stagnation point leading to an impact angle of 90° . An impact of the droplet further downstream will happen under a smaller impact angle as determined by the contour of the blade. The impact angle $\alpha_{\text{imp}} = f(x)$ is therefore a function of the position x on the blade which converges towards $\alpha_{\text{imp},\text{min}} = 0^\circ$ when a droplet just touches the blade's surface on the suction side at the most elevated point of this surface.

The impact scenario and especially the amount of water that is deposited of the blade is determined by the impact angle. The amount of deposited water influences the formation of the water film on the blade.

When a water film comes into existence it is driven towards the trailing edge by shear forces that spring from the surrounding flow. These shear forces increase with increasing distance from the leading edge due to the typical Ma number distribution on the suction side of a compressor blade which is dominated by a high velocity regime. This leads to an acceleration of the water film.

Saber and El-Genk have investigated the behavior of accelerated liquid films in [77]. They report the breakup of the liquid film into rivulets when the liquid flow rate decreases below a certain threshold to maintain a continuous film. The necessary liquid flow rate is referred to as the minimum wetting rate (MWR). The minimum liquid film thickness (MLFT) is the film thickness at breakup.

Both, the MLFT and the MWR decrease with increasing gas velocities. The analogy to the test cases at hand becomes evident in Figure 3.4. The image shows a close up photograph of the water film that develops on the suction side of the outer cross section at the leading edge. The water film disintegrates into rivulets.

Analytical approaches to predict the point of film breakup have been presented based on a force balance at the stagnation point by Hartley & Murgatroyd [78], but these investigations did not incorporate the interfacial shear at the free surface.

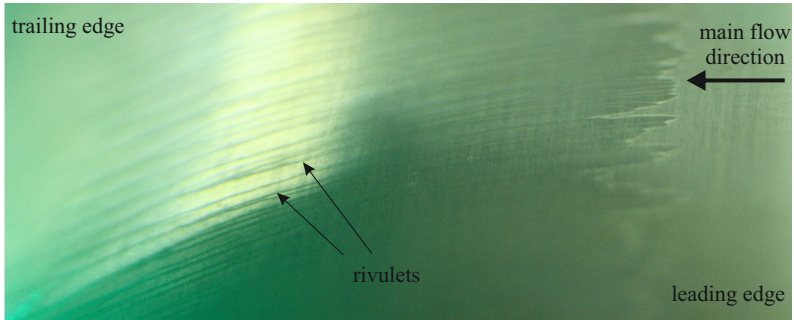


Figure 3.4: Water film on suction side with rivulets

3.3 Measurement Techniques

Standard pressure probes and thermocouples are used to verify the boundary conditions like periodicity and homogeneity of flow at the inlet and outlet plane of the test section. The most relevant data is gained by the means of optical, non-intrusive techniques. A two dimensional Laser Doppler and Phase Doppler Anemometer is used to record the velocity components of the flow. In the case of wet compression the droplet sizes are evaluated as well.

3.3.1 Laser Doppler/Phase Doppler Anemometry

In the course of the experiments conducted for this work a two dimensional Laser Doppler and Phase Doppler Anemometry (LDA/PDA) System by Dantec Dynamics has been used. The working principle of this measurement technique will be explained in the following.

Phase Doppler Anemometry (PDA) is an extension of the Laser Doppler Anemometry. Both are laser light based measurement techniques that use the doppler effect for non-intrusive measurements of velocity (LDA) and size (PDA) of particles that are present in a moving fluid. In the case of this work, the moving fluid is the continuous gas phase and the particles are water or oil droplets. Both techniques rely on light scattering and refraction and are therefore dependent on particles that reflect or scatter the light. The consequence of this is, that the relative velocity between continuous gas phase and the light scattering particles is sufficiently small to be

able to judge the flow properties of the continuous phase. This aspect will be addressed later in this chapter.

The theory of light scattering and reflection on particles has been formulated by Gustav Mie [79]. The underlying phenomenon for the type of measurement conducted in this work is the scattering of light on a single droplet. For the discussion, a basic model for the single incident ray of light and the spherical droplet is introduced in Figure 3.5. The incidence of monochro-

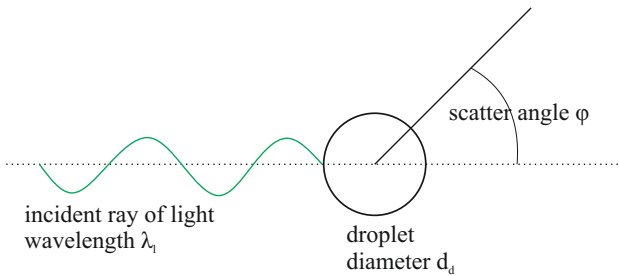


Figure 3.5: Light scatter of polarized light on a single droplet

matic light of a certain wavelength λ_i on a single particle or droplet results in the emission of scattered light. The scatter angle is denoted by φ . For the following discussion it is assumed, that the incident light is polarized and that its amplitude is perpendicular to the polarization direction. The absence of any electromagnetic field is also assumed. The intensity of the scattered light then varies with the scatter angle and can be determined by the sum of the single amplitudes. A function for perpendicular polarisation $S_1(\varphi)$ and parallel polarisation $S_2(\varphi)$ is given.

$$S_1(\varphi) = \sum_{n=1}^{\infty} a_n \Pi_n(\varphi) + b_n T_n(\varphi) \quad (3.54)$$

$$S_2(\varphi) = \sum_{n=1}^{\infty} a_n T_n(\varphi) + b_n \Pi_n(\varphi) \quad (3.55)$$

The Legendre functions $\Pi_n(\varphi)$ and $T_n(\varphi)$ are used here. In this, a_n and b_n are the partial wave amplitudes which can be obtained by:

$$a_n = \frac{2n+1}{n(n+1)} \frac{m\Psi_n(y_M)\Psi'(x_M) - \Psi_n(x_M)\Psi'(y_M)}{m\Psi_n(y_M)\Xi'(x_M) - \Xi_n(x_M)\Psi'(y_M)} \quad (3.56)$$

$$b_n = \frac{2n+1}{n(n+1)} \frac{\Psi_n(y_M)\Psi'(x_M) - m\Psi_n(x_M)\Psi'(y_M)}{\Psi_n(y_M)\Xi'(x_M) - m\Xi_n(x_M)\Psi'(y_M)}. \quad (3.57)$$

In this, Ψ_n and Ξ_n are the Ricatti Bessel functions of the first and third kind and the n^{th} order. The number of partial waves that are included in the evaluation determine the accuracy. An estimation for the necessary number for an error $< 10^{-7}$ is suggested:

$$n = x_M + 4.05x_M^{\frac{1}{3}} + 2. \quad (3.58)$$

The partial wave amplitudes are dependent on the Mie parameters x_M and y_M . These are given by:

$$x_M = \frac{\pi d_d}{\lambda_w} \quad (3.59)$$

$$y_M = mx_M = \frac{n_p}{n_m} \frac{\pi d_d}{\lambda_w}. \quad (3.60)$$

The refraction indices n_p and n_m are valid for the respective medium in combination with vacuum and can be combined to the refraction index m that is valid for refraction from one medium to the other.

Using the equations given above, the intensity of the scattered light as a function of the scatter angle can be displayed as in Figure 3.6a and Figure 3.6b (graphs provided by Dantec Dynamics A/S). The dependency of the scattering behaviour on the droplet diameter in relation to the wavelength is clearly visible. A droplet of the size in the order of the wavelength of the light produces a more constant intensity of the scattered light over the scatter angles than a droplet of a size $d_d \approx 10\lambda$. Highest intensities for the scattered light are yielded for $0^\circ \dots 30^\circ$ in any case. The Phase Doppler Anemometry (PDA) technique is an extension to Laser Doppler Anemometry (LDA) which allows the determination of the particle size. Following the same logic, the principles of LDA will be discussed first.

Basis for both measurement systems, LDA and PDA, is the coherent and monochromatic laser light source. The emitted light is split in two separate beams which are aligned to form an intersection under the angle Θ as

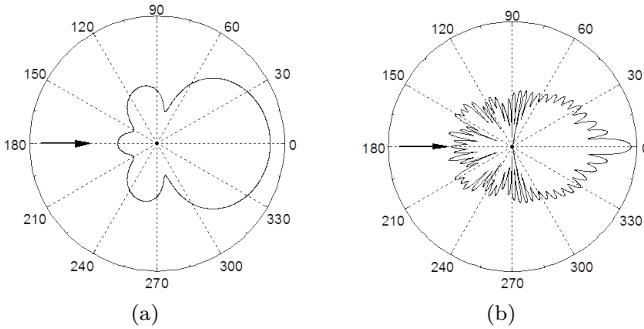


Figure 3.6: Intensity of scattered light as a function of scatter angle for $d_d = 1\lambda$ (a), $d_d = 10\lambda$ (b). (Dantec Dynamics)

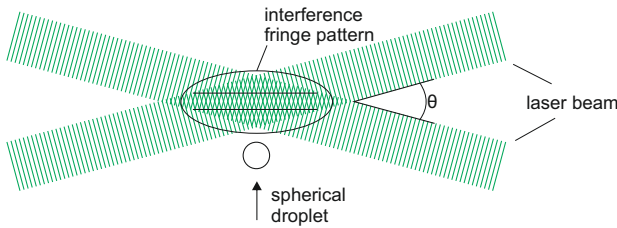


Figure 3.7: Principle of Laser Doppler Anemometry

shown in 3.7. The volume that is created by the intersecting light beams is the measurement volume. The monochromatic nature of the two light beams causes a fringe pattern of light and dark areas in the measurement volume. The fringe spacing is determined by the wavelength of the incident light and the angle of intersection. It is given by:

$$\delta_f = \frac{\lambda}{2 \sin \frac{\theta}{2}} \quad (3.61)$$

When a spherical droplet travels through the measurement volume, light is scattered with the frequency

$$f_{sl} = \frac{2u_d \sin \frac{\theta}{2}}{\lambda} = \frac{u_d}{\delta_f}. \quad (3.62)$$

With this the droplet velocity can be expressed as

$$u_d = \frac{f_{sl}\lambda}{2 \sin \frac{\Theta}{2}}. \quad (3.63)$$

This argumentation explains the correlation of the frequency of the scattered light and the velocity of the droplet but lacks the ability to determine the direction of the droplet. For this reason a bragg cell is used as a beam splitter to produce the two laser beams as the bragg cell applies a frequency shift to one of the laser beams. This frequency shift results in a moving fringe pattern in the measurement volume that is considered in determination of the droplet velocity:

$$u_d = \frac{(f_{sl} - f_s)\lambda}{2 \sin \frac{\Theta}{2}}. \quad (3.64)$$

Since the moving direction of the fringe pattern is known, this way the ambiguity with regard to the droplet's moving direction is overcome.

The advantage of this setup is the scattered light frequency's independence from the position of detection. The velocity reading is therefore independent from the position of the detecting device as well and a calibration is not necessary.

The frequency of the detected scattered light is independent of the detector's position but the phase changes with the alteration of the distance between droplet and detector. This effect is used to determine the size of the droplet. The Phase Doppler Anemometer uses two detectors as indicated in Figure 3.8. The angle ψ denotes their position which is turned out of the scatter plane. The angle between the incident laser beams and the detectors is denoted by φ . The signals that are recorded by the detectors are compared and a phase shift can be correlated to the size of a particle as follows [80]. Let $\Delta\Phi$ be the measured phase shift between the two detected signals. Considering the setup discussed above the phase shift is then:

$$\Delta\Phi = \frac{2\pi}{\lambda} d_d \beta_\varphi^i \quad \text{with} \quad (3.65)$$

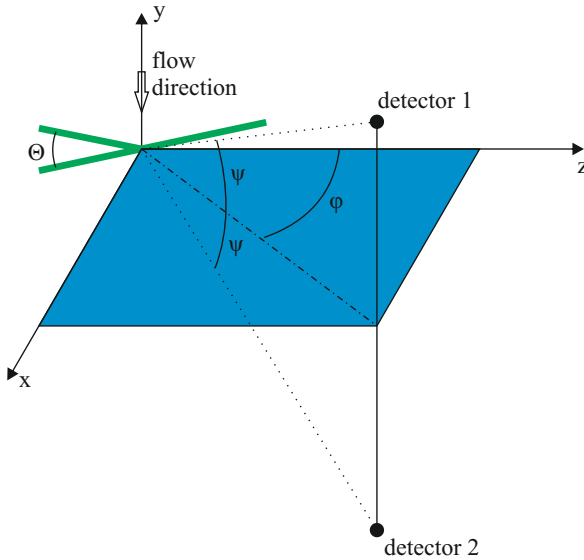


Figure 3.8: Principle of Phase Doppler Anemometry (Dantec Dynamics, 2006)

$$\begin{aligned} \beta_{\Phi}^2 &= \Delta\Phi_{E1} + \Delta\Phi_{E2} \\ &= 2 \left(\sqrt{1 + m^2 - m\sqrt{2}\sqrt{1 + \sin\psi \sin\left(\frac{\Theta}{2}\right) + \cos\psi \cos\varphi \cos\left(\frac{\Theta}{2}\right)}} \right. \\ &\quad \left. - \sqrt{1 + m^2 - m\sqrt{2}\sqrt{1 - \sin\psi \sin\left(\frac{\Theta}{2}\right) + \cos\psi \cos\varphi \cos\left(\frac{\Theta}{2}\right)}} \right). \end{aligned}$$

The coefficient β_{φ}^i is dependent on the dominant order of scattering. For $\varphi = 20^\circ \dots 60^\circ$, the first order of scattering is dominant. The known relative position of the two detectors allows the measured phase difference between the two detected signals to be correlated with the droplet diameter up to a phase shift of 2π . Beyond this threshold the phase shift becomes ambiguous. For this reason a third detector is positioned between the first two. The

comparison of the signals allows to eliminate this ambiguity. A more detailed description can be found in numerous publications (e.g. [80]).

The practical setup of the system consists of a laser light source, a receiving probe and a post processing unit as depicted in Figure 3.9. The LDA/PDA

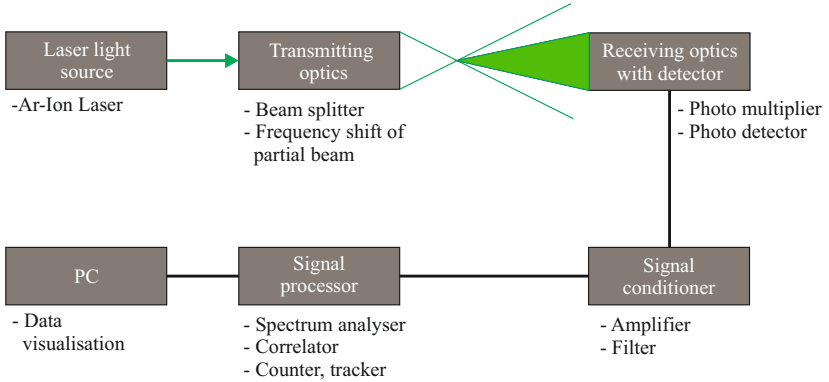


Figure 3.9: Principle setup of LDA/PDA (Dantec Dynamics, 2006)

has two main sources of uncertainty. The evaluation of the recorded Doppler bursts has an uncertainty of $\approx 1\%$ [81]. The slip velocity of the recorded droplets relative to the surrounding flow depends on the Stokes number and is the second main source of uncertainty. The evaluation of the maximal uncertainty as suggested in [82] for a velocity of $280 \frac{\text{m}}{\text{s}}$ yields a value of 6%. Dring's evaluation is based on a deflection of $\beta_1 - \beta_2 = 25^\circ$. Based on the lower design deflection of $\beta_1 - \beta_2 = 6^\circ \dots 13.9^\circ$ in the test cases presented in this work it is assumed that the uncertainty due to the slip velocity is $< 3\%$. The change in inlet Mach number due to water injection as yielded by the evaluation of Equations 3.22 and 3.24. will therefore be neglected in this study as the uncertainty of the measurement equipment exceeds the calculated changes in a .

3.3.2 LDA/PDA Data Acquisition

Two types of measurements are conducted in the course of this work. The determination of the cascade performance parameters is based on the measurement of the inlet and discharge flow properties. The investigation of the general alterations caused by water injection in the inter blade flow utilises

data that is gained from the measurement of a two dimensional grid in the inter blade passage.

In any case, the data acquisition for the 2D LDA/PDA is done in a point-to-point scheme. A measurement grid is tailored for each measurement and the anticipated flow properties, e.g. large velocity gradients, are incorporated in the definition of the measurement grid. For the evaluation of the aerodynamic performance of the cascade, the data collection of the flow properties at the inlet and at the discharge plane has to be conducted. For this, a front and back traverse was defined, according to Fig. 3.10. The one-

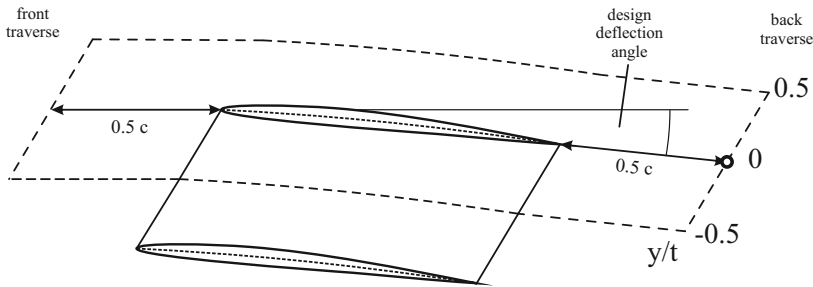


Figure 3.10: Measurement positions

dimensional grid consists of 100 points at the front and 140 points at the back traverse. The resolution is adapted to the anticipated area of interest by increasing the grid's resolution to 5 nodes per mm at the back traverse at $0 < y/t < 0.2$ as this is the wake area that showed the highest velocity gradients during test measurements.

In the dry case DEHS (Di-Ethyl-Hexyl-Sebacat) was injected as a seeding into the flow by two aerosol generators. The diameter $d_{v,90}$ of the generated droplets is $\bar{d}_d < 1 \mu\text{m}$. Droplets of this size follow the flow with negligible deviation [82]. Therefore the dry flow can be considered as the reference flow. 5000 particles are recorded for every position. In the case of water injection, a total number of 10000 particles are recorded to guarantee a sufficient number of particles in each droplet size class. In order to isolate the influence of water injection on the air flow, only particles smaller than $2 \mu\text{m}$ are evaluated in this case. Droplets larger than $2 \mu\text{m}$ will not follow the air flow without considerable deviation and will consequently not represent the air flow. The influence of large droplets on the air flow is therefore

included in the evaluation of the small ($<2 \mu\text{m}$) droplets.

In the case of the investigation of the inter blade flow, a two dimensional grid is used. The grid is generated by the use of a commercial grid generator software as part of CFD applications. The grid used in the measurements of the middle cross section is depicted in Figure 3.11. The blade contour is illustrated by the blue contour line. The grids used in this work comprise ≈ 2000 nodes each. The resolution is locally adapted to the velocity gradients in order to minimise the discretisation error. Measurement directly at the surface of the blade are not feasible. The laser light is reflected at the blade surface leading to erroneous measurements. The minimum distance of a measurement position to the blade surface is $s > 1 \text{ mm}$.

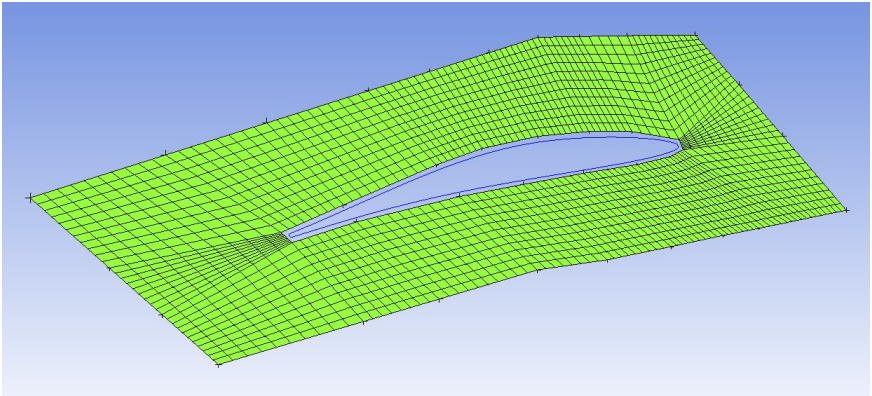


Figure 3.11: Measurement positions in the investigation of the interblade flow

3.3.3 Optical Measurement of Water Load

During the measurements a fraction of the injected water deposits on the side walls of the intake duct. In a measurement setup that uses mass flow rates to determine the water load this imposes an uncertainty that can only be mitigated, by a complete mass balance over the entire test rig.

Due to the constructional circumstances at the test rig, this requires substantial efforts. A practical way to measure the water load in the test

facility at the Helmut Schmidt University in Hamburg, Germany has been described by Eisfeld [31]. He adapted an optical measurement technique that relies on the scattering of light when traveling through a dispersed spray with known properties. The scattering of the light leads to a loss in intensity of the light beam. The comparison of the measured light intensity with a reference intensity delivers the information on the water load. The measurement principle is depicted in Figure 3.12. The setup consists of a

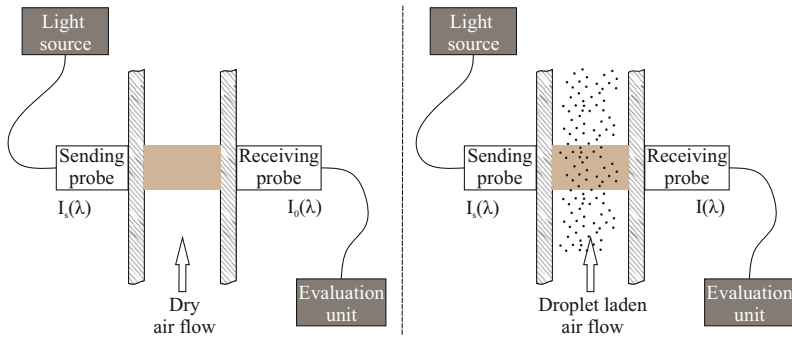


Figure 3.12: Measurement setup water load

light source, a sending probe, a receiving probe and a computer to evaluate the received signal.

The emitting and receiving probes are mounted directly opposite of each other in the side walls of the test section. The light is passed through a collimator to produce a light beam of defined diameter. The emitted light has the known intensity distribution $I_s(\lambda)$. The intensity distribution of the light beam at the receiving probe depends on the properties of the flow in the measurement volume. In case of the dry air flow without water droplets, the light intensity is defined as the reference function $I_0(\lambda)$. In case of the water laden flow the intensity is reduced due to scattering on the water droplets. The recorded light intensity $I(\lambda)$ is evaluated by a spectrometer. With the knowledge of the reference intensity function, the intensity function as a result of the droplet laden flow and other parameters, the correlation in form of the Bouguer-Lambert-Beer equation can be applied to

yield the water load.

$$-\frac{1}{L} \ln \frac{I(\lambda)}{I_0(\lambda)} = \frac{3}{2} C_v \int_{d_{d,\min}}^{d_{d,\max}} Q_{\text{ext}}(d_d, \lambda, m) \frac{\gamma(d_d)}{d_d} dd_d \quad (3.66)$$

In this, Q is the coefficient of extinction according to Mie's theory and C_v is the water load to be determined. The volume density distribution $\gamma(d_d)$ is gained from the PDA measurement that delivers the necessary values as a direct output. A more elaborate description of this technique can be found in [31].

This technique has been successfully used by Schatz & Casey [83] and Renner [84].

3.3.4 Shadowgraphy

Shadowgraphy is an optical method to visualise inhomogeneities in a transparent medium. It uses the different optical properties of any inhomogeneity in the surrounding medium in terms of transparency or light refraction behavior. In the test case at hand two inhomogeneities are present in the flow. Firstly, the injected water droplets refract part of the incident light resulting in dark spots on the image. Secondly, a shock wave develops under transonic flow conditions that refracts the incident light. This is visible as a dark structure in the shadowgraphy images. The setup consists of a conventional DSLR camera, a light source and a collimator lens. The light

Table 3.1: Shadowgraphy setup properties

Property	Value
Camera type	Canon EOS 450D DSLR
Max. resolution of recorded picture	4272 x 2848 Pixel
Objective lens	Macro 90mm F2.8
Distance to focus plane	0.3m
Maximum reproduction scale	1:1

source was a point flash lamp that produces mean illumination durations of $8ns$ with a single flash of $9mJ$. These parameters enable an efficient

image acquisition in a fast traveling, high density spray. The flash light was triggered by the DSLR. The whole setup is depicted in Figure 3.13. The

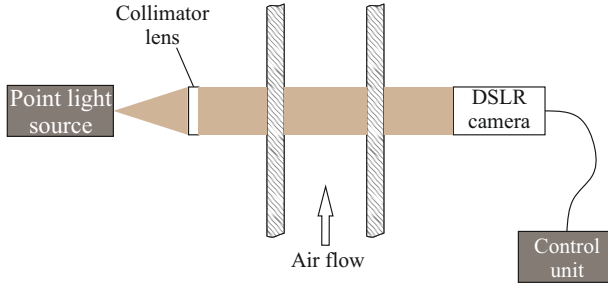


Figure 3.13: Shadowgraphy setup

objective lens used in this setup is capable of reproduction scales of up to 1:1. This enables the setup to display droplets that are in the same order of size as the camera chip pixels, ($< 5 \mu\text{m}$).

The whole setup is mounted on a traverse system to ensure an identical relative position among the setup's components in every measurement position. The traverse system and the image acquisition are controlled via separate applications that run on a standard PC.

4 Experiments Conducted

The two phase flow through a linear compressor cascade differs from the dry air flow in multiple aspects. In an attempt to identify the differences, several experiments have been conducted that aim at the different aspects of the flow.

All water droplets that are injected into the incident flow will interact with the gaseous phase and vice versa. The mode and extent of this interaction depends on the size and the relative velocity of the droplet to the surrounding flow at a given position in the test section. The effects of the presence of the dispersed phase however alters the flow properties of the cascade. The knowledge of these properties are key for the understanding of the necessity of stage matching procedures that arise from the application of water injection in multistage rotating machinery.

The experiments that have been conducted for this work can be divided in three parts that each aimed at a different goal.

- The *Phenomenological Experiments* aim at the understanding of the water flow on the blade surface and the identification of droplet disintegration phenomena. Focus points are the water film formation, droplet disintegration due to aerodynamic forces, droplet entrainment and the behavior of the water upon reentering the free flow at the blade's trailing edge. For these experiments, shadowgraphy and photography techniques are used.
- The *Investigation of the Inlet and Discharge Flow Properties* aim at the understanding of the influence of water injection on the flow properties at the inlet and discharge plane in order to determine the performance parameters of the cascade in each test case. For these experiments the 2D LDA/PDA setup was used to record the flow properties at the inlet and discharge plane of the cascade.
- The *Investigation of the Inter-blade Flow* aims at the deeper understanding of the alterations caused by water injection on the inter-blade flow. For these experiments the 2D LDA/PDA setup is used to record a grid of measurement points between the blades.

4.1 Phenomenological Experiments

Optical, non quantitative measurement techniques like shadowgraphy and photography are used for the phenomenological experiments.

Table 4.1: Phenomenological experiments conducted

Tested geometry	Inlet Ma number	Water Load	β_1
Outer cross section	0.8	1.3%	147°...154°
Middle cross section	0.78	1.3%	137°...146°

4.1.1 Investigation of the Water Film Formation

The investigation was carried out by the means of photography of the water film formation on the suction side of the blades. Both geometries, the outer and middle cross section were tested. A summary of the test conditions is given in Table 4.1.

The incidence angle was subject to variation within the boundaries of stable compressor flow. The tested range for the outer cross section was ($\beta_1 = 147^\circ \dots 154^\circ$) and ($\beta_1 = 137^\circ \dots 146^\circ$) for the middle cross section.

The photographs in figure 4.1 show the suction side of the outer cross section in the cascade configuration. The upper left picture represents the lowest incidence angle of $\beta_1 = 137^\circ$.

An area that is covered by a water film that originates from the leading edge is visible. The water is supplied by depositing water droplets. Further downstream this film deteriorates into rivulets that transport the water to the trailing edge of the blade. The break up of the film is initiated when the water film thickness falls below the minimum liquid film thickness (MLFT) as discussed in [77]. At this point it is energetically favorable for the film to break up into rivulets. The point of break up moves upstream with higher incidence angles. Two phenomena contribute to this behavior which are both triggered by the incidence flow angle.

The conditions in the boundary layer, that develops on the blade surface, have direct influence on the water film as it is located inside the boundary layer. A turbulent boundary layer exerts nonuniform stress on the water film, causing non uniform film thickness, ultimately leading to the deterioration of the film into rivulets when the MLFT is reached. The transition of a laminar to a turbulent boundary layer is dependent on multiple factors, the pressure gradient being one of these factors. The pressure gradient increases with higher incidence angles. This leads to an earlier transition of the boundary layer to a turbulent structure at higher incidence angles. This

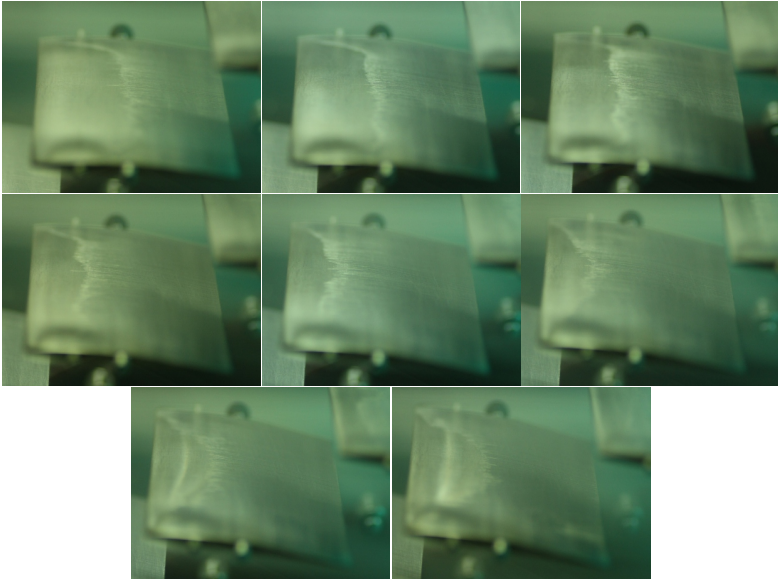


Figure 4.1: Water film formation on suction side of outer cross section. $Ma=0.8$, $X = 1.3\%$, $\beta_1 = 147^\circ \dots 154^\circ$

corresponds to the movement of the point of film deterioration to a further upstream position for higher incidence angles.

The second factor of influence to mentioned in this context is the water film thickness. The higher the initial water film thickness, the more intense disturbances are necessary for the film to break up. This is dependent on the amount of deposited water, which in turn is dependent on the droplet impact angle and the impact velocity as discussed in chapter 3.2.3. The amount of deposited water decreases with higher impact velocities. In this context only the velocity component normal to the surface plays a role, therefore the impact angle becomes key, which is dependent on the airfoil geometry. The outer cross section allows for a larger area with relatively low incidence angles (= low normal impact velocities for a higher amount of deposited water) compared to the middle cross section.

The area in the vicinity of the side walls show a shorter water film at higher incidence angles. The turbulent wall boundary layer causes an early transi-

tion of the boundary layer on the blade. This leads to a significantly earlier film breakup.

The water film formation on the surface of the second geometry (middle cross section) can be seen in Figure 4.2. The upper left picture shows the

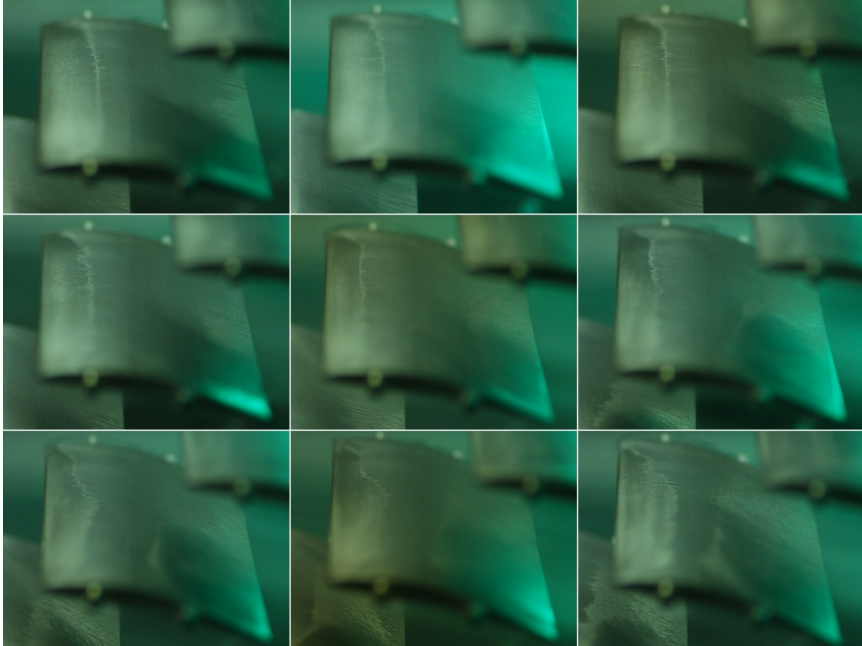


Figure 4.2: Water film formation on suction side of middle cross section $Ma=0.78$, $X = 1.3\%$, $\beta_1 = 137^\circ \dots 145^\circ$

water film at an incidence angle of $\beta_1 = 147^\circ$. In comparison to the outer cross section, the water film develops further downstream. This is the influence of the higher impact angles for the droplets in the area close to the leading edge which leads to a lower fraction of deposited water.

The water film breaks up into rivulets further downstream in this configuration as well, showing the same incidence angle dependent behavior as in the previous case.

4.1.2 Droplet Disintegration

A large fraction of the sum of forces that act upon a droplet in a compressor flow stems from the acceleration and deceleration. The largest forces in this aspect are triggered in transonic flow conditions, when a shock wave terminates the high speed regime on the suction side of the blade.

Droplet breakup due to the exposition of a single droplet to a shock wave has been reported repeatedly. The decomposition of non moving single droplets due to the exposition to a shock wave in a shock tube has been investigated by Boiko et al. [85]. Experiments on the behavior of liquid droplets traveling through shock waves have been undertaken and it was found that shock waves can result in droplet Weber numbers that are sufficiently high for droplet breakup (e.g. [86]).

Chang and Kailasanath [87] used a numerical method to predict the influence of a shock wave traveling through a two phase flow. They found, depending on the exact model used, that the shock wave was decelerated by the presence of the dispersed phase.

The applicability of these results in the setting of a linear compressor cascade is questionable due to the fundamental differences in flow properties. In the setup at hand, the droplet is continuously accelerated upon entering the cascade and is then abruptly decelerated upon passing through the shock that develops in the transonic test cases. The clarification of the presence of such droplet disintegration phenomenon in this setup was one of the aims of this series of experiments as the droplet size distribution is directly influenced by this, which in turn influences the cascade discharge properties. In order to clarify the presence and the extent of droplet breakup, a series of shadowgraphy experiments has been conducted.

The second mode of interaction of a droplet with the surrounding flow is the secondary disintegration due to aerodynamic forces. Secondary disintegration is triggered by high aerodynamic stress which can be described by the Weber number We . The Weber number is determined by the ratio of aerodynamic forces and the surface tension of the droplet (see Eq. 3.42). High aerodynamic forces can be observed in areas where high velocity gradients are present as the relative velocity directly influences the Weber number. In the case of a compressor flow, the highest gradients in the free flow can be found in the acceleration area upstream of the high velocity regime on the suction side and at the termination point of the high speed regime as depicted in Figure 4.3. In this, the Ma number of the inter blade flow of the outer cross section at $Ma = 0.8$ is depicted for two incidence angles. The

typical high speed regime is clearly visible on the suction side of the blade. This regime is terminated by a high negative velocity gradient downstream and moves upstream for higher incidence angles.

Shadowgraphy images were taken to visualise the droplet behavior in the

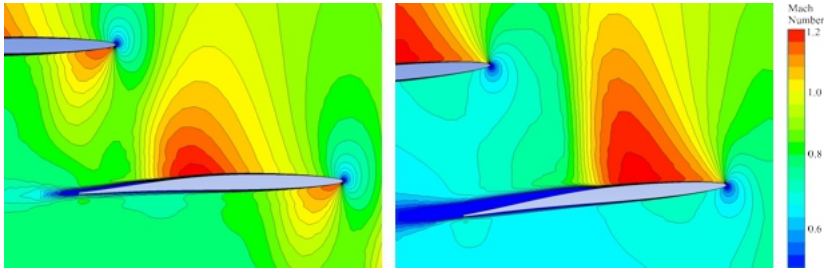


Figure 4.3: Simulated dry air flow: velocity contour plot $Ma=0.8$, $\beta_1 = 147^\circ$ vs $\beta_1 = 151^\circ$

inter blade passage. Figure 4.4 shows the inter blade passage of the outer cross section under transonic operating conditions. The shock that terminates the high velocity regime can be identified by the dark structures that spring from the suction side of the blade. The droplet distribution shows a homogeneous character in the free flow, but is less dense in the vicinity of the suction side. The droplet density in this area is reduced as the droplet size classes that are not able to follow the flow closely, due to their inertia are absent. However some large droplets are visible in this area. These spring from droplet entrainment that takes place in the vicinity of the shock. The abrupt deceleration of the surrounding flow causes an increase in water rivulet thickness which in turn causes crest building that results in droplets being carried away from the surface. Secondary droplet disintegration events can be identified in Figure 4.5, which is a magnified part of Figure 4.4. The shock in the central area of the picture terminates the high velocity regime. Various droplet disintegration events in different phases of the disintegration process can be observed. The location of the events relative to the shock suggest an occurrence of the disintegration triggered by aerodynamic forces in the acceleration regime upstream of the shock wave as well as by the deceleration when passing the shock wave. The typical shockwave-boundary-layer interaction is visible at the shock origin as well, which leads to a thicker boundary layer further downstream as discussed in [49]. Figure 4.6 illustrates the streak formation at the trailing

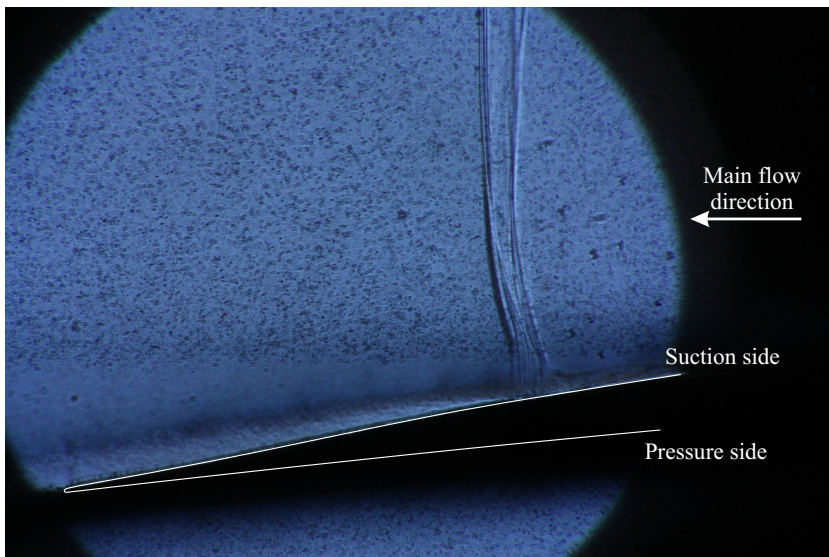


Figure 4.4: Shadowgraphy image of inter blade flow

edge of the blade. The deposited water is driven by the surrounding air flow and travels towards the trailing edge of the blade where it reenters the flow. The intensity of the streak depends on the incidence angle of the flow and the design flow deviation of the blade geometry. Both factors have an emphasising influence for higher values on the mass fraction of injected water that is concentrated in the trailing edge streak. In comparison to the surrounding free flow, the water travels at a low velocity, because it is in contact with the surface of the blade and naturally develops a boundary layer. This results in high relative velocities to the surrounding free air flow. The consequence is the development of a shear layer on the border between the streak and free air flow which causes the visible expansion of the water streak further downstream.

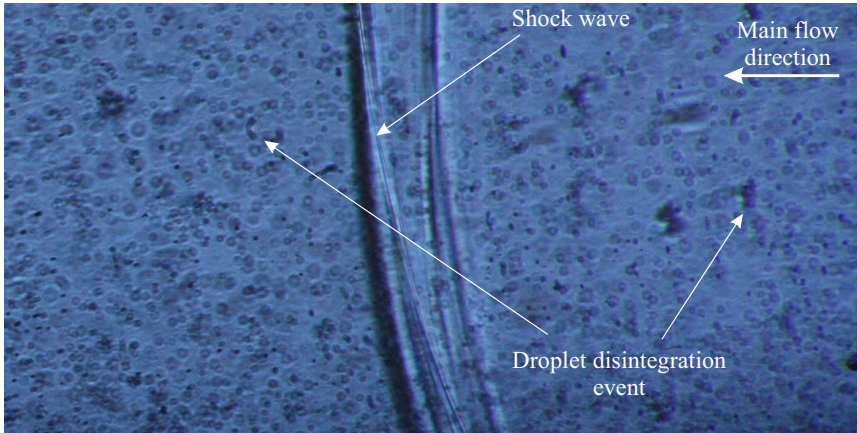


Figure 4.5: Secondary droplet disintegration in cascade flow

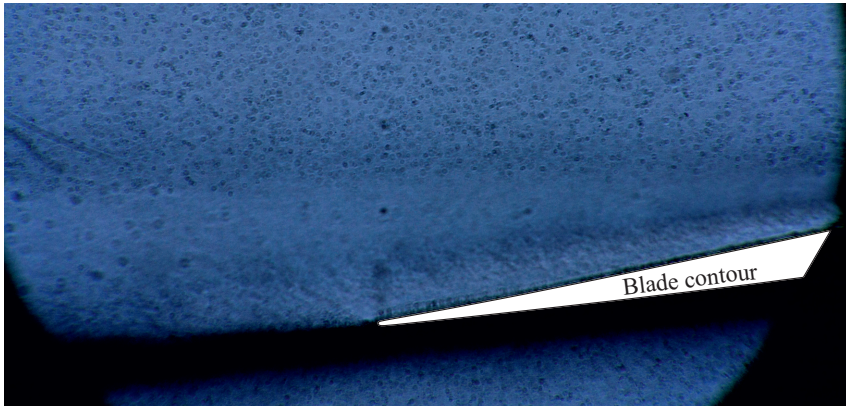


Figure 4.6: Streak formation in cascade discharge flow

4.2 Investigation of Cascade Discharge Properties

The discharge velocity and the discharge flow angle are the main factors for the determination of the loss coefficient. Therefore a detailed discussion of these parameters has to take place. The detailed effect on the loss coefficient and the AVDR will be discussed in chapter 4.3. The discussion presented here solely focuses on the influence on the discharge flow as the understanding of the underlying parameters is key for the discussion of the more complex evaluation of the loss coefficient and AVDR.

The analysis of the discharge properties is based on the measurements along the front and back traverse of the cascade. The 2D PDA system records droplet motion and size. The flow is evaluated by the use of the droplets $d_2 \leq 2 \mu\text{m}$ to ensure a minimal deviation from air flow. The dry air flow serves as a reference in these measurements.

4.2.1 Discharge Flow Velocity

The results presented below are based on measurements conducted on both blade geometries that have been derived from the middle and outer cross section of the rotor blade of an axial compressor, as discussed in chapter 2.2. Two different inlet velocities and water loads were tested over the entire spectrum of incidence angles as summarized in Table 4.2. A convention for the description of the different test cases will be used in the course of the following discussion for better readability. The first character indicates the used airfoil geometry (o = outer cross section, m = middle cross section). The next three characters indicate the inlet Ma number. The last characters indicate the water mass fraction. The code of this convention can be found in Table 4.2 as well.

Airfoil Geometry 1: Middle Cross Section Fig. 4.7a shows the discharge velocity profiles of case no. m078.0 at low incidence angles normalized to the inlet velocity for better comparability. Velocities form a uniform distribution apart from the wake in the area of $-0.1y/t$ to $0.05y/t$ which is characterized by a lower velocity. The mean values are close to 0.85 for the lowest incidence angle tested. Mean discharge velocities decrease with increasing incidence angles. This is due to the increasing flow deflection causing higher pressure ratios. The wake thickness is highest for $\beta_1 = 137^\circ$. The presence of a flow separation on the pressure side is likely in this case as the wake is extended to $-0.2y/t$. This and the high discharge velocity

Table 4.2: Experiments conducted

Inlet Ma number	Water Load	β_1	case no.
0.78	0%	137°...146°	m078.0
0.78	1.3%	137°...146°	m078.13
0.78	2.1%	137°...146°	m078.21
0.71	0%	137°...146°	m071.0
0.71	1.3%	137°...146°	m071.13
0.71	2.1%	137°...146°	m071.21

signals a misaligned incidence flow and consequently a small margin towards instability of the compressor flow. The discharge velocities for case no m078.13 at low incidence angles are depicted in Fig. 4.8a. In comparison to the dry case at low incidence angles the wake area shows a slightly increased thickness. The position of the lowest velocity moves towards the pressure side of the neighboring blade. A tendency towards higher discharge velocities can be noticed for $\beta_1 = 138^\circ \dots 141^\circ$. The cascade flow of $\beta_1 = 137^\circ$ incidence angle results in a smaller wake than in the dry case. Especially the pressure side seems to benefit in this case as the shape of the wake area is significantly altered at $-0.2 < y/t < -0.1$ while it remains unchanged at $y/t > 0$.

Fig. 4.7b depicts the normalized discharge velocity for high incidence angles. For $\beta_1 = 142^\circ$ the prevalent trend of lower discharge velocities and larger wake areas for higher incidence angles stays intact. The position of the lowest velocity in the flow moves further towards the pressure side of the neighboring blade. The shape of the wake structure indicates that $\beta_1 = 141^\circ$ and $\beta_1 = 142^\circ$ still result in a stable compressor flow, but the converging towards a maximum deceleration around $w_2/w_1 = 0.7$ suggests an operation close to the stability limit. This behavior changes for the higher incidence angles beginning at $\beta_1 = 143^\circ$, which results in a higher discharge velocity. For $\beta_1 = 143^\circ$ the wake area is significantly enlarged and displaced towards the pressure side of the neighboring blade. This is a clear sign of a flow separation on the suction side. The flow separation results in a reduced flow deceleration consequently in a higher discharge velocity. For $\beta_1 = 144^\circ$ the area of $0.05 < y/t < 0.5$ shows an extended wake in comparison to lower incidence angles. The velocity gradient over the entire discharge traverse is reduced. This can be interpreted as the behavior of

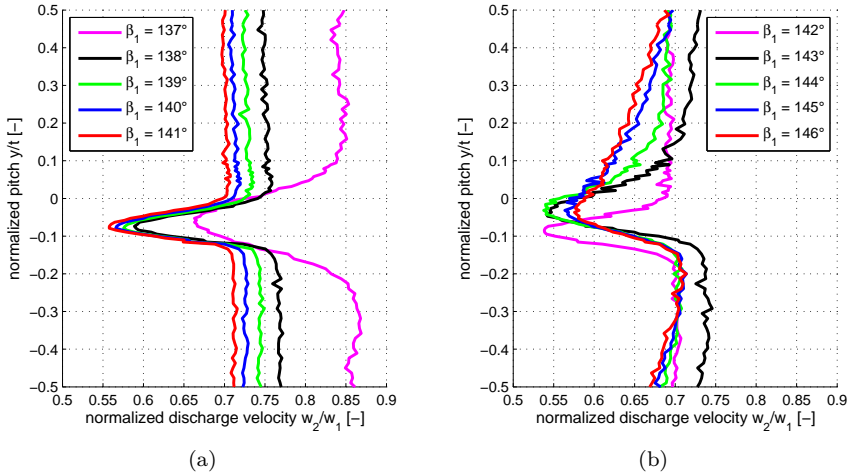


Figure 4.7: Case no. m078.0: measured normalized discharge velocity for low (a) and high (b) incidence angles

a more turbulent flow. The lower discharge velocities for $\beta_1 > 143^\circ$ as a sign of higher dissipation is a supportive argument to this assumption. But this theory cannot be proven as total pressure measurements could not be conducted due to the inaccuracy of total pressure probes in droplet laden flows. The highest incidence angles $\beta_1 = 145^\circ \dots 146^\circ$ result in a very similar velocity progression at the discharge plane. It is dominated by the further extension of the wake and, in comparison to $\beta_1 = 144^\circ$, a non altered velocity level.

Figure 4.8b depicts the discharge velocities for case no. m078.13 at high incidence angles. The velocity progression for $\beta_1 = 142^\circ$ outside the wake area remains unchanged in comparison to the dry case. The values for $\beta_1 = 143^\circ$ are lower, showing an improved deceleration behavior over the dry case. The difference between mean discharge velocity and minimum velocity inside the wake becomes smaller. The wake is smaller than in the dry case and is located at $-0.12y/t$ to $0.07y/t$. The absence of a wake dislocation (as seen in the dry case) and the improved deceleration suggest an improvement in terms of flow separation if not the absence of a detached flow. Higher angles of incidence only have an effect on the wake which grows with higher values for β_1 . The sensitivity of the discharge flow properties

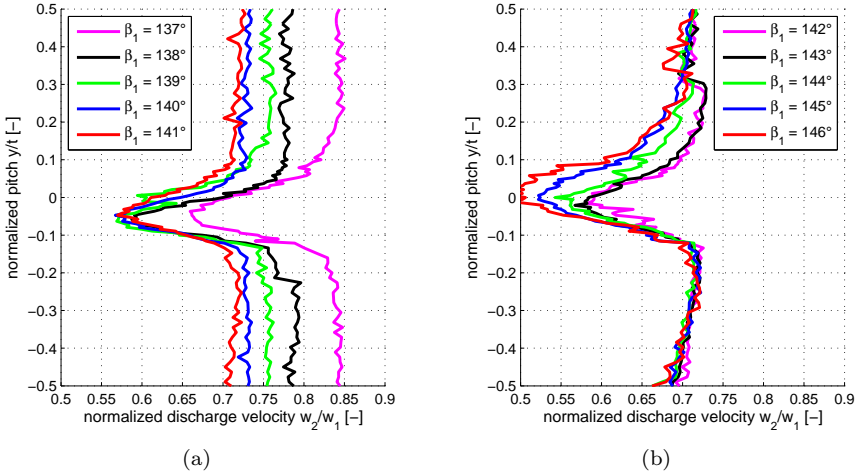


Figure 4.8: Case no. m078.13: measured normalized discharge velocity for low (a) and high (b) incidence angles

to the incident flow properties is lower in the case of water loading. While the shape of the wake shows significant differences for each incident angle in the dry case, these differences diminish in the wet case. The extent of the wake changes but the shape stays intact. This results in an almost identical velocity progression for $\beta_1 = 142\dots 146^\circ$ in the area $-0.5 < y/t < -0.1$. The fundamental shape alteration as seen in the dry case remains absent. Moreover are the minimal velocities inside the wake area higher in the wet case indicating lower momentum losses for $\beta_1 = 142\dots 143^\circ$. This behavior changes for the highest tested incidence angles where the velocity defect exceeds the values of the dry case.

The discharge velocity profiles for low incidence angles for case no. m078.21 are depicted in Figure 4.9a and will be compared to the previous case ($X = 1.3\%$) in the following. The measurements cover a smaller velocity spectrum while showing a generally higher level with the exception of the lowest incidence angle. The deceleration ability for $\beta_1 = 137^\circ$ has further improved over the $X = 1.3\%$ -case resulting in lower velocities. This is in accordance with the shape and size of the wake which is further reduced. This supports the assumption of a suppression effect on flow separations that originates from the presence of water droplets in the flow.

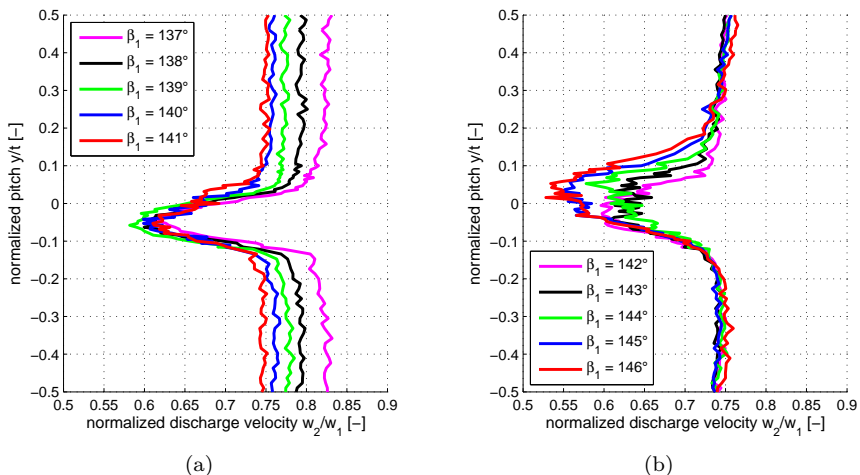


Figure 4.9: Case no. m078.21: measured normalized discharge velocity for low (a) and high (b) incidence angles

Higher incidence angles ($\beta_1 = 139^\circ \dots 141^\circ$) result in higher discharge velocities than in the previous case. The progression for $\beta_1 = 138^\circ$ only shows small deviations. The extent of deviation increases with incidence angle. The wake does not show a noticeable deviation to the previous case. Velocity readings for $X = 2\%$ and high incidence angles can be found in Figure 4.9b. The comparison with the previous case reveals a generally higher level of discharge velocities. The behavior of a constant discharge velocity for increasing incidence angles for $\beta_1 > 141^\circ$ is still present. The velocity progression inside the wake reveals a plateau of low velocities in the vicinity of the trailing edge. This results from water that disintegrates from the water film on the suction side of the blade and reenters the flow. The resulting acceleration of the droplets and the dissipation caused by high relative velocities lead to a larger velocity defect.

The discharge velocity profiles for low incidence angles of case no. m071.0 are displayed in Figure 4.10a. In comparison to case no. m078.0 the overall similarity of the progressions has to be pointed out. The evaluation of the DeHaller criterion delivers nearly the same values for $\beta_1 = 139^\circ \dots 141^\circ$. Minimal velocities inside the wake tend to be higher by $> 3\%$ (abs.). The shape and position of the wakes do not show noticeable deviations. Differences

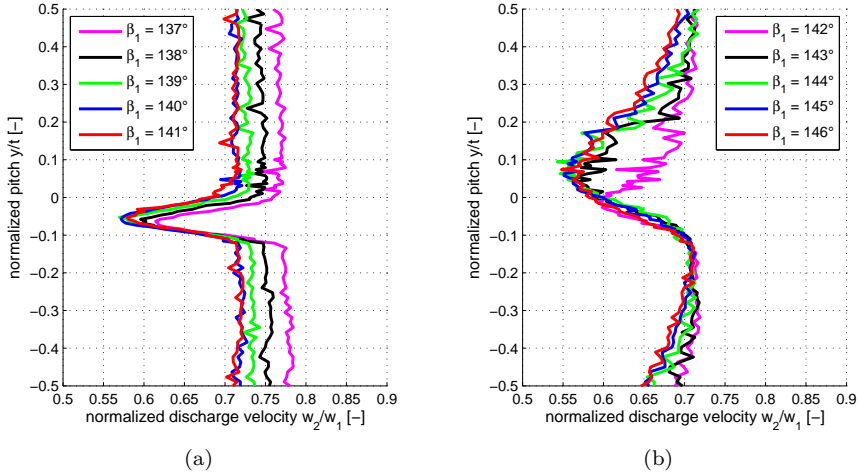


Figure 4.10: Case no. m071.0: measured normalized discharge velocity for low (a) and high (b) incidence angles

can be noticed for the lowest incidence angles. The cascade has a significantly higher deceleration ability for $\beta_1 = 137^\circ$ than in case no. m078.0. This supports the theory of a flow separation on the pressure side in case no. m078.0 which is amplified by higher inlet velocities and is consequently less present with a lower inlet Mach number. The same development on a smaller scale can be noticed for $\beta_1 = 138^\circ$ where the DeHaller criterion delivers lower values as well.

Figure 4.10b depicts the discharge velocity profiles for case no. m071.0 for high incidence angles. While the incidence flow of $\beta_1 = 142^\circ$ in case no. m078.0 resulted in a well defined velocity progression with a well developed wake, does the same incidence angle in this case lead to a flow separation structure. This is indicated by the extension of the wake on the suction side towards the pressure side of the neighboring blade. This behavior is amplified by higher incidence angles. The insensitivity of the discharge velocity profiles to higher incidence angles as seen in case no. m078.0 is present in this case as well.

In summary it can be pointed out that the cascade was more sensitive towards misaligned incidence flows in case no. m078.0 and produced a stable, presumably non detaching, flow for $\beta_1 = 142^\circ$ which was not possible in

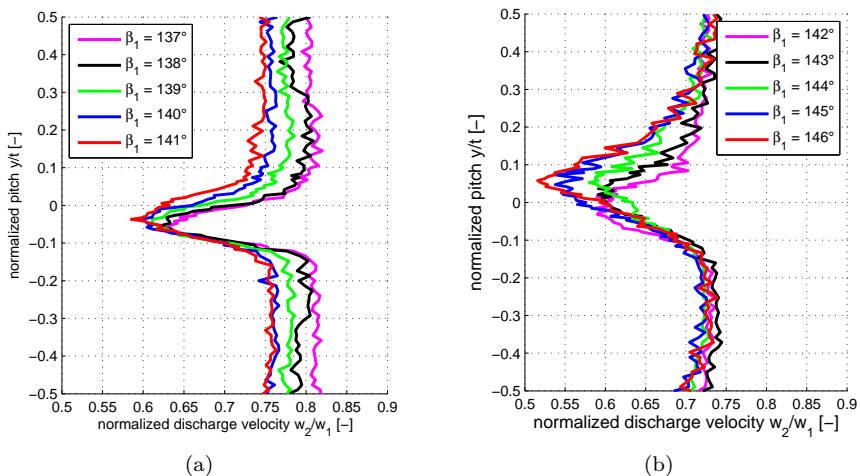


Figure 4.11: Case no. m071.13: measured normalized discharge velocity for low (a) and high (b) incidence angles

case no. m071.0.

The discharge velocity profiles for the case no. m071.13 and low incident angles can be found in Figure 4.11a. In comparison to the corresponding dry flow case an overall detrimental effect can be noticed. The mean discharge velocities are higher and the wake thickness is increased for every incidence angle. The evaluation of the DeHaller criterion results in higher values of $\approx 5\%$. The velocity defect $w_{2,m} - w_{2,\min}$ in the wake tends to be higher. The location of the wake does not show a noticeable difference. A fundamentally altered flow cannot be seen. The discharge velocity profiles for high incidence angles are depicted in Figure 4.11b. The tendency of a detrimental effect continues to be present. The discharge velocities are higher than in the dry case and the velocity defect in the wake is amplified by $\approx 5\%$. This behavior can be explained by water that was deposited on the blade and reenters the flow at the trailing edge. This water is accelerated by the surrounding flow causing a higher velocity defect. The amount of deposited water depends on the incidence angle. The extent of the velocity defect depends on the incidence angle as well, consequently. A difference can be noticed in the shape of the wake. While the dry test case results in a flow separation that results in a large wake area that extends to $y/t = 0.45$, the

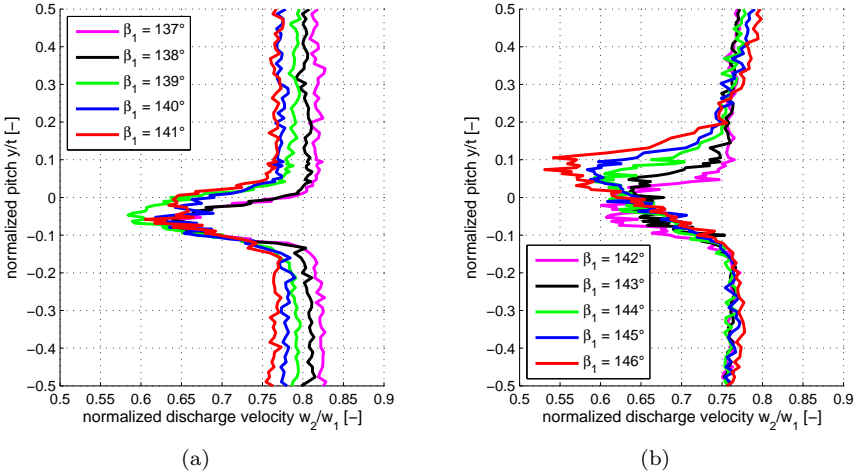


Figure 4.12: Case no. m071.21: measured normalized discharge velocity for low (a) and high (b) incidence angles

water laden flow produces a wake that is limited to $y/t = 0.3$. The reason for this is an impulse transport phenomenon. Water droplets reenergize the detaching flow due to their inertia resulting in a stabilized flow. The alteration seen in the comparison of the cases m071.0 and m071.13 can be again found in case no. m071.21 in Figure 4.12a for low incidence angles. The cascade's ability to decelerate the flow is further reduced by $\approx 2\%$ (abs.) and the wake thickness is further increased for $\beta_1 = 139^\circ \dots 141^\circ$. The position and the shape of the wake do not suggest a fundamentally altered flow pattern in comparison to the previous case.

The results for high incidence angles can be found in Figure 4.12b. A further reduced ability to decelerate the flow can be noticed again. Corresponding values for the normalized discharge velocity are consequently lower (up to 4%). The discharge velocities outside the wake show no sensitivity towards incidence angles $\beta_1 > 141^\circ$. This results in similar velocity progressions at $y/t = -0.5 \dots -0.1$ for all incidence angles. The graphs diverge in the wake area. For $\beta_1 > 142^\circ \dots 143^\circ$ a similar behavior to case no. m078.21 can be found which is characterized by the development of a plateau shape around the trailing edge. The discharge flow for higher incidence angles ($\beta_1 > 144^\circ \dots 146^\circ$) is dominated by a large wake that is displaced to the

pressure side of the neighboring blade. This behavior could be found in case no. m078.21 as well, but not to the same extent. The reason for this phenomenon has its cause in water that disintegrates from the suction side of the blade and reentered the flow. The increased sensitivity in this case can be explained by the lower velocity and therefore lower specific impulse of the surrounding flow which results in a higher relative impact of the droplets on the flow.

The results show that water injection results in a multitude of alterations in the discharge velocities. A summary of the effects for the middle cross section is given:

- Water injection is able to stabilize detaching flows for low incidence angles.
- Water injection leads to a limitation of flow separation on the suction side under high incidence angles.
- Water injection results in a thickened wake. The reason for this is threefold. First, the impacting water droplets disturb the boundary layer causing an earlier transition, leading to a thicker boundary layer. Second, the water reenters the flow at the trailing edge at low velocity and decelerates the flow. Third, the water that travels on the suction side causes an irregular surface structure.
- The overall ability to decelerate the flow by diffusion is reduced by the use of water injection.
- The extent of the stabilizing effect depends on the water load. A higher water load has a higher stabilizing effect. Detrimental effects however, if present (as seen for $(\beta_1 > 144^\circ \dots 146^\circ)$ in case no. m071.21), are amplified as well. A suitable combination of velocity versus water load determines the outcome.

Airfoil Geometry 2: Outer Cross Section The outer cross section of the same blade design was tested in a similar manner. The test cases are summarized in Table 4.3. A description of the test case convention was introduced in Paragraph 4.2.1.

The variation of the incidence angle was limited by blockage in the o87.xx cases. Figure 4.13a depicts the discharge velocity profiles for case no. o089.0.

Table 4.3: Outer cross section: experiments conducted

Inlet Ma number	Water Load	β_1	case no.
0.89	0%	149°...154°	o089.0
0.89	1.3%	149°...154°	o089.13
0.89	2.1%	149°...154°	o089.21
0.8	0%	148°...154°	o08.0
0.8	1.3%	148°...154°	o08.13
0.8	2.1%	148°...154°	o08.21

As seen in the previous cases, the discharge velocity shows an even distribution apart from the wake. The deceleration ability rises with increasing incidence angles. The increase in deceleration is highest between $\beta_1 = 149^\circ$ and $\beta_1 = 150^\circ$, where also the wake thickness is reduced. While the wake covers an area of $0.01 < y/t < 0.17$ for $\beta_1 = 149^\circ$, it is reduced to $0.02 < y/t < 0.12$ for $\beta_1 = 150^\circ$. A reduction in velocity deficit $w_{2,m} - w_{2,\min}$ of $\approx 2\%$ can also be noted for this 1° increment. These indicators suggest that the tested profile was operating close to the stability limit at $\beta_1 = 149^\circ$. The velocity profiles for $\beta_1 = 149^\circ$ and $\beta_1 = 150^\circ$ are similar to a large extent besides the lower discharge velocity for higher incidence angles.

The discharge velocity profiles for case no. o089.0 at high incidence angles can be found in Figure 4.13b. The trend of lower discharge velocities for higher incidence angles stays intact. The velocity profiles tend to converge for the highest tested incidence angles as it was seen in the test cases of the middle cross section. The extent of the wake increases significantly for incidence angles $\beta_1 < 152^\circ$. The expansion of the wake solely takes place on the suction side. The reason for this behavior can be found in the boundary layer shock interaction that causes an increased boundary layer thickness. This effect becomes more prevalent for higher incidence angles as the stress on the boundary layer due to the increasing pressure gradient increases. Figure 4.14a shows the discharge velocity profiles for case no. o089.13. The identified influences of water injection that were present in the previous cases can be again found in this case. For $\beta_1 = 149^\circ$ the normalized discharge velocity is increased by $\approx 3\%$. The wake thickness is decreased. While the wake covered $0.01 < y/t < 0.18$ in the corresponding dry flow case it covers $0.02 < y/t < 0.17$ in the current case. The velocity deficit in

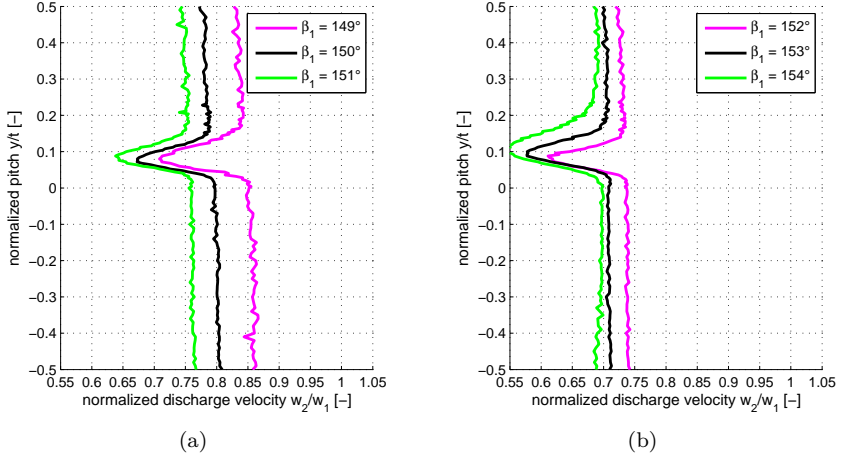


Figure 4.13: Case no. o089.0: measured normalized discharge velocity for low (a) and high (b) incidence angles

the wake increases as seen in the previous cases by $\approx 3\%$. Water injection causes an isolated effect on the wake at incidence angles $\beta_1 = 150\dots 151^\circ$. While the mean discharge velocities remain unchanged outside the wake, is the velocity deficit $w_{2,m} - w_{2,\min}$ and the wake thickness increased.

The profiles of the normalized discharge velocity for high incidence angles can be found in Figure 4.14b. The mean discharge velocity is not significantly affected by the presence of water droplets in the flow. The wake covers a larger area for higher incidence angles, as seen in case no. o089.0, but is still amplified over the dry case. The minimal velocities are lower in this case but converge to the unchanged minimal value of $w_2/w_1 = 0.55$.

A higher water load of $X = 2.1\%$ causes a less effective deceleration of the flow for $\beta_1 = 149^\circ$ as seen in Figure 4.15a. The mean discharge velocity is increased by $\approx 2\%$ (abs.). The velocity deficit and wake thickness does not change significantly. The higher incidence angles result in lower discharge velocities but on a higher level than in case no. o089.13. The wake thickness and position is not altered by an increase of the water load.

Figure 4.15b depicts the normalized discharge velocities for high incidence angles. The results show, that the alterations caused by water injection in the flow in case o089.13 can be found here as well in amplified form. The thickening effect on the wake serves as a good example. The position of the

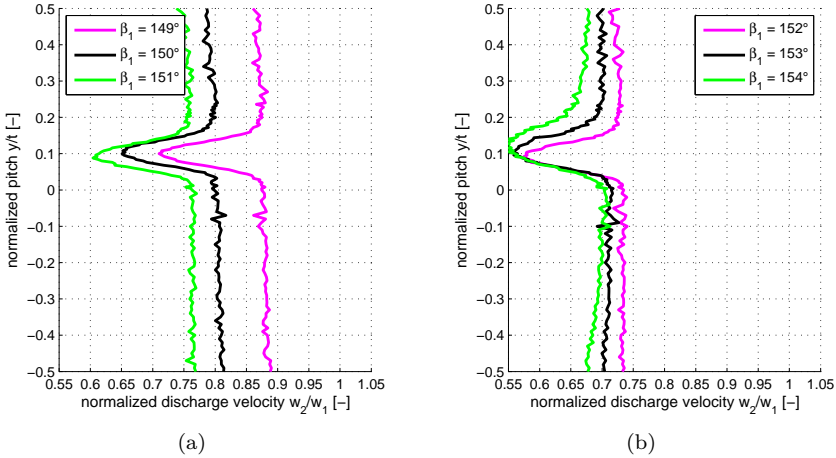


Figure 4.14: Case no. o089.13: measured normalized discharge velocity for low (a) and high (b) incidence angles

minimal velocity remains at $y/t = 0.11$. The velocity progression towards the pressure side of the neighboring blade describes a lower positive gradient the higher the water load is. This results in a heavily extended wake for $\beta_1 = 154^\circ$. The reason for this can be found in the amount of water that disintegrates from the suction side of the blade. Upon disintegration the water ligaments and droplets have a low velocity and consequently a high relative velocity to the surrounding flow. This distracts the airflow and leads to possibly higher dissipation. Discharge velocities are higher than in case o089.13 as seen for the low incidence angles.

The discharge velocity profiles for low incidence angles for case no. o080.0 are depicted in Figure 4.16a. The range of tested incidence angles could be increased for inlet Ma number of 0.8 as the blockage effect as seen in case no. o089.0 is not as prevalent. The DeHaller number for the $\beta_1 = 147^\circ$ is close to 1. This indicates that flow deceleration and pressure increase does not take place. The cascade operates at the choke line. The wake shows an expansion towards the suction side of the neighboring blade. This behavior was also noticed in case no. m078.0. The discharge velocity profiles resulting from incidence angles $\beta_1 = 148^\circ \dots 150^\circ$ show a smaller wake thickness and similar progression. The expansion cannot be noticed anymore. The DeHaller number decreases with increasing incidence angles.

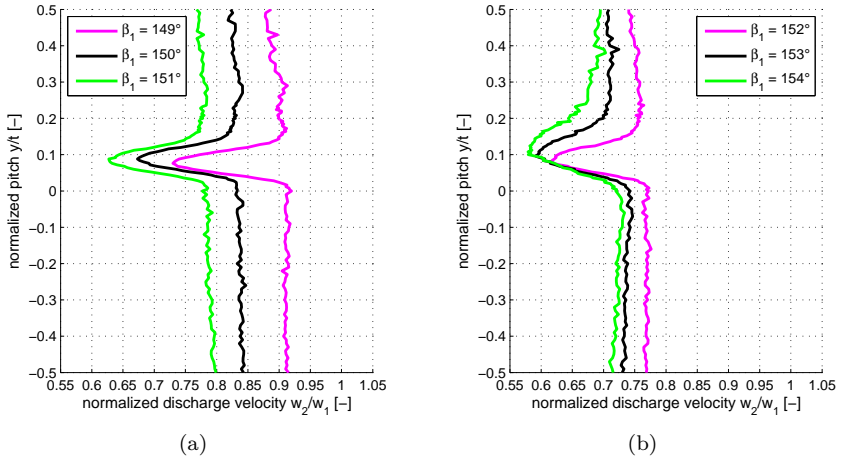


Figure 4.15: Case no. o089.21: measured normalized discharge velocity for low (a) and high (b) incidence angles

Figure 4.16b depicts the discharge velocity profiles for case no. o080.0 at high incidence angles. The cascade operates in a similar way as seen in case o089.0. The DeHaller number decreases with increasing incidence angles. The wake thickness increases with increasing incidence angles. The velocity deficit inside the wake is not as high as in case no. o089.0. A large displacement of the wake as seen in the test cases of the middle cross section at high incidence angles cannot be noticed.

Figure 4.17a depicts the discharge velocity profiles for low incidence angles in case o080.13. The comparison to case no. o080.0 shows that water injection does not have a significant influence on the flow outside the wake. The flow passes the discharge plane at the same velocity as in case no. o080.0. A difference between the two cases can be found in wake thickness and velocity deficit. Wake thickness is increased for $\beta_1 = 148^\circ \dots 150^\circ$ by 2...3% by the presence of water droplets in the flow while it remains unchanged for $\beta_1 = 148^\circ$. The velocity deficit $w_{2,m} - w_{2,\min}$ is significantly increased for all incidence angles by about 5%. The increased velocity deficit can again be explained by water that disintegrates at the trailing edge.

The velocity profiles for high incidence angles in case no. o080.13 are depicted in Figure 4.17b. As seen for low incidence angles, is the deceleration ability in form of the DeHaller number not noticeably influenced by water

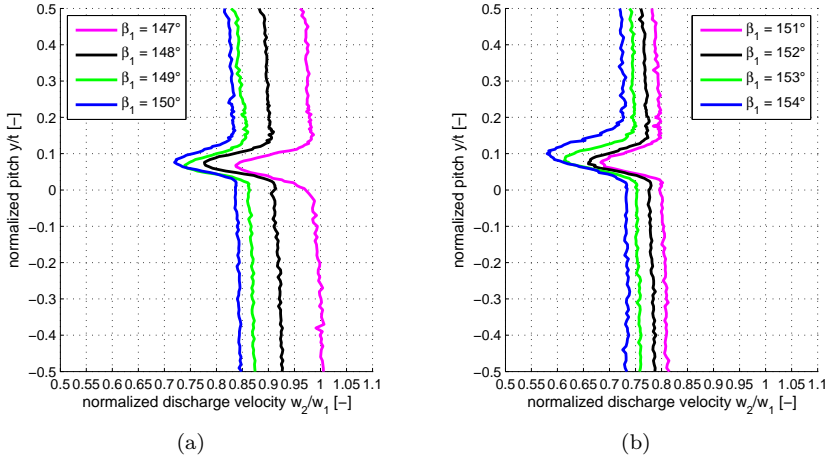


Figure 4.16: Case no. o080.0: measured normalized discharge velocity for low (a) and high (b) incidence angles

injection of 1.3%. The values remain on the level of the dry case. The differences are restricted to the wake. The velocity deficit is increased by about 5% for all incidence angles. The wake thickness is increased for higher incidence angles as well. But this effect cannot solely be reasoned with the presence of water droplets in the flow, as this could be noticed in case no. o080.0 as well. The change in shape of the velocity progression in the wake is similar to the structure seen in case no. o089.21 for high incidence angles. The wake extends towards the pressure side of the neighboring blade and a plateau shape becomes visible for $\beta_1 = 153^\circ$ and $\beta_1 = 154^\circ$. The reason for this has been given in the discussion of case no. o089.21 (water disintegrates from the film on the suction side of the blade).

The discharge velocity profiles for low incidence angles of case no. o080.21 are depicted in Figure 4.18a. In comparison to case no. o080.13 the differences in the area $0.2 < y/t < 0.5$ have to be mentioned. The discharge velocity tends to be lower in this area ultimately jeopardizing the periodicity of the flow. The recorded differences can be as high as 4% (abs.). This influence deteriorates with increasing incidence angles.

The DeHaller number was not influenced (when taking case no. o080.0 as a reference) by water injection of 1.3%. This changes for 2.1% water load. The ability to decelerate the flow decreases for all incidence angles. The

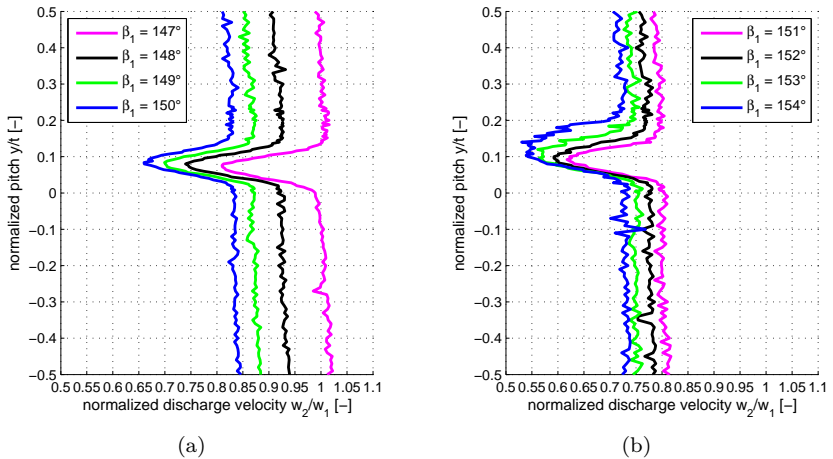


Figure 4.17: Case no. o080.13: measured normalized discharge velocity for low (a) and high (b) incidence angles

velocity deficit is not changed by the increase in water load.

Figure 4.18b depicts the discharge velocity profiles for case no. o080.21 at high incidence angles. The trend of a hampered deceleration by a water load of 2.1% remains intact for higher incidence angles. Normalized discharge velocities are 2...4% higher in comparison to case no. o080.13. A difference can be found in the position and size of the wake which tend to be displaced towards the suction side of the neighboring blade. Moreover is the size of the wake reduced in this case for high incidence angles. The series of experiments conducted with the outer cross section delivered results that differ from the results of the middle cross section tests. A summary is given in the following:

- A large deviation in the shape and position of the wake for the lowest incidence angles as seen in case no. m078.13 could not be identified. The reason for this may lie in the absence of a flow separation. This would emphasize the assumption that water injection dampens flow separations.
- A negative effect on the deceleration ability could only be identified for a water load of 2.1%. A lower water load of 1.3% did not influence the normalized discharge velocity.

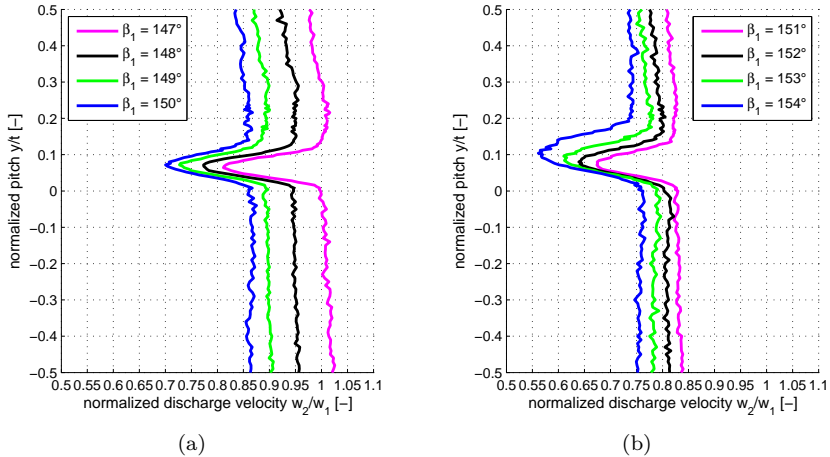


Figure 4.18: Case no. o080.21: measured normalized discharge velocity for low (a) and high (b) incidence angles

- The effect of water that reenters the flow upon disintegrating from the suction side of the blade was visible for all water laden flows. It is visible via a low velocity regime that is attached to the wake area oriented towards the pressure side of the neighboring blade. This type of structure has been visible in the tests of the middle cross section as well.

4.2.2 Deflection Angle

The discharge flow angle β_2 contains information on the ability of the cascade to divert the flow. In an attempt to analyze the effects of water injection on the cascade's aerodynamic behavior, the discussion of the discharge flow angle β_2 is key. In order to include the incident flow angle in the discussion, the deflection angle $\Delta\beta = \beta_1 - \beta_2$ will serve as a basis. The incident flow angle β_1 is the result of the cascade position, which is adjusted utilising the turning mechanism as described in chapter 2. The discharge flow angle β_2 is a direct output of the velocity measurements as the LDA/PDA records both components of the velocity vector. The deflection angle is presented as the difference $\beta_1 - \beta_2$ as presented in the cascade definitions.

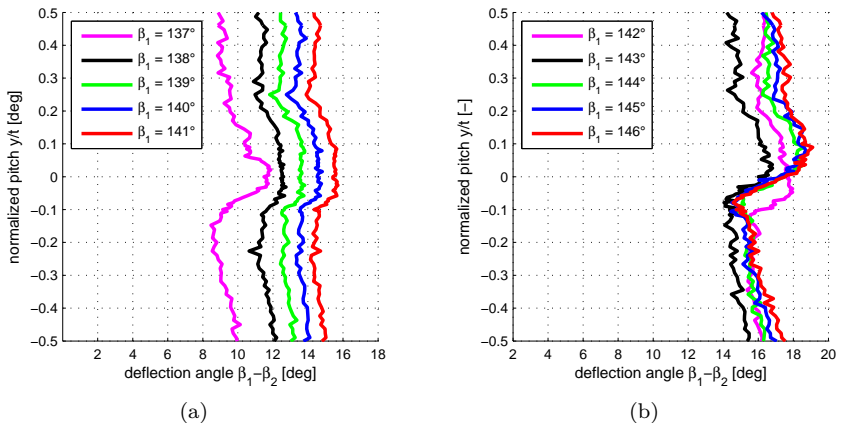


Figure 4.19: Case no. m078.0: measured deflection angle for low (a) and high (b) incidence angles

Airfoil Geometry 1: Middle Cross Section Figure 4.19a depicts the measured deflection angle for case no. m078.0 for low incidence angles. The result for $\beta_1 = 137^\circ$ shows a more volatile progression than it is seen for the other incidence angles. The difference between the highest and lowest value is 2.5° while it is 1° for all other incidence angles. The enlarged wake thickness discussed in Figure 4.7a can be identified here as well by the larger area of non uniform progression ($-0.15 < y/t < 0.2$). In comparison large gradients indicate a disturbed flow structure and support the assumption

of a flow separation on the pressure side of the blade as mentioned in the discussion of the discharge velocities. Incidence angles of $\beta_1 = 138^\circ \dots 141^\circ$ yield parallel progressions. The mentioned deviation in the wake area is not present.

The deflection angle progressions for case no. m078.0 at high incidence angles can be found in Figure 4.19b. The analysis of the discharge flow yielded by an incidence flow with $\beta_1 = 142^\circ$ reveals a beginning flow separation on the suction side as seen in Figure 4.7b. This finds expression in the dislocation of the wake towards the pressure side of the neighboring blade. These locally increased flow angles stem from low axial velocities in the respective areas. A fully developed flow separation can be found for $\beta_1 > 143^\circ$. Higher incidence angles still lead to higher velocities normal to the main flow direction and hence to higher deflection angles. The dislocation and extent of the wake increases with increasing incidence angles. Figure 4.20a depicts the deflection angle progressions for case no. m078.13

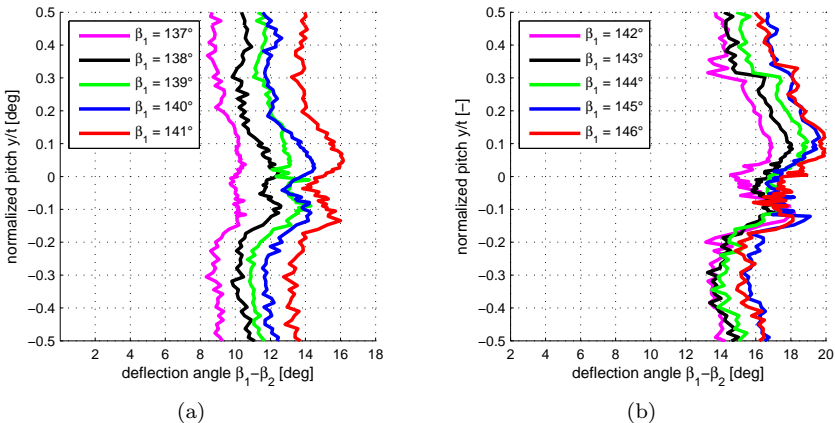


Figure 4.20: Case no. m078.13: measured deflection angle for low (a) and high (b) incidence angles

at low incidence angles. The comparison to the previous case shows that an incidence flow with $\beta_1 = 137^\circ$ results in an over all similar deflection angle but in a less volatile graph. The progression is well aligned with the progressions yielded for higher incidence angles. This finding is in accordance to the identified dampening effect of water injection on flow separations. Incidence flows with $\beta_1 > 137^\circ$ result in parallel progressions. The shape of

the wake differs from the dry case. The wake is enlarged and a local minimum at $y/t \approx -0.05$ becomes visible. This is due to a streak of water that originates from the trailing edge of the blade. This streak of high density spray dampens the local velocity normal to the main flow direction. This leads to lower local deflection angles. This effect increases with increasing incidence angles. The ability of the cascade to divert the flow is reduced by 10% or $\approx 1^\circ$.

The deflection angle progressions for case no. m078.13 for high incidence angles are depicted in Figure 4.20b. The comparison to the dry case reveals that the flow does not react as abrupt to increasing incidence angles as it does in the dry case. Incidence flows with $\beta_1 = 142^\circ \dots 146^\circ$ still show signs of flow separations (i.e. the local increase of deflection angles due to low axial velocities at $y/t = 0.1 \dots 0.2$), but the transition is not as abrupt. The deflection angles tend to be lower as seen for the low incidence angles.

The deflection angle progressions for case no. m078.21 at low incidence

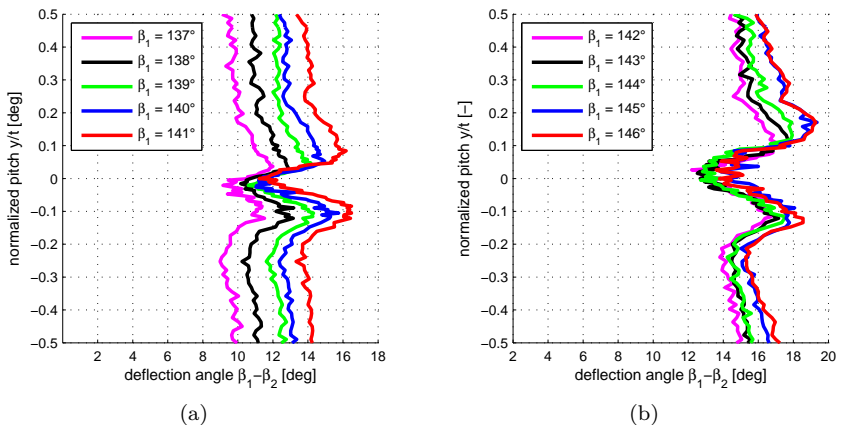


Figure 4.21: Case no. m078.21: measured deflection angle for low (a) and high (b) incidence angles

angles are shown in Figure 4.21a. The alterations seen in case no. m078.13 (in comparison to the dry case) can be identified again in amplified form, i.e. a local minimum of deflection in the area of the wake. The alignment effect for the incidence flow of $\beta_1 = 137^\circ$ can still be noticed via the parallelism of all progressions. A displacement of the wake can be noticed for $\beta_1 = 141^\circ$. This is in agreement with the discussion of the discharge velocities of this

case. The specific deflection angle is mildly decreased by the increase in water load.

Figure 4.21b depicts the deflection angle progressions for case no. m078.21 at high incidence angles. The identified structures for the low incidence angles can be found again. The local minimum in the wake area increases with increasing incidence angles. The shapes of the progressions remain parallel. The deflection angle progressions for case no. m071.0 are shown in Figure 4.22a. A difference to case no. m078.0 can be noticed for $\beta_1 = 137^\circ$. The

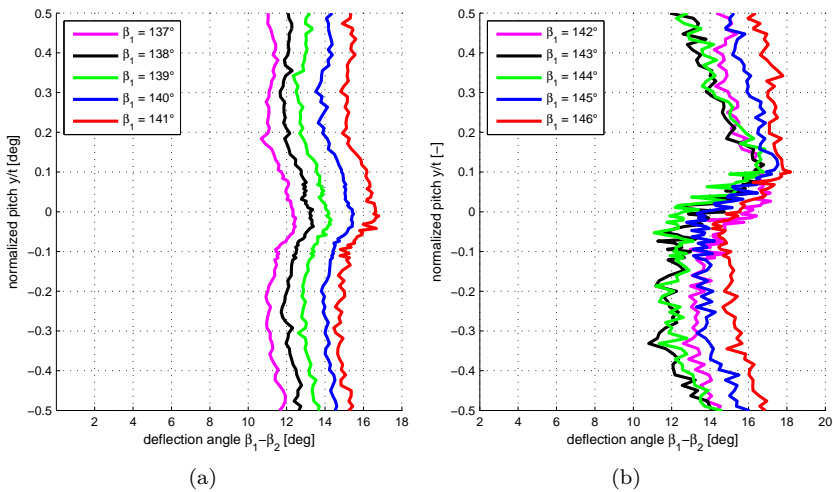


Figure 4.22: Case no. m071.0: measured deflection angle for low (a) and high (b) incidence angles

mean value for the deflection angle is increased by about 2° . Moreover is the high volatility reduced and the graph is parallel to the graph resulting from higher incidence angles. These differences can be explained by the lower inlet Ma number which renders the cascade more tolerant towards misaligned incidence flows. The incidence angle $\beta_1 = 138^\circ$ results in a higher deflection angle as well ($\approx +1^\circ$). This cannot be noted for $\beta_1 = 139^\circ \dots 141^\circ$. The well aligned progressions for the lowest incidence angles in this case are an additional indicator that the cascade was operating at or beyond the stability limit in case no. m078.0 as the range of stable incidence angles broadens with decreasing inlet Ma numbers.

Figure 4.22b shows the deflection angle progressions for case no. m071.0 at high incidence angles. The graphs show higher gradients than for the low incidence angles and the wake areas are dislocated and enlarged. This has been noted for case no. m078.0 as well and a flow separation on the suction side was identified as a possible reason. The effect of a wider range of incidence angles that result in a stable compressor flow, as seen for $\beta_1 = 137^\circ$, cannot be found for high incidence angles. The deflection angle progressions

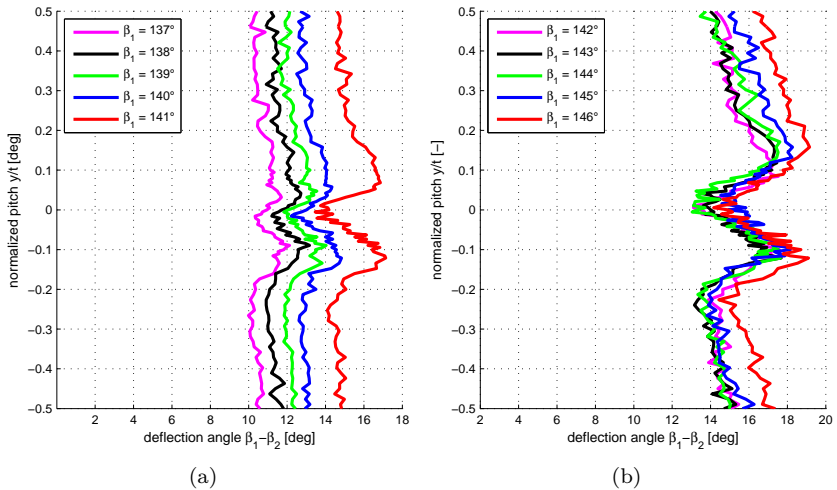


Figure 4.23: Case no. m071.13: measured deflection angle for low (a) and high (b) incidence angles

for case no. m071.13 at low incidence angles are shown in Figure 4.23a. A local minimum in the wake area as seen in case no. m078.13 can be found again in amplified form. The difference between minimum and maximum deflection angle is increased to 2.5° . The comparison to the corresponding dry case shows decreased deflection angles by $\approx 0.5^\circ$. The comparison to case no. m078.13 shows a higher level of deflection by $\approx 1.2^\circ$.

Figure 4.23b depicts the deflection angle for case no. m071.13 at high incidence angles. The results show similarities to the results gained from the experiments at low incidence angles. The amplitude increases with increasing incidence angles. This is again due to the amount of water that impinges on the blade which is dependent on the incidence angle. The comparison to

case no m078.13 shows a difference in the shape of the wake. While a local minimum at $y/t = 0$ can be identified for inlet Ma number $Ma = 0.71$, this is not the case for inlet Ma number $Ma = 0.78$. The lower inlet Ma number renders the cascade more sensitive to flow separations on the suction side. The evaluation of the discharge velocity revealed a dislocated wake towards the pressure side of the neighboring blade. This leads to relatively high axial velocities at $y/t = 0$ and consequently to low deflection angles.

The deflection angle progressions for case no. m071.21 at low incidence

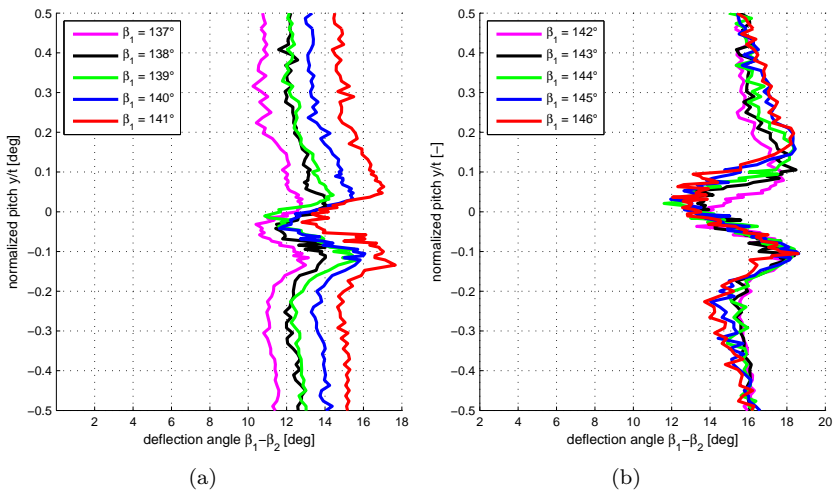


Figure 4.24: Case no. m071.21: measured deflection angle for low (a) and high (b) incidence angles

angles are depicted in Figure 4.24a. The increase in water load leads to an amplification of the effects identified in case no. m071.13. An increase in volatility and amplitude of the graphs can be noted as well as a local minimum in the wake area. The deflection angle remains at the same level. Figure 4.24b contains the deflection angle progressions of case no. m071.21 at high incidence angles. The specific deflection angle is decreased by the increase in water load. This finds expression in a smaller band of deflection angles. This was seen for inlet Ma number $Ma = 0.78$ as well but not to this extent. The reason for this amplification is a lower inlet Ma number that results in a higher tendency towards flow separation. An increasing

incidence angle increases the dissipation rate and the resulting deflection angle has a deficit in comparison to the dry case. An increased water load above a certain limit increases the dissipation.

The results of the discussion above can be summarized as follows.

- Water injection has a detrimental effect on the deflection angle. The values are decreased up to $\Delta_{\max} = 2^\circ$.
- A stabilization effect could be identified for low incidence angles at high inlet Ma numbers which is assumed to stem from dampened flow separation on the pressure side.
- A stabilizing effect for high incidence angles could not be identified.

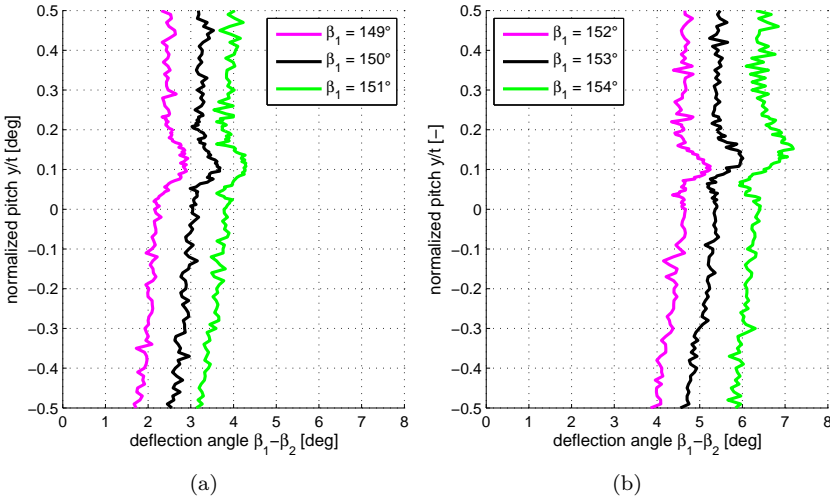


Figure 4.25: Case no. o089.0: measured deflection angle for low (a) and high (b) incidence angles

Airfoil Geometry 2: Outer Cross Section Figure 4.25a depicts the discharge flow angle for case no. o089.0 at low incidence angles. The graphs are dominated by a uniform progression. The lowest deflection angle is found for the lowest tested incidence angle. The specific deflection angle of the cascade $\Delta\beta/\Delta\beta_1 \approx 1$ remains constant for all incidence angles. A deviation from the uniform progression can be found in the area that corresponds to the wake in the discharge velocity profiles (i.e. Figure 4.13b). This deviation is present for all incidence angles and is characterized by a locally increased value. The higher values stem from low axial and radial velocities in the respective area.

The discharge flow angles for case no. o089.0 at high incidence angles can be found in Figure 4.25b. The structures that characterize the discharge flow angle for low incidence angles can again be found in amplified form for high incidence angles. A uniform progression apart from an area at $y/t \approx 0.1$ (which corresponds to the wake) is present. The highest incidence angle of $\beta_1 = 154^\circ$ results in a displacement of the non uniform structure to the pressure side of the neighboring blade as seen in Figure 4.13b for the wake. Figure 4.26a depicts the discharge flow angle profiles for case no. o089.13

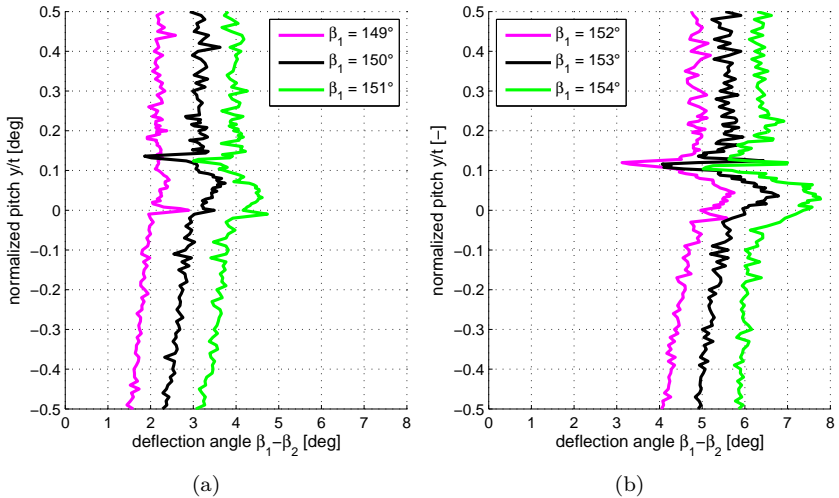


Figure 4.26: Case no. o089.13: measured deflection angle for low (a) and high (b) incidence angles

at low incidence angles. The comparison to the corresponding dry case (o089.0) shows that apart from the wake area no difference in the shape of the progression is caused by the presence of water droplets in the flow. A reduction of the deflection angle of $\approx 0.5^\circ$ can be found for $\beta_1 = 149^\circ$ and $\beta_1 = 150^\circ$. The area around $y/t \approx 0.1$ shows a smaller influence of the wake on the discharge flow angle. A structure that corresponds to the wake is only barely visible for $\beta_1 = 149^\circ$. The progression of the discharge flow angle in the wake area becomes more volatile. Beginning at $\beta_1 = 150^\circ$ high gradients become visible around $y/t = 0.12$. A reason for this may be a shear layer that is located between the streak of water that develops at the trailing edge of the blade (c.f. Figure 4.6) and the free flow. The velocities on each side of the shear layer show considerable differences and hence result in different flow angles.

Figure 4.26b shows the discharge flow angles for case no. o089.13 at high incidence angles. The previously described alterations fostered by water injection can be found again for high incidence angles in amplified form. The area of low axial velocities and hence higher angles of deflection becomes larger with higher angles of incidence and the deviation $\beta_{2,m} - \beta_{2,min}$ grows

to $\approx 2^\circ$. The degree of volatility in the discharge flow angle progression at $y/t = 0.12$ does not depend on the incidence angle. Figure 4.27a contains

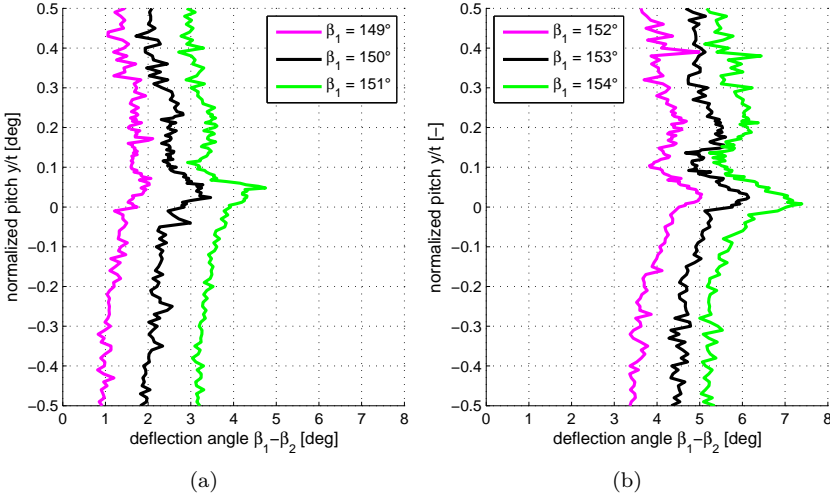


Figure 4.27: Case no. o089.21: measured deflection angle for low (a) and high (b) incidence angles

the discharge flow angles for case no. o089.21 at low incidence angles. The area of high volatility at $y/t = 0.12$ cannot be found for the water load of 2.1%. This might be due to the fact that more water reenters the flow at the trailing edge in this case and a higher amount of water causes a larger streak of high droplet density in the cascade discharge flow. The increased size of the streak causes a different mixing behavior and hence a different flow angle distribution. A final assessment of this flow structure cannot be given on the basis of the data at hand as an investigation of the entire two dimensional flow field with a sufficiently high resolution would be necessary to obtain a reliable result on this aspect. The necessary effort to obtain detailed data on this aspect however clearly exceeds the expected benefit and scope of this work.

The area of higher deflection angles at $y/t \approx 0.02$ shows higher gradients and a larger deviation from the mean value. The deflection angle progressions for case no. o089.21 at high incidence angles are depicted in Figure 4.27b. The deviations seen in the discussion of the low incidence angles can be

found again. The ability to divert the flow is reduced by about $0.5^\circ \dots 1^\circ$. The highest deflection angles can be found at $y/t = 0 \dots 0.1$ which differs from case no. o089.13. The streak of high density spray has a larger influence in this case and fosters a corresponding region of low axial velocities (cf. Figure 4.15b) which in turn leads to higher deflection angles as the meridional velocity is not affected by the streak at this location of the flow field.

Figure 4.28a depicts the deflection angle for case no. o080.0 at low incidence

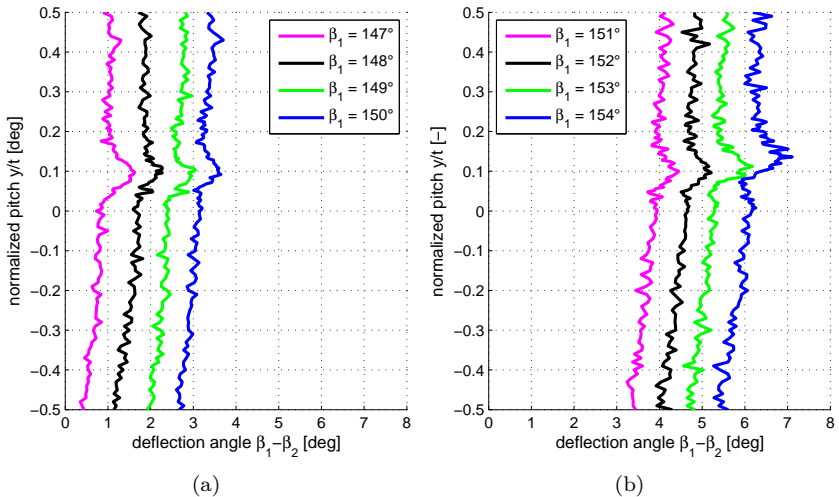


Figure 4.28: Case no. o080.0: measured deflection angle for low (a) and high (b) incidence angles

angles. The graphs for $\beta_1 = 148^\circ \dots 150^\circ$ show a parallel shape as seen for case no. o089.0. The wake can be identified by higher deflection angles due to low axial velocities. The position of the locally higher deflection angles correspond to the identified positions of the wake in the analysis of the discharge velocities. An exception can be found for $\beta_1 = 147^\circ$. The discharge flow angle deviates towards the suction side of the neighboring blade towards higher deflection angles. This is an additional indicator to the assumption that the cascade was operating at the stability limit as seen in the DeHaller number close to 1 for this operating point in Figure 4.28a. The deflection angle progressions for case no. o080.0 at high incidence angles can be found in Figure 4.28b. The trend of higher deflection angles

for higher incidence angles stays intact as well as the position and the extent of the wake. A larger structure of higher deflection angles can be found for $\beta_1 = 154^\circ$. This is in agreement with the increased wake thickness seen in Figure 4.16b. The deflection angle progressions for case no. o080.13 at low

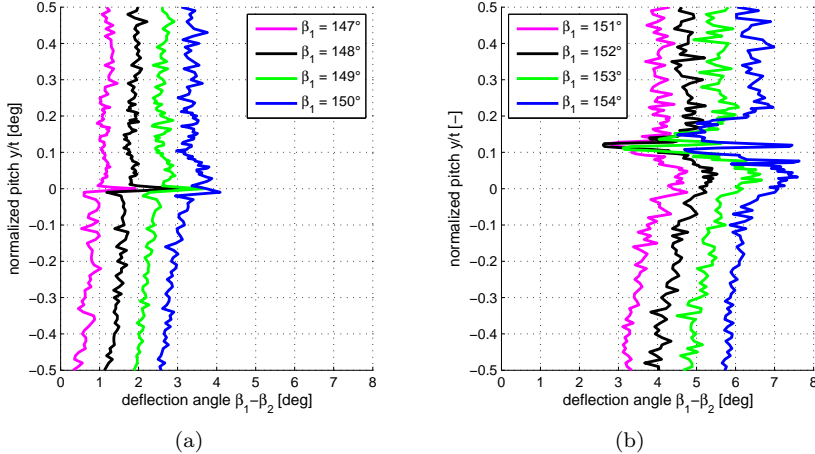


Figure 4.29: Case no. o080.13: measured deflection angle for low (a) and high (b) incidence angles

incidence angles are depicted in Figure 4.29a. The graph shown for $\beta_1 = 147^\circ$ stands in clear contrast to case no. o080.0. The difference in shape and position seen in the dry case cannot be noticed with water injection. The progression is parallel to the results of the remaining incidence angles. This implies that the flow structure that led to the disturbed deflection angle progression in case o080.0 has disappeared. The nature of this flow structure cannot be determined on the basis of the presented data, because a sign of flow separation could not be identified in the discussion of the discharge velocities. The value of the deflection angle is negative for $\beta_1 = 147^\circ$ which again indicates that the compressor was operating at or beyond the stability limit. Incidence flow of $\beta_1 = 148^\circ \dots 150^\circ$ yields similar flow patterns as seen in case no. o089.13. The areas of higher volatility can be found again in a similar extent for the same incidence angles. A sensitivity of the formation of the determining flow structures seem to be insensitive to the inlet Ma number in the tested range. The use of water injection amplifies the highest measured deflection angle slightly which is due to lower

minimal axial velocities that are measured for the droplet laden flow. Figure

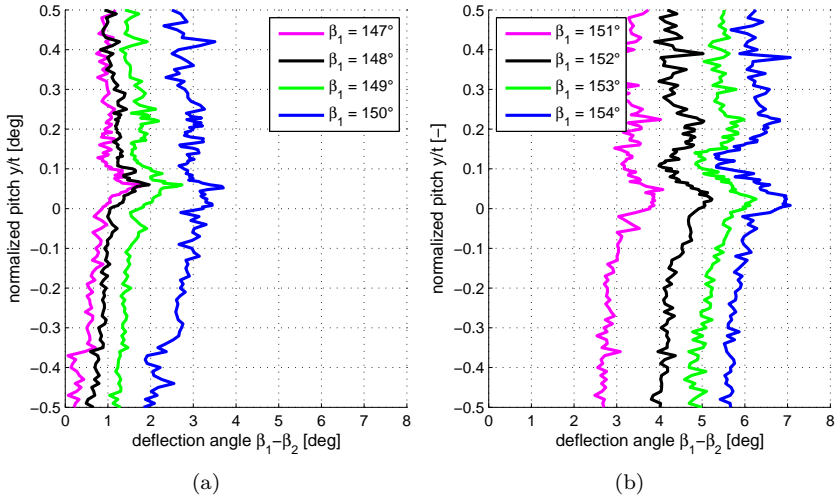


Figure 4.30: Case no. o080.21: measured deflection angle for low (a) and high (b) incidence angles

4.30a depicts the deflection angle progression yielded in case no. o080.21 for low incidence angles. Incidence angles $\beta_1 = 148^\circ \dots 150^\circ$ produce a similar progression as seen in case no. o080.13. The values for the discharge angle tends to be slightly lower for higher water load.

The discharge flow angle progressions for case no. o080.21 at high incidence angles can be found in Figure 4.30b. The area of high volatile readings as seen in case no. o080.13 at $y/t \approx 0.1$ cannot be noticed anymore. The streak of disintegrating water at the trailing edge dominates the discharge flow as discussed in the cases with inlet Ma number $Ma = 0.89$. The cascade's ability to divert the flow is lowered up to 5% relative. The wake can be identified in areas that are in agreement to the findings in the discussion of the discharge flow velocities for all incidence angles.

The analysis of the deflection angle is a supplemental source of information to the data gained from the discussion on the discharge flow velocities. A summary of the information gained from the tests conducted with Airfoil Geometry 2 (outer cross section) is given here:

- The extent of flow alterations by water injection is determined by the water mass fraction. Water load of $X = 1.3\%$ leads to a shear layer in the discharge flow resulting in a highly volatile progression of the deflection angle. It also leads to an alignment effect for the lowest tested incidence angle. The overall ability of the cascade to divert the flow is not affected.
- Water mass fraction of $X = 2.1\%$ leads to a wide streak of high density spray that originates from the trailing edge. Turbulence that is produced due to the relative velocity of water and air flow leads to a higher diffusion rate and renders the highly volatile area seen with the low water mass fraction invisible. The overall ability of the cascade to divert the flow is lowered by $\approx 5\%$ relative to the dry air flow.

4.3 Investigation of Performance Parameters

In the previous section the discharge flow properties were discussed in detail in order to reveal the influences of a water laden flow on the aerodynamic behavior of the tested compressor cascades. The application of these results in the assessment of the aerodynamic performance however demands the evaluation of dimensionless numbers. The knowledge of these is mandatory for comparability and the calculation of multistage compressors. The most important dimensionless numbers in this context are:

- Axial Velocity Density Ratio $AVDR$
- DeHaller number $Ha = w_2/w_1$
- deflection angle $\Delta\beta = \beta_1 - \beta_2$
- loss coefficient ω

A cross sensitivity of AVDR, loss coefficient and discharge flow angle exists, as discussed in [88]. Based on this, an evaluation of the loss coefficient and the discharge flow angle has to incorporate a discussion of the AVDR. A higher value for AVDR leads to a negative bias for the loss coefficient and the discharge flow angle as was stated by Köller in [43].

Misaligned incidence flows can result in corner vortices and/or flow separations. Both phenomena lead to a stream tube contraction and consequently to a higher value for the AVDR. This is fostered by a larger deviation from the design incidence angle.

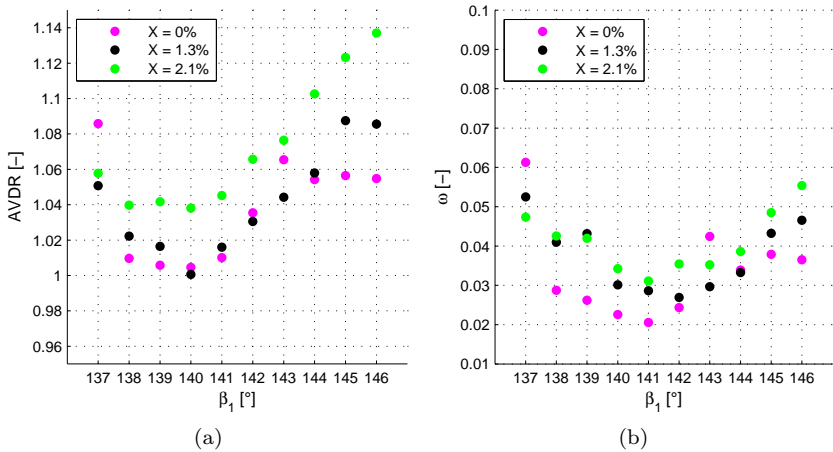


Figure 4.31: Influence of water injection on AVDR and loss coefficient. Middle cross section at inlet $Ma=0.78$

The following discussions are based on the data gained from the measurements of the inlet and discharge flow. Both geometries, the middle and the outer cross section will be discussed.

Airfoil Geometry 1: Middle Cross Section The AVDR as a function of the incidence angle of the cases m078.0, m078.13 and m078.21 is depicted in Figure 4.31a. The readings for the dry case show an overall low level in comparison to the wet cases. Starting from the lowest tested incidence angle, the progression shows a negative tendency and reaches its global minimum ($AVDR_{\min} \approx 1.005$) for $\beta_1 = 140^\circ$. The values increase with increasing incidence angles and reach a stagnating maximum ($AVDR_{\max} \approx 1.06$) for $\beta_1 \geq 143^\circ$. An exception to the low values for AVDR in the dry case can be found for the lowest incidence angle of $\beta_1 = 137^\circ$. From the discussion of the discharge flow properties of case m078.0 we know that a flow separation is a most likely scenario for this case. A consequence of this is $AVDR > 1.08$ in the dry case which is considerably higher than in the wet cases. Water injection leads to a reduced AVDR for both water laden cases for $\beta_1 = 137^\circ$. As discussed above, a lower value indicates a lower contraction of the stream tube in the discharge plane. This emphasizes the

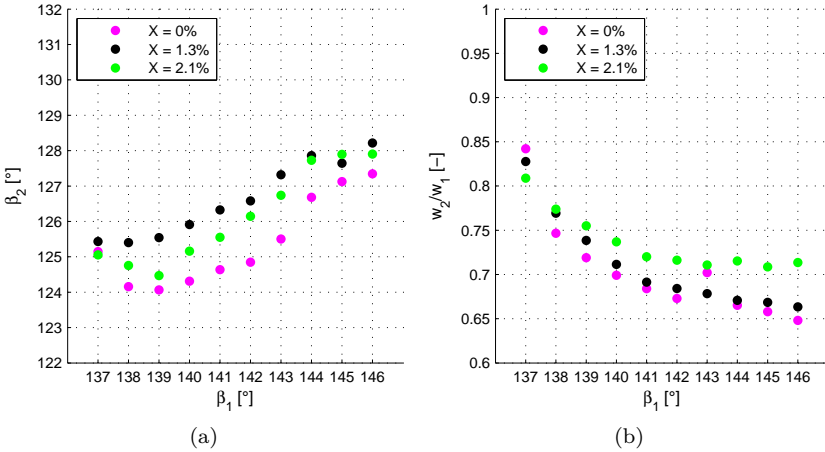


Figure 4.32: Influence of water injection on discharge flow angle and De-Haller number. Middle cross section at inlet $Ma=0.78$

dampening effect of the presence of water droplets on vortex generation and flow separations as these (in addition to the wall boundary layer) lead to the stream tube contraction.

The progression of the loss coefficient is depicted in Figure 4.31b. It follows the typical shape with a global minimum of $\omega_{\min} = 0.02$ for $\beta_1 = 141^\circ$. A reduced value for ω is found for both water laden cases in comparison to the dry case for $\beta_1 = 137^\circ$. The AVDR is also lower in this case. A lower AVDR indicates an increased flow deceleration, due to a low stream tube contraction, that leads to higher stresses on the boundary layer on the suction side of the blade resulting in higher losses. Considering this, the positive effect on the loss coefficient can be accredited to the presence of water droplets in the flow.

Negative effects of water injection in terms of an increased loss coefficient for $\beta_1 > 137^\circ$ can also be accredited to the presence of water droplets in the flow. Wherever the loss coefficient is increased, the AVDR is either unchanged or higher which, based on the discussion above, in tendency leads to a higher loss coefficient. A different picture is drawn from the evaluation of the discharge flow angle. The influence of the AVDR is clearly visible. A high value of the AVDR for the dry case at $\beta_1 = 137^\circ$ results in a lower

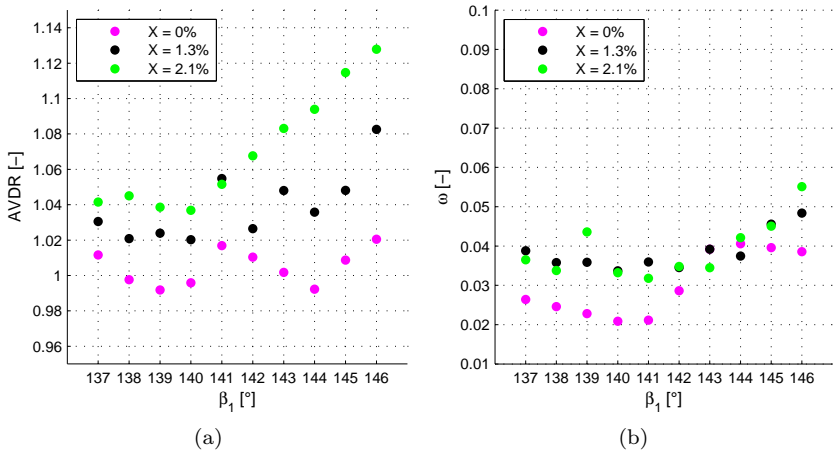


Figure 4.33: Influence of water injection on AVDR, loss coefficient. Middle cross section at inlet $Ma=0.7$

value for β_2 . High values for the AVDR lead to underestimated values for β_2 in the case of water load of $X = 2.1\%$. Therefore it can be generally stated for the evaluation of the middle cross section at inlet Ma number $Ma = 0.78$ that the differences seen between the dry reference case and the wet cases can be accredited to the presence of water droplets in the flow. The analysis of the cross sensitivity of the AVDR and the discharge flow angle as well as the loss coefficient clearly shows that the alterations, even though positively influenced by the AVDR, still lead to over all negative effects.

The effects of water injection on the flow deceleration are depicted in Figure 4.32b. Flow deceleration is generally hampered by water injection. The values increase with increasing water load by up to 5%. An exception can be found for the lowest incidence angle $\beta_1 = 137^\circ$. The values for the DeHaller number are decreased for the water laden flows. The AVDR for the water laden flows at this incidence angle show lower values than the dry reference flow. This suggests an underestimation of the DeHaller number and the effect of the decreased value cannot be clearly accredited to the presence of water droplets in the flow.

The evaluation of the AVDR, the loss coefficient, discharge flow angle and the DeHaller number in the case of inlet Ma number $Ma = 0.71$ can be

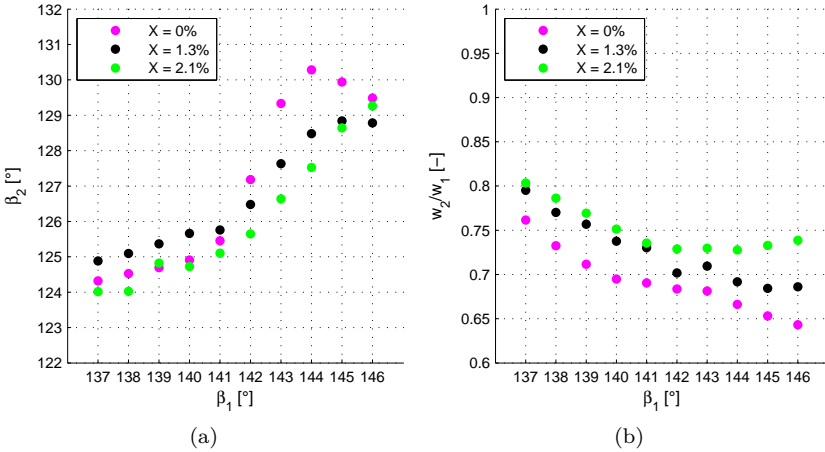


Figure 4.34: Influence of water injection on discharge flow angle and De-Haller number. Middle cross section at inlet $Ma=0.71$

found in Figure 4.33a to 4.34b. In contrast to the previous discussion of the flow resulting from an inlet Mach number $Ma = 0.78$, the AVDR is generally increased in case of water injection in the range of 2...10 percent points. A smaller increase of up to 4 percent points can be found for incidence angles which result in a stable, non detached discharge flow ($\beta_1 = 137^\circ \dots 142^\circ$). Beginning flow separations were identified for $\beta_1 \geq 142^\circ$. These flow separations are accompanied by higher increases of the AVDR as the stream tube contraction in the discharge plane is increased. Higher incidence angles result in an amplification of this tendency. A higher water mass fraction leads in tendency to a higher AVDR.

The loss coefficient ω is increased as well. The data in Figure 4.33b show an increase of up to 2 percent points while still showing the typical shape progression for the loss coefficient with a global minimum of $\omega_{\min} = 0.02$. This increase is however underestimated, considering the cross sensitivity of AVDR and ω . The loss coefficient shows higher values even though the AVDR is increased substantially which results in an underestimation of the loss coefficient. This also renders the improved values for ω negligible, which were found for $\beta_1 = 143^\circ$ and $\beta_1 = 144^\circ$ where the loss coefficient shows lower values.

The discharge flow angle is increased as a consequence of water injection of $X = 1.3\%$ for the range of $\beta_1 = 137^\circ \dots 145^\circ$. This result can be accredited to the presence of water droplets in the flow as the cross sensitivity of the AVDR causes a negative bias for the discharge flow angle in this case. The discharge flow angle is therefore underestimated. This results in a decreased flow turning. The influence of the AVDR can be observed for the highest incidence angles where the values for β_2 tend to fall below the value of the dry reference flow. This phenomenon can be directly linked to the behavior of the AVDR in this band of incidence angles. The discharge flow angle β_2 shows consequently lower values than the dry reference flow in the case of $X = 2.1\%$ water injection.

The DeHaller number for this case is depicted in Figure 4.34b. A progression of decreasing values can be found for the dry case as well as the water laden cases. Water injection results in higher values for the DeHaller number which has been found in the case of inlet Ma number $Ma = 0.78$ as well. A diverging progression towards higher incidence angles can be found in correspondence to the AVDR progression. The following can be stated in summary of the evaluation of the performance parameters of the middle cross section:

- Water injection leads in almost all cases to an increased loss.
- Water injection tends to hinder flow turning. The discharge flow angle is increased by about $0.1\Delta\beta_{\text{design}}$.
- Water injection tends to hinder flow deceleration by 10...15% relative.
- Water injection tends to increase the AVDR.
- A scenario could be identified ($Ma=0.78$, $\beta_1 = 137^\circ$) where a flow separation on the pressure side, due to a negative incidence angle, caused high losses in the dry case. This scenario benefited from the use of water injection in terms of recorded losses.

Airfoil Geometry 2: Outer Cross Section The influence of the AVDR on the loss coefficient, discharge flow angle and the DeHaller number in the case of inlet Ma number $Ma = 0.89$ can be found in Figure 4.35a to 4.36b. The values for the AVDR in the dry reference case follow a U-shaped progression with a global minimum for $\beta_1 = 152^\circ$. The global maximum can be found for $\beta_1 = 149^\circ$. Water injection leads in tendency to a lower AVDR in this case. The maximum decrease is 3%.

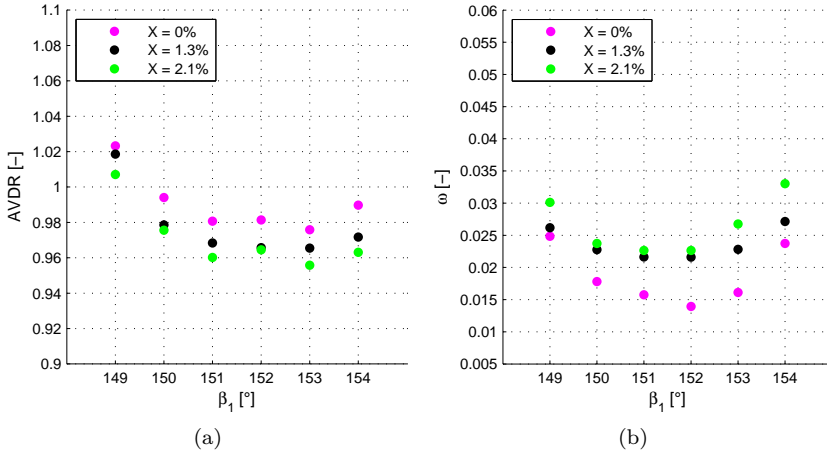


Figure 4.35: Influence of water injection on AVDR, loss coefficient. Outer cross section at inlet $Ma=0.89$

The loss coefficient ω (Figure 4.35b) follows the same typical shape as seen for the test cases with the middle cross section. The global minimum ($\omega_{\min} = 0.014$) can be found for $\beta_1 = 152^\circ$. The progression found for water injection of $X = 1.3\%$ shows a less volatile behavior. This reflects the findings from the detailed discussions of the discharge flow properties, where it was found that the water laden flow is less sensitive to alterations of the incidence angle. For the lowest tested incidence angle the value is increased by less than 1% point. Considering the overestimation due to the cross sensitivity of the AVDR, this increase neglectable. For all other incidence angles a considerably higher increase of the loss coefficient is found. It can also be noted that the progression for $X = 2.1\%$ water load is almost parallel to the dry reference case.

The discharge flow angle is slightly increased for water load of $X = 1.3\%$. This effect cannot be clearly accredited to the presence of water droplets in the flow, as the AVDR leads, in tendency, to an overestimation of the discharge flow angle in this case. The values for the higher water load do not differ significantly from the dry test case. This results in an amplification of the deflection angle, considering the influence of the AVDR.

The DeHaller number remains unchanged by water injection for the most

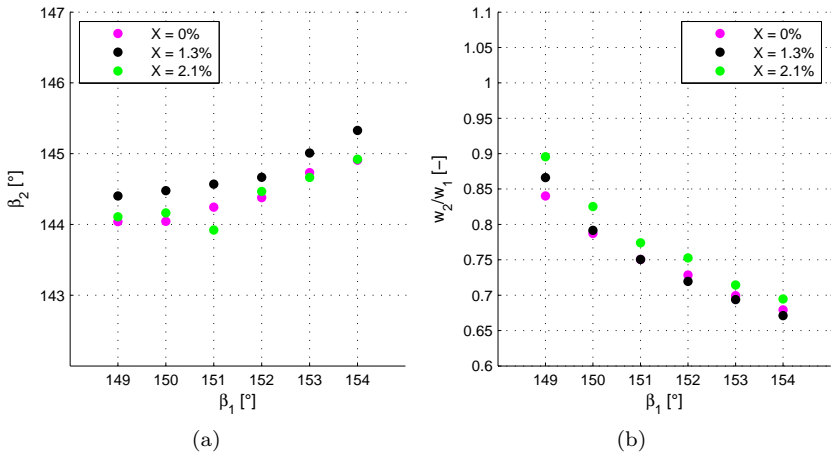


Figure 4.36: Influence of water injection on discharge flow angle and DeHaller number. Outer cross section at inlet $Ma=0.89$

incidence angles. An increase of up to 3% points can be found for $\beta_1 = 149^\circ$ and $X = 1.3\%$. Higher water load leads to higher DeHaller numbers.

The AVDR, the loss coefficient, discharge flow angle and the DeHaller number in the case of inlet Ma number $Ma = 0.8$ are depicted in Figure 4.37a to 4.38b. The progression for the AVDR seen in the previous case can be found again. A value of $AVDR \approx 1.03$ has been recorded for the lowest incidence angle tested ($\beta_1 = 147^\circ$). For higher incidence angles a monotonic progression unfolds which converges to a band of $AVDR = 0.94 \dots 0.96$. The influence of water load increases for incidence angles $\beta_1 = 150^\circ \dots 154^\circ$ resulting in differences in the AVDR of 2% points.

The progression for the loss coefficient follows the typical U-shape. A global minimum of $\omega = 0.015$ can be found for $\beta_1 = 152^\circ$ which is unchanged from the previous case (inlet Ma number $Ma = 0.89$). Water injection increases the loss coefficient up to 1% point of 50% relative for $\beta_1 = 152^\circ$. The consideration of the cross sensitivity of the AVDR and the loss coefficient does not have a considerable influence in this case as the values for the AVDR diverge in both directions (for the water laden cases) from the dry reference case and the loss coefficient is uniformly increased.

A shift of the minimal value for the loss coefficient of $\Delta\beta_1 \approx 1^\circ$ towards

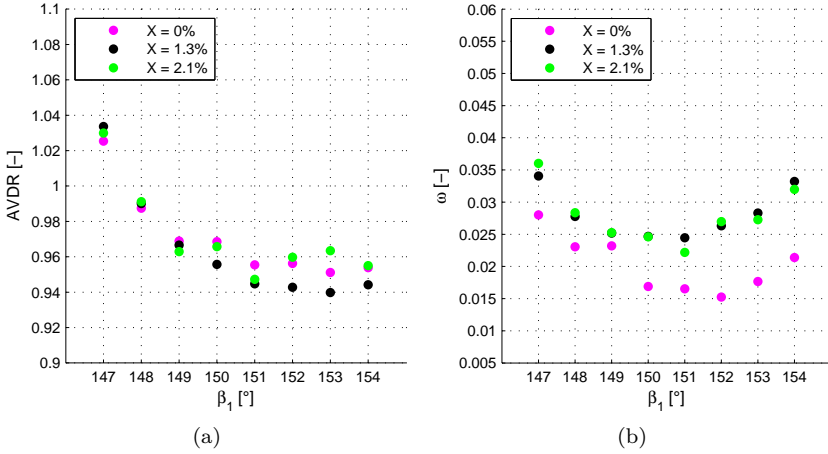


Figure 4.37: Influence of water injection on AVDR, Loss coefficient. Outer cross section at inlet $Ma=0.8$

low incidence angles can be noticed. The results of the evaluation of the discharge flow angle can be found in Figure 4.38a. The dry reference flow results in a monotonic increase of the values with increasing incidence angles as seen in the previous case. The values for the water laden flows diverge from the reference for incidence angles $\beta_1 \geq 150^\circ$, but this is due to the AVDR. A higher AVDR leads to a lower β_2 and vice versa. This can be seen in this case.

The DeHaller number, as depicted in Figure 4.38b, follows a similarly shaped progression as in the previous case. Water injection of $X = 1.3\%$ has no significant influence on the DeHaller number. A higher water load tends to hamper the deceleration which results in higher values for the DeHaller number of up to 6% points.

The evaluation of the dimensionless numbers for the outer cross section showed significant differences in comparison to the middle cross section. A summary is given here:

- Water injection has a more limited effect on the AVDR in comparison to the middle cross section.
- Water injection increases the losses similarly to the middle cross sec-

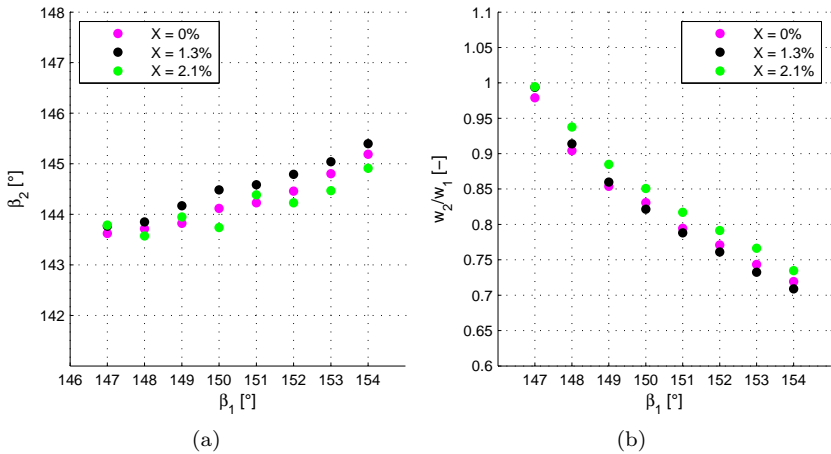


Figure 4.38: Influence of water injection on discharge flow angle and De-Haller number. Outer cross section at inlet $Ma=0.8$

tion (up to 50%), relative.

- Water injection hinders flow turning by about $0.1\Delta\beta_{\text{design}}$. This finding is repetitive to the findings for the middle cross section.
- Water injection hampers flow deceleration by 5...7% relative.
- A scenario could be identified, where the negative effect of water injection on the losses is kept to a minimum for $\beta_1 = 147^\circ$ and inlet Ma number $Ma = 0.8$. This is in correspondence to the findings for the middle cross section where the best results in terms of losses could be found for the lowest incidence angles.

These differences may be determined by the presence of water on the suction side of the blade. A certain fraction of water droplets in the incident flow will impact on the blade and form a water film, as discussed in Chapter 4.1. The water film will desintegrate into rivulets upon reaching the MLFT due to the acceleration of the surrounding flow and the resulting shear stress. Rivulets have a greater height in comparison to a water film. The increased height leads to increased aerodynamic forces on the water which lead to desintegrating ligaments on the suction side. The position of the

water film breakup into rivulets depends foremost on the water load, the incidence angle and the inlet Ma number as these parameters determine the Ma number distribution on the suction side. The water that reenters the flow at the suction side is subject to high relative velocities as the ligament originates from the boundary layer. This leads to an impulse transport from the continuous to the dispersed phase and consequently to an increased wake thickness.

This influence extends to the discussion of the deflection angle. The blade geometry of the middle cross section is designed to divert the flow by 14° versus 6° for the outer cross section at design incidence angle. The relative velocity normal to the main flow direction between the continuous phase and the desintegrated ligaments is higher for the middle cross section as the initial velocity of the ligaments is identical for both geometries thus leading to higher impulse transfer rates ultimately leading to a more significant influence of water injection in terms of the deflection angle on the middle cross section.

These findings have to be discussed in the light of the application of water injection in rotating machinery.

4.4 Investigation of the Inter Blade Flow

The results discussed above imply a significant influence of water injection on the flow. In order to clarify the underlying phenomena additional measurements have been conducted. The results can be found in the inter blade Ma number distribution in Fig. 4.39. The measurements were conducted at an incidence angle of $\beta_1 = 140^\circ$ and $Ma = 0.78$ on the middle cross section. The measurement grid comprises 2000 nodes and 10000 droplets were recorded for each node in the case of water injection. A number of 5000 particles were recorded in the case of the dry air flow. The results of the dry air flow are depicted in the top figure and serve as the reference flow. The measurement of the Ma number distribution of the dry air flow was conducted with DEHS as a seeding, as in the experiments regarding the performance parameters. The measurement of the Ma number distribution in case of a water laden flow delivers the values for all droplets classes during the same experiment. A post processing routine is applied to filter the information for different droplet sizes. The Ma number distributions in case of water injection are displayed in a point to point normalization in the form of Ma/Ma_{ref} for each droplet class. Each data point of the dry air flow (DEHS) serves as a reference for the corresponding coordinate of the water

laden flow for each droplet class. The different droplet classes are chosen to represent different abilities to follow the air flow. The smallest droplet class of $0 \mu\text{m} < d_d < 2 \mu\text{m}$ represents the air flow. Droplets of this size will follow the air flow with negligible deviation, as discussed. This is also well visible in the contour plot of the smallest droplet class. The measured deviation from the dry air flow in the undisturbed incidence flow is $< 3\%$.

The data shows a compressor flow with a high velocity regime on the suction side which is terminated by the deceleration as the free flow area increases. The highest recorded velocities are close to $Ma = 1$. The wake originates at the trailing edge and is characterized by low velocities. This behavior can be generally found for the droplet laden flow, which is depicted for the different droplet classes in the remaining subfigures of Figure 4.39, as well. The contour plot of the normalized velocity for the smallest droplets ($0\mu\text{m} < d_d < 2 \mu\text{m}$) shows two major differences in comparison to the dry air flow (DEHS). Firstly, the maximum velocity in the high speed regime shows a deficit of about 15% for the lowest values. This influences the incidence flow of the neighboring blade. Secondly, the discharge velocity is about 10% higher. Other differences can be noticed. The incidence velocity is about 2% lower just upstream of the leading edge ($x/c \approx 0.1$). The incidence velocity is influenced by the high speed regime on the suction side of the neighboring blade. As the maximum velocity on the suction side is reduced, the incidence velocity is reduced. It has to be pointed out however, that the velocity deficit in incidence velocity is only a small fraction of the deficit in the high speed regime (2% vs. 15%).

A velocity surplus can be noticed directly at the leading edge. This is due to the droplet inertia. The continuous phase is decelerated abruptly upon approaching the stagnation point at the leading edge of the blade while the droplets remain travelling at higher velocities. The wake, characterised by low velocities, tends to cover a larger area and originates not solely from the trailing edge. The source of this low velocity regime is water that disintegrates from the suction side of the blade. The normalised discharge velocities depicted in Figure 4.8a show the same values for the minimal velocity in the wake. This seems to stand in contrast to Figure 4.39. The reason for this is, that the discharge traverse was recorded further downstream where the flow properties are more aligned. The differences mentioned above can be found in amplified form for larger droplets. Increasing droplet size elevates the velocity deficit in the high speed regime and the velocity surplus in the cascade discharge properties.

The Ma number distribution for the flow around the outer cross section for

an inlet Ma number $Ma = 0.89$ is depicted in Figure 4.40. The incidence flow results in a well developed transonic flow regime on the suction side. The maximum Ma number is $Ma_{\max} > 1.1$. The high velocity regime is terminated by a shock that causes an abrupt flow deceleration at $x/c \approx -0.3$. The flow is further decelerated downstream. The wake originates at the trailing edge and the suction side close to the trailing edge. A high incidence angle in this measurement leads to high pressure gradients that cause an increased boundary layer thickness. This causes the dominant wake structure.

The comparison with the droplet laden flow shows no influence of the water injection on the incidence flow. The normalised Ma number upstream of the leading edge of the blade approaches unity for this entire area. A velocity deficit of up to 15% is visible in the high velocity regime on the suction side. The discharge velocity does not show a clear deviation from the dry case. As on the pressure side of the blade, the deviations are comparably small at $> 4\%$.

The identified alterations can be found in amplified form for the larger droplet classes. A larger droplet size leads to larger deviations. The velocity deficit in the high velocity regime is increased in size and intensity. A velocity surplus of up to 20% is recorded for the largest droplets in the cascade discharge flow on the suction and pressure side.

The altered flow properties with regard to the velocity in case of water injection have multiple symptoms. The largest deviations between the dry and droplet laden flow can be found in areas of large velocity gradients. The droplet laden flow tends to dampen velocity gradients. This can be explained by the coupling of the two phases. The density of water ρ_w exceeds the density of air ρ_{air} by three magnitudes. Comparing a unit volume of air and water, this results in a higher inertia for the unit volume water. Considering comparable pressure gradients in the flow field for both cases (water laden and dry) this has to lead to a lower acceleration and deceleration for water droplets of a sufficient size as the same pressure induced forces act on a greater mass. This in turn leads to relative velocities between droplets and surrounding air flow. This argumentation is supported by the trend of larger deviations in the velocity readings for larger droplets. However it has to be stressed, that all droplet sizes are present at the same time. The measurements show, that considerable velocity difference develop between the droplet classes. Therefore, droplet-droplet interaction cannot be neglected. The collision of droplets leads to an impulse transport between the droplet classes. Assuming a homogeneous velocity distribution over all

droplet classes in the incidence flow, only a comparably small, turbulence driven number of collisions will take place. This number will increase with increasing relative velocity between the droplet classes. For the incidence flow the furthest upstream scenario of this sort is the high velocity regime on the suction side. The acceleration of the small droplets causes collisions with the larger and slower droplets. Impulse is transported to the larger droplet classes. This explains the velocity deficit for the smallest droplet class.

In summary the following can be stated:

- Water injection reduces maximum velocity in the high velocity regime on the suction side of the blade.
- Water injection increases the rate of deceleration towards the cascade discharge plane.
- The above mentioned effects become more prevalent for larger droplets.
- The effects are also increased with higher design deflection angles of the blade. A reason for this can be given with the increased droplet-droplet collision probability. Larger force is needed to accelerate larger droplets at the same rate in any direction. Large droplets will therefore not only be less easily decelerated but also deflected. A relative velocity develops therefore in two directions.

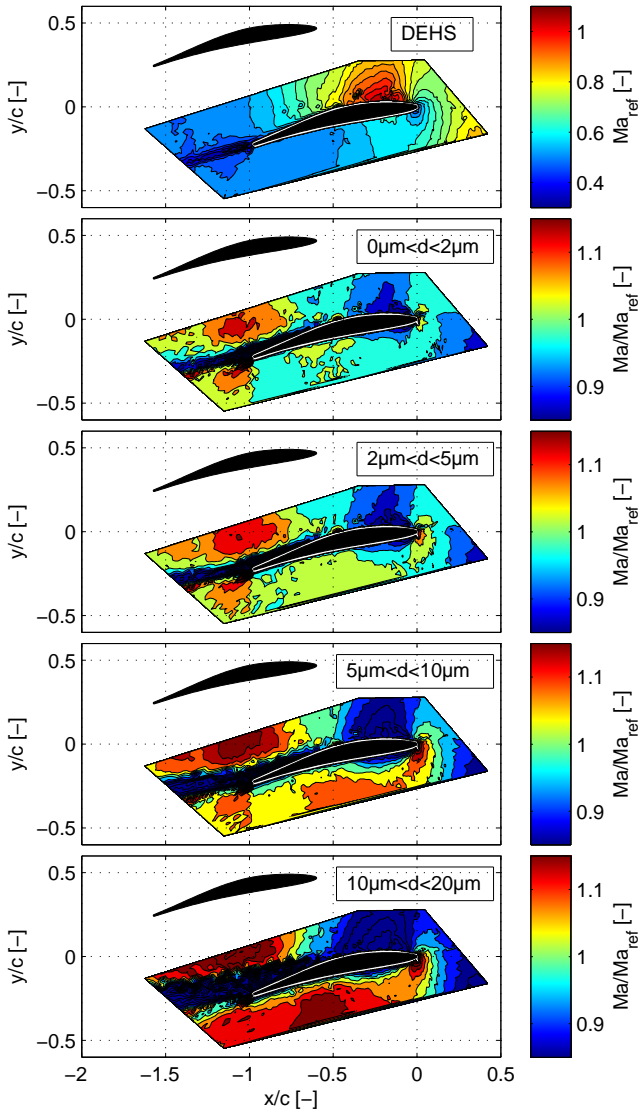


Figure 4.39: Measured blade passage Ma number for middle cross section ($\beta_1 = 140^\circ$, $X = 1.3$)

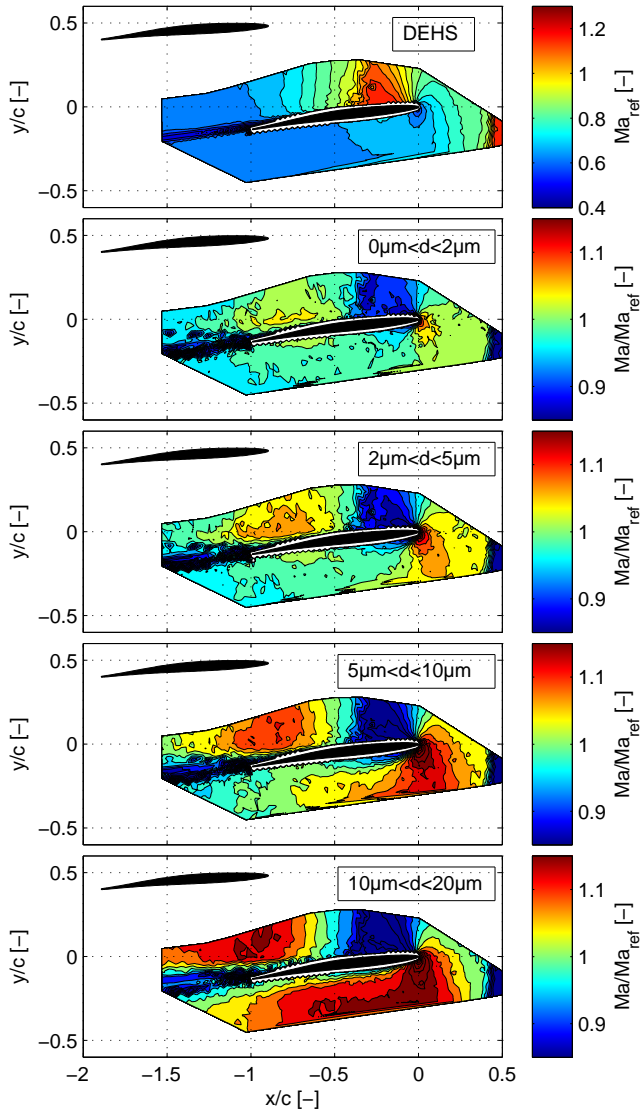


Figure 4.40: Measured blade passage Ma number for outer cross section ($\beta_1 = 154^\circ$, $X = 1.3$)

5 Conclusion

A large fraction of investigations published on two phase compressor flows incorporate theoretical work on the compression process. Thermodynamic analysis focus on droplet evaporation models and how the resulting fluid properties influence the compression process. Key aspects in this kind of research are the shift in stage loading towards the later stages and the reduction in surge margin.

Recent publications deal with the aerodynamic effects caused by the presence of liquid water droplets numerically. Full three dimensional CFD models of entire axial compressors are presented.

Past experimental investigations however show, that these models are not yet able to predict all identified aspects of the two phase flow. In order to increase the knowledge on the aerodynamic performance of a compressor cascade in a two phase flow, a series of measurements in a linear compressor cascade was conducted at the wind tunnel test facility at the Helmut-Schmidt-University in Hamburg, Germany.

5.1 Summary

This study aimed at the deeper understanding of the effects imposed by water injection on the aerodynamic performance of two compressor blade profiles. In order to achieve this, the incidence angle, the inlet Ma number and the water load of the incidence flow was varied. The incidence angle was varied within the limits of stable compressor flow. These limits were given by compressor choke for low incidence angles and flow separations for high incidence angles. Two blade geometries were tested. These geometries were adapted from the middle and outer cross section of an experimental axial compressor rotor blade. Optical, non-intrusive measurement techniques were applied. The key findings are:

- Water injection has multiple effects on the discharge flow properties.
- Discharge flow velocity increases in tendency.
- The deflection angle decreases in tendency.
- The loss coefficient is reduced for a low number of operating points at lowest incidence angles, broadening the range of possible incidence angles.

- The loss coefficient increases for most high blade loading boundary conditions.

There are however implications for the application of water injection to be mentioned for machinery that is in commercial operation. Water injection is widely accepted as a means for power augmentation. In these scenarios a high power output and therefore a high air flow rate is desirable. This leads to low incidence angles for the rotating blades. The experiments however show that in exactly these scenarios the blade aerodynamics are positively, in some cases mildly negatively, affected by the use of water injection in terms of the losses which renders the use of water injection as a means for power augmentation a reasonable action from this point of view. This further emphasises the need for stage matching procedures.

The results show that water injection influences the mean deflection angle. Considering a whole stage (rotor and stator) and a homogeneous incidence flow, this will have multiple effects.

The following guide vane will be confronted with an altered incidence flow. This will have an effect on the stability margin that depends on the design of the following blade row.

Water impinges on the surface of the blade and deposits to a certain fraction on the blade. The surrounding flow drives the water to the trailing edge of the blade where it reenters the flow. This leads to a local concentration of water in the discharge flow resulting in a locally altered discharge flow angle and renders the assumption of a homogeneously distributed dispersed phase not supportable. The extent of this effect is determined by the blade geometry and the droplet properties.

In investigations of two phase compressor flows due to water injection one has to distinguish the thermodynamic and aerodynamic influence. One has to even distinguish between the effects for a single blade row, a whole stage, the entire compressor and the entire gas turbine. The investigations presented in this work show, depending on the geometry, a reduced or a mildly increased value for the aerodynamic losses for low incidence angles. A connection to the consequences for the operation of water injection systems is established. These consequences however do not touch upon the widely accepted negative effects on the surge margin of the whole compressor. Neither do they hold information on the effects on the reported thermodynamic benefit of water injection. The experiments are conducted in a linear cascade. In a rotating machine, a certain fraction of the water will be transported to the blade tip due to centrifugal forces. This might cause additional blockage

and redistribution of the blade loading. This effect has no influence on the results presented in this work.

A meaningful comparison to numerical results cannot be drawn at this point in time as the numerical investigations that are known to the authors are not yet able to account for important influences like the reentering of droplets in the free flow from the suction side (entrainment) in a reliable manner.

In conclusion it can be stated that in order to fully utilize the potential benefit from water injection into the compressor of gas turbines, stage matching procedures have to be conducted that incorporate the influence of water injection.

5.2 Future Prospects

The results of this work give insight into the aerodynamic behavior of axial compressor blade profiles in a two phase flow. The presented data contain information on the loss coefficient, AVDR, deflection angle and the DeHaller number. The experiments conducted delivered answers to a number of open questions and directed the interest to new research opportunities. For this, the presented information can be utilised in multiple ways e.g. for the calculation of compressor maps, stage matching procedures or as a validation case for numerical models. Thermodynamic investigations on the wet compression process can benefit from this data, as well.

Future investigations will focus on isolating the relevant factors of influence like droplet size and blade geometry. The experiments show that droplet coalition due to relative velocities between different droplet classes have an influence on the cascades discharge flow properties. The isolation of the behavior of uninfluenced droplets of a single droplet class will give a better understanding of the influences of each class. This understanding needs to be gained also in dependence of the blade geometry.

Another focus area is the detailed investigation on the behavior of the water on the blade surface to provide further information to researchers that work on numerical methods. To the author's knowledge, no reliable model exists at this point in time to predict the water behavior on the blade surface. The knowledge of this will foster the understanding of water film - boundary layer interactions that influence the blade losses.

Thermodynamic investigations can benefit from this data in the calculation of the efficiency of entire, multistage compressors. These calculations can be extended to gas turbines. The possibility to predict the behavior of the compressor under two phase flow conditions is valuable asset in the design

of water injection systems.

References

- [1] R. V. Kleinschmidt, "Value of wet compression in gas-turbine cycles," *Mech. Eng. (Am. Soc. Mech. Eng.)*, vol. 69(2), pp. 115–116, 1947.
- [2] U. S. ENVIRONMENTAL PROTECTION AGENCY Office of Air and Radiation Office of Air Quality Planning and Standards Research Triangle Park, North Carolina 27711, "Alternative control techniques document—nox emissions from stationary gas turbines: Epa-453/r-93-007."
- [3] D. L. Daggett, "Water misting and injection of commercial aircraft engines to reduce airport nox," *NASA/CR—2004-212957*, 2004.
- [4] I. Day, "Rain ingestion in axial flow compressors at part speed," *ASME Turbo Expo 2000*, GT 2005-68582, 2005.
- [5] AGARD, "Recommended practices for the assessment of the effects of atmospheric water ingestion on the performance and operability of gas turbine engines," *AGARD ADVISORY REPORT NO. 332*, 1995.
- [6] R. O. Dietz and W. A. Flemming, "Altitude-wind-tunnel investigation of thrust augmentation of a turbojet engine," *NACA Report No. RM-E7C12*, 1947.
- [7] R. K. Bhargava, "Gas turbine fogging technology: A state-of-the-art review: Part i: Inlet evaporative fogging- analytical and experimental aspects," *Journal of Engineering for Gas Turbines and Power*, 2007.
- [8] —, "Gas turbine fogging technology: A state-of-the-art review: Part ii: Overspray fogging-analytical and experimental aspects," *Journal of Engineering for Gas Turbines and Power*, 2007.
- [9] —, "Gas turbine fogging technology: A state-of-the-art review: Part iii: Practical considerations and operational experience," *Journal of Engineering for Gas Turbiens and Power*, 2007.
- [10] K. Brun, "Impact of continuous inlet fogging and overspray operation on ge 5002 gas turbine life and performance," *ASME Turbo Expo 2008*, GT2008-50207, 2008.
- [11] R. Bhargava, "Parametric analysis of existing gas turbines with inlet evaporative and overspray fogging," *Journal of Engineering for Gas Turbines and Power*, vol. 127, pp. 145–158, 2005.

-
- [12] M. Bianchi, "Gas turbine power augmentation technologies: A systematic comparative evaluation approach," *ASME Turbo Expo 2010*, GT2010-22948, 2010.
- [13] M. Chaker, "Inlet fogging of gas turbine engines detailed climatic analysis of gas turbine evaporation cooling potential in the usa," *ASME Turbo Expo 2003*, 2003.
- [14] Q. Zheng, "Thermodynamic analyses of wet compression process in the compressor of gas turbine," *Proceedings of ASME Turbo Expo 2002*, GT2002-30590, 2002.
- [15] —, "Thermodynamic performance of wet compression and regenerative (wcr) gas turbine," *Proceedings of ASME Turbo Expo 2003: Power for Land, Sea and Air*, GT2003-38517, 2003.
- [16] I. Roumeliotis and K. Mathioudakis, "Evaluation of water injection effect on compressor and engine performance and operability," *Applied Energy*, 2009.
- [17] J. H. Horlock, "Compressor performance with water injection," *Proceedings of ASME Turbo Expo 2001*, 2001-GT-0343, 2001.
- [18] A. J. White and A. J. Meacock, "An evaluation of the effects of water injection on compressor performance," *Proceedings of ASME Turbo Expo 2003: Power for Land, Sea and Air*, GT2003-38237, 2003.
- [19] J. R. Khan and T. Wang, "Overspray fog cooling in compressor using stage-stacking scheme with non-equilibrium heat transfer model for droplet evaporation," *ASME Turbo Expo 2009*, pp. 609–622, GT2009-59590, 2009.
- [20] C. Matz, W. Kappis, G. Cataldi, G. Mundinger, S. Bischoff, E. Helland, and M. Ripken, "Prediction of evaporative effects within the blading of an industrial axial compressor," *ASME Turbo Expo 2008*, no. GT2008-50166, 2008.
- [21] A. J. White and A. J. Meacock, "Wet compression analysis including velocity slip effects," *ASME Turbo Expo 2010*, GT2010.23793, 2010.
- [22] T. Eisfeld and F. Joos, "On thermodynamic modelling of two-phase flow compression with dispersed water droplets in air," *ISROMAC14, Honolulu US*, 2012.

-
- [23] —, “Experimental investigation of the aerodynamic performance of a linear axial compressor cascade with water droplet loading,” *ASME Turbo Expo 2010*, GT2010-22831, 2010.
- [24] K. Brun, R. Kurz, and H. Simmons, “Aerodynamic instability and life-limiting effects of inlet and interstage water injection into gas turbines,” *Journal of Engineering for Gas Turbines and Power*, vol. 128, pp. 617–625, 2006.
- [25] L. Sun, Y. Li, Q. Zheng, and R. Bhargava, “The effects of wet compression on the separated flow in a compressor stage,” *ASME Turbo Expo 2008*, GT2008-50920.
- [26] M. Luo, Q. Zheng, L. Sun, Q. Deng, S. Li, C. Liu, and R. Bhargava, “The numerical simulation of inlet fogging effects on the stable range of a transonic compressor stage,” *Proceedings of ASME Turbo Expo 2011*, GT2011-46124, 2011.
- [27] L. Sun, Q. Zheng, M. Luo, Y. Li, J. Wang, and R. Bhargava, “Numerical through flow simulation of a gas turbine engine with wet compression,” *Proceedings of ASME Turbo Expo 2012*, GT2012-68846, 2012.
- [28] T. Eisfeld and F. Joos, “Experimental investigation of two-phase flow phenomena in transonic compressor cascades,” *ASME Turbo Expo 2009*, GT2009-59365, 2009.
- [29] J. C. Emery, L. J. Herrig, J. R. Erwin, and A. R. Felix, “Systematic two-dimensional cascade tests of naca 65-series compressor blades at low speeds,” *NACA report: NACA-TR-1368*, 1958.
- [30] E. S. Ulrichs, “Experimental investigations into the behavior and influence of water droplets in a compressor cascade flow,” Ph.D. dissertation, Helmut-Schmidt-Universität / Universität der Bundeswehr Hamburg, Hamburg, 2007.
- [31] T. Eisfeld, “Experimentelle Untersuchung der Aerodynamik einer mit Wassertropfen beladenen Luftströmung in einem ebenen Verdichtergitter,” Ph.D. dissertation, Helmut-Schmidt-Universität / University of the Federal Armed Forces Hamburg, Hamburg, 2011.
- [32] C. Hirsch, *Advanced methods for cascade testing: Méthodes avancées pour les essais des grilles d’aubes*. Neuilly sur Seine: North Atlantic

- Treaty Organization, Advisory Group for Aerospace Research & Development, 1993.
- [33] J. Lepicovsky, E. McFarland, R. Chima, and J. Wood, "On flowfield periodicity in the nasa transonic flutter cascade, part i-experimental study," *ASME Turbo Expo 2000*, 200-GT-0572, 2000.
- [34] W. Traupel, *Thermische Turbomaschinen Erster Band. Thermodynamisch-strömungstechnische Berechnung*, 4th ed. Berlin and Heidelberg and New York: Springer, 2001.
- [35] —, *Thermische Turbomaschinen Zweiter Band. Geänderte Betriebsbedingungen, Regelung, Mechanische Probleme, Temperaturprobleme*, 4th ed. Berlin and Heidelberg and New York: Springer, 2001.
- [36] H. Oertel, *Prandtl - Führer durch die Strömungslehre: Grundlagen und Phänomene*, 12th ed. Wiesbaden: Vieweg + Teubner, 2008.
- [37] R. H. Aungier, *Axial-flow compressors: A strategy for aerodynamic design and analysis*. New York: ASME Press, 2003.
- [38] H. Grein, R. Röper, and E. Schmidt, "Auslegung und Untersuchung einer invers ausgelegten Beschaufelung eines einstufigen Axialverdichters mit Vorleitrad," *Forschungsberichte Verbrennungskraftmaschinen, FVV; 489*, vol. 489, 1991.
- [39] N. Scholz, "Über die Durchführung systematischer Messungen an ebenen Schaufelgittern," *Zeitschrift für Flugwissenschaften*, no. 10, 1956.
- [40] S. Lieblein, "Experimental flow in 2d-cascades," *The Aerodynamic Design of the Axial Flow Compressor*, vol. NACA RME 56B03 reprinted NASA SP 36 in 1965, 1965.
- [41] W. J. G. Bräunling, *Flugzeugtriebwerke*, 3rd ed. Heidelberg and London and New York: Springer, 2009.
- [42] H. A. Schreiber, "Axial velocity density ratio influence on exit flow angle in transonic/supersonic cascades," *Karman Institute for Fluid Dynamics*, vol. Lecture Series 1988-03, 1988.
- [43] U. Köller, "Entwicklung einer fortschrittlichen Profilsystematik für stationäre Gasturbinenverdichter," *Forschungsbericht DLR e.V.*, no. 20, 1999.

-
- [44] U. Stark, *Ebene Verdichtergitter in quasizweidimensionaler Unterschallströmung*. Düsseldorf: VDI-Verl., 1987.
- [45] C. Crowe, M. Sommerfeld, and Y. Tsuji, *Multiphase Flows with Droplets and Particles*. Boca Raton: CRC Press, 1997.
- [46] H. Herwig, *Strömungsmechanik: Eine Einführung in die Physik und die mathematische Modellierung von Strömungen*. Berlin and Heidelberg and New York: Springer, 2006.
- [47] H. Schlichting and K. Gersten, *Grenzschicht - Theorie*. Berlin and Heidelberg and New York: Springer, 1996.
- [48] U. Ganzer, S. Rill, P. Thiede, and J. Ziemann, *Gasdynamik*. Berlin and New York: Springer-Verlag, 1988.
- [49] L. Hilgenfeld, “Turbulenzstrukturen in hochbelasteten Transsonik-Verdichtergittern unter besonderer Berücksichtigung der Verdichtungsstoß-Grenzschicht-Interferenz,” Ph.D. dissertation, Universität der Bundeswehr München, Munich, 17.11.2006.
- [50] C. E. Brennen, *Fundamentals of multiphase flow*. Cambridge [England] and New York: Cambridge University Press, 2005.
- [51] G. Wozniak, *Zerstäubungstechnik: Prinzipien, Verfahren, Geräte*, 1st ed., ser. VDI. Berlin: Springer, 2001.
- [52] F. Schmelz, “Tropfenzerfall in beschleunigten Gasströmungen,” Ph.D. dissertation, Universität Dortmund, Aachen, 2002.
- [53] A. M. Worthington, *A Study of Splashes*. London and New York and Bombay and Calcutta: Longmans, Green and Co., 1908.
- [54] A. L. Yarin, “Drop impact dynamics: Splashing, spreading, receding, bouncing,” *Annual Review of Fluid Mechanics*, no. 38, pp. 159–192, 2006.
- [55] R. Rioboo, M. Marengo, and C. Tropea, “Time evolution of liquid drop impact onto solid, dry surfaces,” *Experiments in Fluids*, no. 33, pp. 112–124, 2002.
- [56] C. Mundo, “Zur Sekundärzerstäubung newtonischer Fluide an Oberflächen,” Ph.D. dissertation, Universität Erlangen-Nürnberg, Erlangen-Nürnberg, 19.07.2012.

- [57] L. Xu, Z. W. W., and S. R. Nagel, "Drop splashing on a dry smooth surface," *Physical Review Letters*, vol. 94, no. 18, 2005.
- [58] M. Rein, "Phenomena of liquid drop impact on solid and liquid surfaces," *Fluid Dynamics Research*, vol. 12, no. 2, pp. 61–93, 1993.
- [59] M. B. Lesser and J. E. Field, "The impact of compressible liquids," *Annual Review of Fluid Mechanics*, no. 15, pp. 97–122, 1983.
- [60] F. J. Heymann, "High-speed impact between a liquid drop and a solid surface," *Journal of Applied Physics*, vol. 40, no. 13, pp. 5113–5122, 1969.
- [61] V. Surov, "Initial stage in the impingement of a water drop onto a compressible baffle," *Fluid Mechanics, Soviet Research*, pp. 1–7, 1989.
- [62] C. D. Stow and M. G. Hadfield, "An experimental investigation of fluid flow resulting from the impact of a water drop with an unyielding dry surface," *Proceedings of the Royal Society A: Mathematical, Physical and Engineering Sciences*, vol. 373, pp. 419–441, 1981.
- [63] G.E. Cossali, "Multiple drop impact on heated surface," *9th International Conference on Liquid Atomization and Spray Systems ICLASS*, 2003.
- [64] B. Richter, K. Dullenkopf, and H. J. Bauer, "Investigation of secondary droplet characteristics produced during wall impact," *Lehrstuhl und Institut für Thermische Strömungsmaschinen (ITS) Universität Karlsruhe*, 2004.
- [65] C. Stow and R. Stainer, "The physical products of a splashing water drop," *Meteorological Society of Japan*, vol. 55, pp. 518–532, 1977.
- [66] P. Walzel, "Zerteilgrenze beim Tropfenaufprall," *Chemie Ingenieur Technik*, vol. 52, no. 4, pp. 338–339, 1980.
- [67] W. Samenfink, "Grundlegende Untersuchung zur Tropfeninteraktion mit schubspannungsgetriebenen Wandfilmen," Ph.D. dissertation, Universität Karlsruhe, Karlsruhe, 09.07.2012.
- [68] A. L. Yarin and D. A. Weiss, "Impact of drops on solid surfaces: self-similar capillary waves, and splashing as a new type of kinematic discontinuity," *Journal of Fluid Mechanics*, vol. 283, p. 141, 1995.

- [69] G. E. Cossali, “The impact of a single drop on a wetted solid surface,” *Experiments in Fluids*, vol. 22, pp. 463–472, 1997.
- [70] R. Rioboo, C. Bauthier, J. Conti, M. Voue, and J. d. Coninck, “Experimental investigation of splash and crown formation during single drop impact on wetted surfaces,” *Experiments in Fluids*, vol. 35, no. 6, pp. 648–652, 2003.
- [71] J. Urban, “Numerische Untersuchung und Modellierung von Tropfen-Wand-Interaktionen,” Ph.D. dissertation, Universität Stuttgart, Stuttgart, 2009.
- [72] H. Gomma and B. Weigand, “Modelling and investigation of the interaction between drops and blades in compressor cascades with a droplet laden inflow,” *ISROMAC-14*, vol. 2012, 2012.
- [73] B.I. Nihmatulia, V.V.Guguchkin, N.I.Yasil’ev, and Yu.P.Arestenko, “The knockout of secondary droplets from the surface of a film (droplet carryover) in dispersed-film flows,” *Heat and Mass Transfer and Physical Gasdynamics*, vol. 31, no. 4, pp. 600–603, 1993.
- [74] S.M. Frolov, B.E. Gelfand, and E.I. Timofeev, “Interaction of a liquid film with a high-velocity gas flow behind a shock wave,” *Translated from Fizika Goreniya i Vzryva*, vol. 20, no. 5, pp. 107–114, 1984.
- [75] R.D. Archer, B.E Milton, M. Behnia, and R.T. Casey, “Entrainment of liquid droplets into shock-induced airstreams,” *20th International Symposium on Shock Waves*, pp. 1267–1272, 1995.
- [76] B.E. Milton, M. Behnia, and K. Takayama, “Interaction of liquid films with shock induced airflows,” *Proc. 6th Symposium on Shock Waves*, pp. 1265–1270, 1995.
- [77] H. Saber and M. El-Genk, “On the breakup of a thin liquid film subject to interfacial shear,” *Journal of Fluid Mechanics*, vol. 500, pp. 113–133, 2004.
- [78] D. E. Hartley and W. Murgatroyd, “Criteria for the break-up of thin liquid layers flowing isothermally over solid surfaces,” *International Journal of Heat and Mass Transfer*, vol. 7, no. 9, pp. 1003–1015, 1964.
- [79] G. Mie, “Beiträge zur Optik trüber Medien, speziell kolloidaler Metal-lösungen,” *Annalen der Physik*, vol. 330, no. 3, pp. 377–445, 1908.

-
- [80] H.-E. Albrecht, *Laser doppler and phase doppler measurement techniques*. Berlin and New York: Springer, 2003.
- [81] B. Ruck, *Lasermethoden in der Strömungsmesstechnik*. Stuttgart: AT-Fachverlag, 1990.
- [82] R. P. Dring, “Sizing criteria for laser anemometry particles,” *Journal of Fluids Engineering*, vol. 104, no. 1, p. 15, 1982.
- [83] M. Schatz and M. Casey, “Design and testing of a new miniature combined optical/pneumatic wedge probe for the measurement of steam wetness,” *AIP Conference Proceedings*, pp. 464–479, 2007.
- [84] M. Renner, “Entwicklung eines optisch-pneumatischen Meßsystems für Zweiphasen-Wasserdampfströmungen,” Ph.D. dissertation, University of Stuttgart, Stuttgart and Germany, 2001.
- [85] V. M. Boiko, “Dynamics of droplet breakup in shock waves,” *Translated from Zhurnal Prikladnoi Mekhaniki i Tekhnicheskoi Fiziki*, no. No. 2, pp. 108–115, 1986.
- [86] K.D. Khan and N. Chigier, “Effect of shock waves on liquid atomiation of a a two-dimensional airblast atomizer,” *Atomization and Sprays*, vol. 1, pp. 113–136, 1991.
- [87] E. Chang and K. Kailasanath, “Shock wave interactions with particles and liquid fuel droplets,” *Shock Waves*, vol. 12, no. 4, pp. 333–341, 2003.
- [88] D.L. Tweedt, “Experimental investigation of the performance of a supersonic compressor cascade,” *NASA Technical Memorandum 100879*, 1988.

List of Figures

2.1	Test rig overview	10
2.2	Measurements taken in vicinity of test section	11
2.3	Incidence angle variation mechanism in neutral position (a) and neutral position plus 5° (b)	12
2.4	Boundary layer injection system: nozzle configuration	13
2.5	Measured inlet velocity profile without (a) and with (b) injection as reported in [28]	14
2.6	View into the settling chamber (a). Schematic of test rig configuration (b).	15
2.7	Pin jet nozzle bete PJ10	16
2.8	Measured droplet size distribution at cascade inlet; total number of droplets per node: 10000	16
2.9	Axial compressor velocity plan	17
2.10	Traverse nomenclature	20
3.1	Transonic flow conditions: interblade shock configuration	27
3.2	Droplet deformation process	34
3.3	Breakup mechanisms as determined by We number	35
3.4	Water film on suction side with rivulets	43
3.5	Lighth scatter of polarized light on a single droplet	44
3.6	Intensity of scattered light as a function of scatter angle for $d_d = 1\lambda$ (a), $d_d = 10\lambda$ (b).(Dantec Dynamics)	46
3.7	Principle of Laser Doppler Anemometry	46
3.8	Principle of Phase Doppler Anemometry (Dantec Dynamics, 2006)	48
3.9	Principle setup of LDA/PDA (Dantec Dynamics, 2006)	49
3.10	Measurement positions	50
3.11	Measurement positions in the investigation of the interblade flow	51
3.12	Measurement setup water load	52
3.13	Shadowgraphy setup	54
4.1	Water film formation on suction side of outer cross section. $Ma=0.8$, $X = 1.3\%$, $\beta_1 = 147^\circ \dots 154^\circ$	57
4.2	Water film formation on suction side of middle cross section $Ma=0.78$, $X = 1.3\%$, $\beta_1 = 137^\circ \dots 145^\circ$	58
4.3	Simulated dry air flow: velocity contour plot $Ma=0.8$, $\beta_1 = 147^\circ$ vs $\beta_1 = 151^\circ$	60
4.4	Shadowgraphy image of inter blade flow	61

4.5	Secondary droplet disintegration in cascade flow	62
4.6	Streak formation in cascade discharge flow	62
4.7	Case no. m078.0: measured normalized discharge velocity for low (a) and high (b) incidence angles	65
4.8	Case no. m078.13: measured normalized discharge velocity for low (a) and high (b) incidence angles	66
4.9	Case no. m078.21: measured normalized discharge velocity for low (a) and high (b) incidence angles	67
4.10	Case no. m071.0: measured normalized discharge velocity for low (a) and high (b) incidence angles	68
4.11	Case no. m071.13: measured normalized discharge velocity for low (a) and high (b) incidence angles	69
4.12	Case no. m071.21: measured normalized discharge velocity for low (a) and high (b) incidence angles	70
4.13	Case no. o089.0: measured normalized discharge velocity for low (a) and high (b) incidence angles	73
4.14	Case no. o089.13: measured normalized discharge velocity for low (a) and high (b) incidence angles	74
4.15	Case no. o089.21: measured normalized discharge velocity for low (a) and high (b) incidence angles	75
4.16	Case no. o080.0: measured normalized discharge velocity for low (a) and high (b) incidence angles	76
4.17	Case no. o080.13: measured normalized discharge velocity for low (a) and high (b) incidence angles	77
4.18	Case no. o080.21: measured normalized discharge velocity for low (a) and high (b) incidence angles	78
4.19	Case no. m078.0: measured deflection angle for low (a) and high (b) incidence angles	79
4.20	Case no. m078.13: measured deflection angle for low (a) and high (b) incidence angles	80
4.21	Case no. m078.21: measured deflection angle for low (a) and high (b) incidence angles	81
4.22	Case no. m071.0: measured deflection angle for low (a) and high (b) incidence angles	82
4.23	Case no. m071.13: measured deflection angle for low (a) and high (b) incidence angles	83
4.24	Case no. m071.21: measured deflection angle for low (a) and high (b) incidence angles	84

4.25	Case no. o089.0: measured deflection angle for low (a) and high (b) incidence angles	86
4.26	Case no. o089.13: measured deflection angle for low (a) and high (b) incidence angles	87
4.27	Case no. o089.21: measured deflection angle for low (a) and high (b) incidence angles	88
4.28	Case no. o080.0: measured deflection angle for low (a) and high (b) incidence angles	89
4.29	Case no. o080.13: measured deflection angle for low (a) and high (b) incidence angles	90
4.30	Case no. o080.21: measured deflection angle for low (a) and high (b) incidence angles	91
4.31	Influence of water injection on AVDR and loss coefficient. Middle cross section at inlet Ma=0.78	93
4.32	Influence of water injection on discharge flow angle and DeHaller number. Middle cross section at inlet Ma=0.78	94
4.33	Influence of water injection on AVDR, loss coefficient. Middle cross section at inlet Ma=0.7	95
4.34	Influence of water injection on discharge flow angle and DeHaller number. Middle cross section at inlet Ma=0.71	96
4.35	Influence of water injection on AVDR, loss coefficient. Outer cross section at inlet Ma=0.89	98
4.36	Influence of water injection on discharge flow angle and DeHaller number. Outer cross section at inlet Ma=0.89	99
4.37	Influence of water injection on AVDR, Loss coefficient. Outer cross section at inlet Ma=0.8	100
4.38	Influence of water injection on discharge flow angle and DeHaller number. Outer cross section at inlet MA=0.8	101
4.39	Measured blade passage Ma number for middle cross section ($\beta_1 = 140^\circ, X = 1.3$)	106
4.40	Measured blade passage Ma number for outer cross section ($\beta_1 = 154^\circ, X = 1.3$)	107

List of Tables

2.1	Spray properties produced by PJ10 nozzle at 200bar	16
2.2	Compressor design parameters	19
2.3	Geometrical data of the tested blade profiles	19
3.1	Shadowgraphy setup properties	53
4.1	Phenomenological experiments conducted	56
4.2	Experiments conducted	64
4.3	Outer cross section: experiments conducted	72